

Mgr inż. Marta Pawlak

Gas Conditioning for Fuel Cells in Microreactors

DISSERTATION

First supervisor: Univ.-Doz.-Ing. Dr.Techn. Viktor Hacker

Institute for Chemical Engineering and Environmental Technology
Christian Doppler Laboratory for Fuel Cell Systems
Graz University of Technology

2010

ACKNOWLEDGEMENT/DANKSAGUNG

This thesis was conducted at the Christian Doppler Laboratory for Fuel Cell Systems, a research facility implemented at the Institute of Chemical Engineering and Environmental Technology, Graz University of Technology.

I was supported by many people in writing this thesis.

First of all, I would like to thank my supervisor Univ.-Doz. Dr. techn. Viktor Hacker, head of the Doppler Laboratory for Fuel Cell Systems, for his initiating, guidance, and supporting while writing my thesis.

I am very grateful to Dipl.-Ing. Dr.techn., Ao.Univ.-Prof. Klaus Reichmann, who kindly took the role of the co-supervisor and for his advices and interest in my work.

Special thanks go to my colleagues Adina, Munazza, Markus, Gerd, Thomas, Wolfgang, Manfred for their help, friendship and good cooperation.

Finally, I want to thank my family especially my parents and my sister, and also my friends for their continuous support and encouragement during this task.

Last, but not least I would like to thank Lukas for his help and patience.

ABSTRACT

High- and low-temperature water gas shift reactions were examined for the ability to decrease the CO fraction of the synthesis gas down to a level tolerable for proton exchange membrane fuel cells. These gas purification methods had the advantage of a higher hydrogen yield being achievable by “converting” CO into H₂, thus leading to a higher overall efficiency of the fuel cell system. The performance of microstructured reactors fitted with different commercial catalysts, which was discussed within the first part of this paper as a function of the temperature, gas flow rate, and gas composition, was evaluated.

The preparation, optimization of catalysts for the water-gas shift reaction in a micro-channel reactor were investigated in the second part of this experimental work with the aim of generating hydrogen for mobile fuel cell systems. The catalysts had to exhibit high catalytic activity and strong adhesion to support foils and prove long-term stability, especially during start-up/shut-down procedures. The coating of micro-channel metallic plates was performed first with nanopowders/support materials by spin-coating methods. The dispersion stability and the detailed interaction between particles were determined by zeta-potential analysis. The catalytic active materials were deposited during the impregnation method and accomplished the forming of the two catalyst systems. Well-adhering wash coats were obtained on micro-structured foils. A detailed investigation into the influence of different variables on the coating uniformity has led to a coating of catalysts inside stainless steel micro-channels with good adhesion. The adhesion was highly dependant on the nature of binder, initial particle sizes, pH and also surfactant addition. The catalysts were tested at the reaction temperature range between 200 °C and 450 °C in one-stage water-gas shift reactors. The catalyst loading, the surface area and platinum amount had a significant effect on the activity of both Pt/CeO₂/Al₂O₃ and Pt/CeO₂ catalysts.

KURZFASSUNG

Wassergas-Shift Reaktionen wurden bei unterschiedlichen Temperaturen auf die Möglichkeit zur Reduktion des CO Gehalts im Synthesegas bis auf einen maximal für PEM Brennstoffzellen zulässigen Wert untersucht. Vorteil dieser Gasreinigungsmethode ist die hohe Ausbeute, die durch die direkte Umwandlung von CO in H₂ erreicht wird. Dieser Umstand führt in weiterer Folge zu einer Effizienzerhöhung des gesamten Brennstoffzellensystems. Die Leistung von mikrostrukturierten Reaktoren, die mit unterschiedlichen kommerziell erhältlichen Katalysatoren beschichtet wurden, wurde evaluiert. Diese Leistung hängt, wie im ersten Teil dieser Arbeit diskutiert wird, von der Temperatur, dem Gasfluss und der Gaszusammensetzung ab.

Die Herstellung und Optimierung von Katalysatoren für die Wassergas-Shift Reaktion in einem Mikrokanal-Reaktor wurde im zweiten Teil der experimentellen Arbeit untersucht. Ziel dieser Untersuchungen ist die Bereitstellung von Wasserstoff für mobile Brennstoffzellensysteme. Hauptaugenmerk wurde dabei auf hohe katalytische Aktivität, eine starke Adhäsion auf der Mikrokanalplatte und auf Langzeitstabilität, vor allem unter Start/Stopp Bedingungen gelegt. Die Mikrokanalplatten wurden mit dem Katalysatorträger durch einen Spin-Coating Prozess beschichtet. Die Stabilität und die Interaktion der Partikel im dispergierten Zustand wurden durch die Analyse des Zeta-Potentials bestimmt. Die katalytisch aktiven Materialien wurden mittels einer Imprägniermethode abgeschieden und durch die Bildung eines Katalysatorsystems abgeschlossen. Gut haftende „wash-coat“ Katalysatoren wurden auf Mikrokanalplatten erhalten. Die Aufklärung des Einflusses von unterschiedlichen Faktoren auf die Gleichmäßigkeit der Beschichtung führte zu verbesserter Adhäsion des Katalysators in den Kanälen der Mikrokanalplatten. Die Stärke der Adhäsion war abhängig vom Bindermaterial, der ursprünglichen Partikelgröße, dem pH Wert und der Tensid Zugabe.

Die so erhaltenen Katalysatoren wurden bei Reaktionstemperaturen zwischen 200 °C und 450 °C in einem einstufigen Wassergas-Shift Reaktor charakterisiert. Die Katalysatorbeladung, die Oberfläche und die Platinmenge hatten einen entscheidenden Einfluss auf die Aktivität von Pt/CeO₂/Al₂O₃ und Pt/CeO₂ Katalysatoren.

TABLE OF CONTENTS

1	INTRODUCTION	7
2	FUNDAMENTALS.....	12
2.1	WATER GAS SHIFT IN MICROSTRUCTURED REACTORS.....	12
2.2	WATER GAS SHIFT REACTION	13
2.3	WATER GAS SHIFT REACTORS.....	14
2.3.1	MONOLITHIC REACTORS	14
2.3.2	PLATE HEAT-EXCHANGER REACTORS	14
2.3.3	WATER GAS SHIFT REACTION IN MICROSTRUCTURES.....	14
2.3.4	STACK-LIKE REAKTOR APPLIED TO WATER GAS SHIFT.....	15
2.3.5	SANDWICH-TYPE REACTOR (HCR)	15
2.4	WATER GAS SHIFT CATALYSTS.....	15
2.4.1	NON-PRECIOUS-METAL-CATALYSTS.....	15
2.4.2	PRECIOUS-METAL CATALYSTS.....	16
2.4.2.1	Pt/ CeO ₂ CATALYST FOR WGS REACTION	16
2.4.2.2	Pt/CeO ₂ /Al ₂ O ₃ CATALYST FOR WGS REACTION IN MICROREACTORS	17
2.5	WGS CATALYST APPLICATIONS	19
2.6	THE ADVANTAGES AND DRAWBACKS OF MICROSTRUCTURED DEVICES	19
2.7	CATALYST COATING TECHNIQUES	20
2.7.1	METALLIC SUBSTRATE PREPARATION	20
2.7.2	CATALYST COATING AS SUSPENSION.....	21
2.7.3	SOL-GEL COATING.....	24
2.7.4	ANODIC OXIDATION.....	27
2.7.5	ELECTROPHORETIC DEPOSITION (EPD)	27
2.7.6	FLAME SPRAY DEPOSITION.....	27
2.7.7	ELECTROLESS PLATING	27
2.7.8	CHEMICAL VAPOR DEPOSITION (CVD).....	28
2.7.9	SPUTTERING VS: UV-DECOMPOSITION	28
2.7.10	MOLTEN SALT SYNTHESIS.....	28
2.7.11	ZEOLITE CATALYSIS	28
2.7.12	IMPREGNATION METHOD.....	30
2.8	CATALYST DEPOSITION METHODS	31
2.8.1	DIP-COATING (SPRAY COATING)	31
2.8.2	DROP-COATING.....	31
2.8.3	SPIN-COATING.....	31
2.8.4	BRUSH; SYRINGE.....	31
2.8.5	INFILTRATION; GAS FLUID	31
2.8.6	ELECTROSTATIC SOL-SPRAY DEPOSITION.....	32
3	EXPERIMENTAL DETAILS	33
3.1	CATALYST CHARACTERIZATION METHODS.....	33

3.1.1	BET SURFACE AREA MEASUREMENT (S_{BET}).....	33
3.1.2	MERCURY POROSIMETRY	36
3.1.3	SCANNING ELECTRON MICROSCOPY WITH ENERGY-DISPERSIVE SPECTROMETRY (SEM; EDXS) 39	
3.1.4	X-RAY DIFFRACTION (XRD).....	39
3.1.5	THERMO GRAVIMETRIC ANALYSIS (TGA)	41
3.1.6	PARTICLE SIZE ANALYSIS BY LASER DIFFRACTION	43
3.1.7	PARTICLE SIZE ANALYSIS AND ZETA POTENTIAL MEASUREMENTS	45
3.2	EXPERIMENTAL SET UP	47
3.2.1	TEST STAND	47
3.2.2	REACTOR	47
3.2.3	ONLINE GAS ANALYSIS	47
3.2.3.1	INFRARED ANALYSER MODULE: URAS 14.....	47
3.2.3.2	THERMAL CONDUCTIVITY ANALYSER MODULE: CALDOS 17	50
4	CHARACTERIZATION OF HTS AND LTS REACTIONS IN MICRO-STRUCTURED REACTORS	52
4.1	EXPERIMENTAL.....	52
4.1.1	CATALYST PREPARATION.....	52
4.1.2	COATING OF THE PLATES (WASH COATING)	52
4.1.3	CHARACTERIZATION OF THE CATALYST.....	52
4.1.4	EXPERIMENTAL CONDITIONS.....	53
4.1.5	GEOMETRIC STRUCTURE OF THE CATALYST LAYERS	54
4.1.6	DETERMINING CATALYTIC PROPERTIES.....	58
5	HYDROGEN PURIFICATION USING MICROSTRUCTURES PART I: PREPARATION OF Al_2O_3 AND CeO_2 WASHCOATS IN MICROCHANNELS	63
5.1	EXPERIMENTAL.....	63
5.1.1	EXPERIMENTAL SET-UP.....	63
5.1.2	CATALYST PREPARATION (SUSPENSION).....	63
5.1.3	COATING OF THE PLATES (SPIN COATING).....	64
5.1.4	CHARACTERIZATION OF COATED LAYERS	64
5.1.4.1	SCANNING ELECTRON MICROSCOPY (SEM; EDX).....	64
5.1.4.2	PARTICLE ANALYSIS	64
5.1.4.3	THERMO-GRAVIMETRIC ANALYSIS (TGA)	64
5.1.4.4	MERCURY POROSIMETRY.....	65
5.1.4.5	ZETA POTENTIAL	65
5.2	RESULTS AND DISCUSSION	65
5.2.1	PARTICLE SIZE AND MORFOLOGY	65
5.2.2	CHARACTERIZATION OF SUSPENSIONS	67
5.2.2.1	ZETA POTENTIAL	67
5.2.2.2	EFFECT OF SURFACTANT AND PVA ADDITION	67
5.2.2.3	THERMO-GRAVIMETRIC ANALYSIS (TGA)	68
5.2.3	CHARACTERIZATION OF LAYERS	69
5.2.3.1	EFFECT OF DRYING ON Al_2O_3 LAYER.....	69
5.2.3.2	EFFECT OF SOLID CONTENT VARIATIONS ON LAYER FORMATION	70

5.2.3.3	EFFECT OF CALCINATION TEMPERATURE FOR THE Al ₂ O ₃ LAYER	71
5.2.3.4	POROSIMETRY (PORE DIAMETER).....	72
5.2.3.5	EFFECT OF FREQUENCIES OF COATING ON METAL LOADING.....	72
5.2.3.6	EFFECT OF LAYER NUMBER AND BINDER MOLECULAR WEIGHT ON STRUCTURE MORPHOLOGY	75
5.2.3.7	ADHESION	75
6	<i>HYDROGEN PURIFICATION USING MICROSTRUCTURES PART II: CATALYTIC PERFORMANCE OF NM-Pt- CATALYST FOR WATER GAS SHIFT ON MICROSTRUCTURED PLATES</i>	78
6.1	EXPERIMENTAL SECTION.....	78
6.1.1	<i>EXPERIMENTAL SET-UP (MICROCHANNEL PLATES)</i>	78
6.1.2	<i>CATALYST PREPARATION (SUSPENSION)</i>	78
6.1.3	<i>COATING OF THE PLATES (SPIN COATING AND IMPREGNATION)</i>	80
6.2	RESULTS AND DISCUSSION	80
6.2.1	<i>EFFECT OF IMPREGNATION NUMBER ON CATALYST LOADING</i>	80
6.2.2	<i>MORFOLOGY OF THE COATED CATALYSTS</i>	81
6.2.3	<i>EFFECT OF H₂O</i>	86
6.2.4	<i>EFFECT OF CATALYST WEIGHT (WHSV)</i>	89
6.2.5	<i>COMPARISONS BETWEEN Pt/CeO₂/Al₂O₃ AND Pt/CeO₂ CATALYST</i>	92
6.2.6	<i>COMMERCIAL CATALYST</i>	93
7	<i>SUMMARY</i>	95

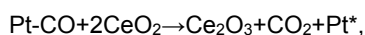
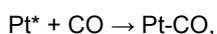
1 INTRODUCTION

Fuel cell technology has reached a stage of development where it has become increasingly interesting for commercial applications. Currently, most of the hydrogen is produced from hydrocarbons by steam reforming or autothermal reforming combined with complex gas-cleaning procedures.

A typical gas-cleaning procedure includes the following two steps: The reformed fuels are first passed through the high temperature water gas shift (WGS) stage (HTS) and are then fed into the low-temperature water gas shift stage (LTS) to reduce the CO concentration. The outlet gas still contains small amounts of carbon monoxide, which can poison the platinum catalyst used in proton exchange membrane fuel cells. Therefore, preferential oxidation can be utilized as an additional fine purification step.

The HTS and LTS reactions can be carried out in a micro fuel processor. The advantages of these systems include high conversion efficiencies, fast dynamic responses, low heat losses, and efficient usage of the anode off-gases by catalytic combustors [44]. Catalyzed microstructured plates create a compact system [91, 92]. The stainless steel foils show strong adhesive properties for catalyst layers. The catalysts are deposited using the wash coating method [44].

Precious metal catalysts such as Pt/CeO₂, Au/CeO₂, Au/Fe₂O₃ [93], Ru/CeO₂, Ni/CeO₂, Pd/CeO₂ [94], Ru/ZrO₂, Ru/SiO₂, and Ru/Al₂O₃ [6] as well as catalysts with several layers such as Pt/Rh, Pt, and Pt/Pd on CeO₂/Al₂O₃ and Pt/Rh/Al₂O₃ [24] are described in the literature for CO removal. Pt/CeO₂ catalysts are selected for the experimental examinations of the WGS reaction because of their bifunctional mechanism [95] and their high CO-conversion rates under high-temperature WGS reaction conditions [48].



Ceria is reduced from Ce⁴⁺ to Ce³⁺ and donates oxygen ions for the oxidation of carbon monoxide to carbon dioxide. Platinum, on the other hand, catalyzes the reduction of water into hydrogen, thus liberating an oxygen ion that reoxidizes the ceria Ce³⁺ to Ce⁴⁺ [20].

Inexpensive fabrication techniques and lower catalyst cost may play a significant role in the overall fuel processor cost. Here the micro-structured devices offer many possibilities for cost reduction owing to the improved mass transfer in small channel systems, which allow a highly-efficient usage of the catalyst. Micro-structure devices allow for rapid system stabilization due to the fast dynamic response because of the low residence times applied. Micro-structured reactors not only enable improved catalyst effectiveness but also working at a high efficiency/volume ratio, thus leading to a material and size reduction potential. For these reasons, the novel reactor concept of fuel processing has various existing opportunities to achieve the maximum performances. If the exothermic heat of reaction can be removed from the reactor, the thermodynamics can be exploited by driving down the exit temperatures. Micro-channel reactors appear to be able to accomplish the formidable heat transfer task while achieving small reactor volumes. However, it will require high performance catalysts to take advantage of the favourable low temperature equilibria [5].

In order to functionalize micro-structured components for heterogeneously catalysed reactions, the catalytically active layer has to be fixed within the micro-structure. Often it was difficult to achieve strong adhesion of the catalyst coating on the micro-structured material, which was made of metal. But for some catalysed reactions, the inner surface area of the micro-channels was not large enough to attach a sufficient number of active centres. It was therefore necessary to develop active coatings with a large surface area on micro-structured metal foils for coating with catalytically-active solutions such as noble metals. The coating of

the catalyst support materials onto micro-channel plates was widely achieved by wash coating of the suspensions. Gamma alumina was the most popular catalyst support material, which was achieved as a result of the suspension deposition. In many publications in the last four years, it has been reported that the suspension usually consisted of alumina or commercial catalyst powder, water, binder and acids for pH adjustment [26, 35, 49, 118].

The alumina powder with the main particle size of 3 μm was mixed with a commercial methylhydroxyethyl-cellulose binder, and only minor cracks appeared on the layer after the coating of aqueous suspension on the micro-structured platelet [25]. The effect of a nature and the concentration of the three high molecular weight binders such as PVA (Mw = 95000), Tylose (Mw = 95000) and PEG (Mw = 20000) in the suspension on the quality of alumina and low temperature shift (LTS) commercial catalyst coating were investigated for the water-gas shift reaction obtained in micro-channels [29]. Pfeifer et al. [47] used nanoparticles such as CuO, ZnO, TiO₂ and Al₂O₃ dispersed in an aqueous solution of 1 wt.% hydroxy ethyl cellulose (HEC) [47, 119] and with hydroxy propyl cellulose (HPC, Mw=370000g/mol) dissolved in isopropyl alcohol [30]. The catalysts were only active for several hours. The influence of layer thickness on its uniformity was analysed for Al₂O₃ (185 m²/g) coatings. Cracks and catalyst layer deteriorations were only found with thicknesses of more than 40 μm [34]. Due to the variation of H₂O/solid ratio in the slurry, the highly-active and stable Rh/MgO-Al₂O₃ catalyst has been discovered [36]. The easy way to prepare the suspension based on nm-particles was presented by Goerke et al. [6]. The CeO₂ and ZrO₂ powders were suspended in ethyl alcohol or water and then applied onto stainless steel and FeCrAlloy foils.

Some other interesting articles were described the Al₂O₃-coating optimization on the monolith structures. The concentration of solid material in a suspension varied largely and influenced the desired layer thickness, which depends also on the nature of the particle surfaces. Agrafiotis et al. [49] showed that the size of the suspended particles has a great influence on the adhesion on the substrate in the case of monolith coating by different oxides. It was also proved several

times that the amount of alumina increased on the monolith walls with increasing pH-value and increasing alumina concentration in the suspension [51].

To be accepted for the mass production of fuel processors, it is necessary to reduce the cost of fabrication techniques. Catalyst cost is an important part of the total fuel processor cost, especially when precious metals are used as a catalyst. Promising possibilities for cost reduction were found for micro-structure devices after their improvement of formidable heat and mass transfer in micro-channels. For this reason this system had the potential to reduce the reactor size. The catalyst effectiveness was extremely high in micro-structure reactors for such small reaction volumes. The other promising possibility of the new reactor concept included the driving down of the reaction temperature due to advantages of the high-performance catalysts in the favourable low temperature equilibria when the exothermic reaction heat is removed [5].

Many papers described advance testing of micro-structured reactors/heat exchangers for water-gas shift reactors to improve their heat and mass transfer and catalyst adapting according to the requirements of the new application. Dokupil et al. [1] focused on a propane fuel processor for an auxiliary power unit application. The system included the two adiabatic WGS reactors with the ceramic monolith, which were coated with the precious metal catalysts. The CO concentration was reduced from 12 mol.% to 1 mol.% at 280 °C. The reactors were operated with GHSV of 20000 h⁻¹ and 10000 h⁻¹ for medium (MTS) and low temperature (LTS) catalysts, respectively. The temperature increases of 68 K for MTS and 15 K for LTS were determined. Auto thermal reforming (ATR) systems were investigated by Roychoudhury et al. [2] in addition to monolith-based water-gas shift (WGS) reactors. The CO conversion increased from 10 % to 50 % after the variation of GHSV between 50000 h⁻¹ and 5000 h⁻¹ and under the following reaction conditions: CO = 3.6 %, H₂O/CO = 2.6 and T = 280 °C. Kolb et al. [3] tested the complete 5kW fuel processor for iso-octane for mobile auxiliary power units including two water-gas shift reactors. High-temperature WGS carried out by cross-flow cooling

channels fed with the gas in three stages and for low temperature WGS was provided by an un-cooled monolithic reactor. The same catalyst was chosen for both HTS and LTS reactors. The inlet CO concentration had 10 vol.% for HTS and 2.6 vol.% for LTS with a maximum WHSV of 9.5 NL/(h g_{cat.}) for HTS and 18.8 NL/(h g_{cat.}) for LTS. The highest CO conversion of 90 % for HTS and 82 % for LTS was achieved at 260 °C under WHSV of 39 NL/(h g_{cat.}) and 17 NL/(h g_{cat.}), respectively.

An integrated water-gas shift reactor/heat exchanger designed for 2 kW fuel cell systems was presented by Kolb et al. [4]. The internal temperature profile of the reactor was determined. A high initial rate of reaction required a lower temperature at the reactor inlet. The reactor temperature decreased gradually leading to a carbon monoxide reduction with a CO conversion of 91%. The WGS reactors were 200 mm long, 120 mm wide and 120 mm or 130 mm high for HTS or LTS reactors. The numbers of foils were 110 with 16000 channels in the HTS reactor and 130 foils containing 19000 channels in the second LTS reactor. The channel dimensions were 600 μm width and 800 μm height for both reactors. 1 wt.% Pt/CeO₂ on an alumina layer was used as the catalyst for WGS reactions. A gas with a CO content of 9.4 mol.% was fed to the HT-WGS operated under a WHSV of 38 Ndm³(hg_{cat.})⁻¹ and 1 mol.% of CO was achieved after the reaction.

A LTS reactor was operated under a WHSV of 33 Ndm³(hg_{cat.})⁻¹ and a CO product of 0.6 mol.% was detected. The highly-active Pt/CeO₂/Al₂O₃ catalyst for medium temperature of WGS between HTS and LTS was applied for the sandwich-type reactor (HCR) and showed long-term stability. The catalyst tests were performed first under a total flow rate of 60 N cm³/min and a corresponding WHSV of 200 N dm³/(h g_{cat.}) [24].

Tonkovich et al. [5] performed the water-gas shift catalysts in a plug-flow reactor. The 5% Ru/ZrO₂ powder catalysts were fabricated on nickel foam support. The catalysts were packed in a 7 mm ID quartz tube with the thickness from 0.5 to 2.5 cm. The highest CO conversion of 99.8 % was measured at 300 °C and a steam to carbon ratio of 3:1. The equilibrium conversion of 99.93 % was calculated for the same inlet gas containing 5 % of CO concentration and 50 ms.

However, the monolithic catalyst was found to be most efficient at 500 °C under the same gas mixture concentration and flow and reached the CO conversion of 94 %.

The WGS catalyst systems can produce very low CO concentrations only at low temperatures, which are favoured by thermodynamics. For this reason, most of the published work has focussed on precious metal catalysts such as Ru/Fe₂O₃, Au/Fe₂O₃ and Au/TiO₂, with high CO conversion activities at 200°C [5, 7, 8].

Other groups of WGS catalysts are precious metals supported on ceria [9-13] or zirconia [12, 14–16]. The ceria produced 2% CH₄ at 400°C in the dry gas at high space velocity. Goerke et al. [6] applied the WGS catalysts such as 3 wt.% Au/CeO₂ and 5 wt.% Ru/ZrO₂ onto 25 micro-structured foils made of Fecralloy and stainless steel. The catalysts' mass for foil surface area was reached at 0.44 mg/cm² of the Au/CeO₂ and 7.4 mg/cm² of the Ru/ZrO₂ catalyst. The Ru/ZrO₂ catalyst, which was distributed on Fecralloy, achieved 96 % CO conversion at 310 °C, 20 ms and with a gas mixture containing 25 vol.% of CO, 25 vol.% of H₂O and 50 vol.% of N₂. Compared to the Ru-catalyst, the Au/CeO₂ catalyst achieved only 3.4 % of CO conversion at 370 %. However, the Ru/ZrO₂ catalyst showed a CO conversion of up to 95 % at 340 °C under 3 vol.% CO and above 270 °C at 1 vol.% CO.

The goal of this thesis was the preparation and optimization of catalysts for the water-gas shift reaction in a microchannel reactor with the aim of generating hydrogen for mobile fuel cell systems. The catalysts additionally had to exhibit high catalytic activity and strong adhesion to support foils and prove long-term stability to be approved for common usage. The results of this experimental work mentioned in Chapter 4 have been published in journal Energy & Fuels [121], and the results written in Chapter 5-6 have been submitted in journal Chemical Engineering Communications too [116, 122].

Chapter 2 introduces fundamental aspects of the water-gas shift (WGS) reaction. The different types of WGS reactors and WGS catalysts will be presented in this chapter along with a detailed literature review. The

variety of the catalyst coating techniques on the structured surfaces, including a literature survey, is also described. The catalyst characterization methods of the coated WGS catalyst layers which are used for the WGS reaction tests will be presented in Chapter 3. The design of the WGS test ring, which was implemented for the experimental part of this thesis, is also outlined in this chapter.

In Chapter 4, the wash coatings were prepared from commercially available dry-milled powder catalysts. The commercial catalysts (PtX, PtY, RuZ, and CuXY) were prepared using a milling process. Adhesion characteristics were investigated as a function of the particle sizes of the powder catalysts. Influences of preparation methods, reduction treatments, and concentrations of the gases for HTS and LTS reaction conditions were studied.

In Chapter 5, the alumina and cerium dioxide wash coats were obtained by spin coating. The coating parameters such as suspension-pH, binder (PVA) molecular weight and solid loading were varied to optimize the homogeneous, well-adhered layer with good thermal stability and high surface area for water-gas shift reaction on microstructures.

Chapter 6 focuses on the possibilities using microstructured reactors after the adapting of Pt catalysts such as Pt/CeO₂/Al₂O₃ and Pt/CeO₂ on microchannel foils for the one-step water-gas shift reaction at low reaction temperatures. Microstructured reactors allowed the creation of more compact and efficient systems thanks to new microchannel devices with the promising possibility of deposition of high surface-area catalysts. This remained a main impact factor which influenced the better catalyst dispersion and better catalyst usage, especially for small amounts of expensive precious metals.

CHAPTER A

THEORY

LITERATURE REVIEW

STATE OF THE ART

2 FUNDAMENTALS

2.1 WATER-GAS SHIFT IN MICROSTRUCTURED REACTORS

The process chart developed for the coupled SOFC – PEFC system within this work is shown in Figure 1. The synthesis gas from the diesel reformer is fed to the

SOFC. The off-gas of the SOFC still contains carbon monoxide. As carbon monoxide is detrimental to the catalyst of the PEFC, a gas cleaning step has to be introduced.

A High Temperature Shift-Reactor (HTS) and a Low Temperature Shift-Reactor (LTS) for CO reduction by water-gas shift reaction are introduced as the gas cleaning step.

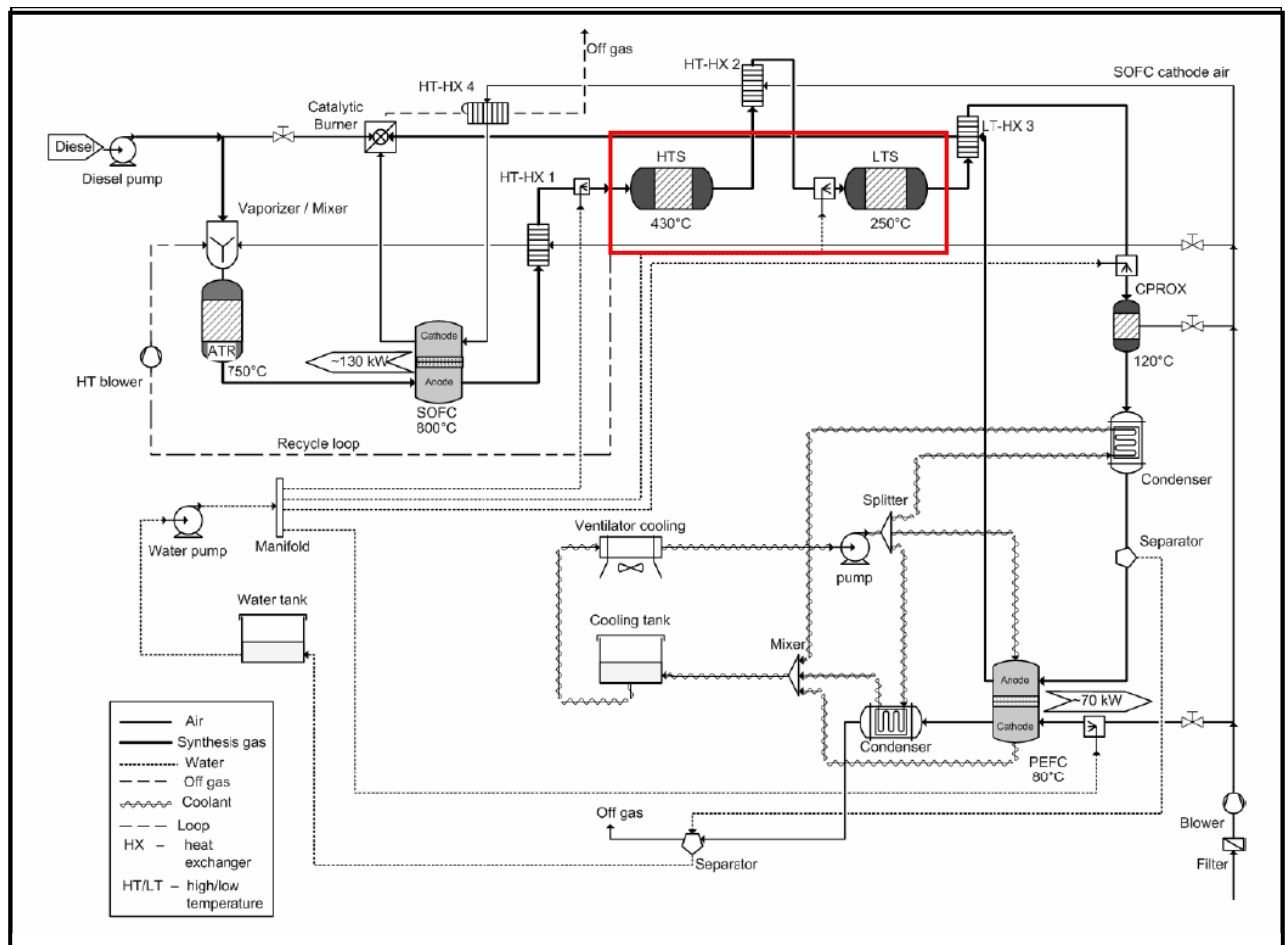


Figure 1 Process Chart for the coupled SOFC-PEFC system.

2.2 WATER-GAS SHIFT REACTION

The oxidation reaction of carbon monoxide with steam is called the water-gas shift (WGS) reaction, Eq (1).



The thermodynamic equilibrium constant can be calculated according to the following formula (2):

$$K(T) = \exp\left(\frac{4577.8}{T} - 4.33\right) \quad \text{Equation 2}$$

The WGS reaction represented an important step in the industrial production of hydrogen and has been used in industrial processes since the early 1940s. The essential role of the industrial WGS reaction is to adjust the CO/H₂ ratio of synthesis gas needed for further processes, e.g. methanol synthesis and ammonia synthesis.

It has found new significance in fuel processing in conjunction with fuel cells. The WGS reaction is reversible and exothermic and due to its moderate exothermicity the WGS reaction is thermodynamically unfavourable at elevated temperatures. This is illustrated by the continuous decline and eventual sign change in the Gibbs free energy as a function of temperature, and the corresponding decreasing equilibrium constant as temperature increases (Figure 2). Of course, the kinetic of the catalytic reaction is more favourable at higher temperatures.

The water content has a strong influence on the CO-conversion. The water content entering the WGS reactor can be varied by controlling the amount added

in the reformer and by injecting water. In addition CO, CO₂ and H₂ concentrations are mainly dependent on the reformer operating temperature, which in turn determines the thermodynamic limitations. In order to overcome this thermodynamic limitation while maintaining high reaction rates, WGS is normally conducted in multiple adiabatic stages with inter-stage cooling to obtain higher conversions overall, i.e., high temperature shift (HTS) is conducted in the first stage where operation temperatures range from 350 °C to 600 °C, while low temperature shift (LTS) occurs in the second stage with a temperature range of 150 °C to 300 °C.

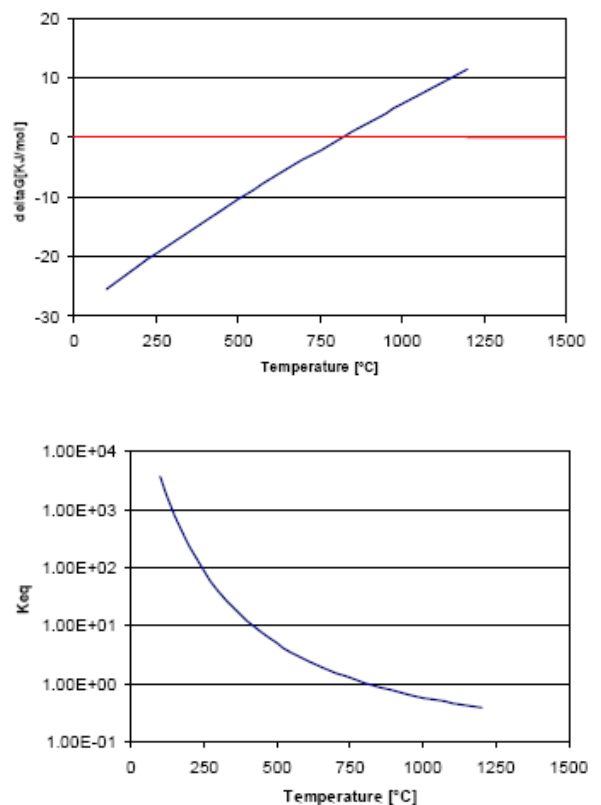


Figure 2 Thermodynamic equilibrium of the WGS reaction as described by the Gibbs free energy change and the equilibrium constant of the reaction as function of temperature.

2.3 WATER-GAS SHIFT REACTORS

2.3.1 MONOLITHIC REACTORS

Dokupil et al. [1] focused on a propane fuel processor for auxiliary power unit application. The system included the two adiabatic WGS reactors with the ceramic monolith, which were coated with the precious metal catalysts. The CO-concentration was reduced from 12 mol.% to 1 mol.% at 280 °C. The reactors were operated with GHSV of 20000 h⁻¹ and 10000 h⁻¹ for medium (MTS) and low temperature (LTS) catalysts respectively. The temperature increases of 68 K for MTS and 15 K for LTS were determined.

The auto thermal reforming (ATR) system in addition to monolith-based water-gas shift (WGS) reactors was investigated by Roychoudhury et al. [2]. The CO-conversion increased from 10 % to 50 % after variation of GHSV between 50000 h⁻¹ and 5000 h⁻¹ and under the following reaction conditions: CO = 3.6 %, H₂O/CO = 2.6 and T = 280 °C.

2.3.2 PLATE HEAT-EXCHANGER REACTORS

Kolb et al. [3] tested the complete 5kW fuel processor for iso-octane for mobile auxiliary power units including two water-gas shifts reactors. High temperature WGS carried by cross-flow cooling channels fed with the gas in three stages and for low temperature WGS was provided by uncooled monolithic reactor. For both HTS and LTS reactors, the same catalyst was chosen. The inlet CO-concentration was 10 for HTS and 2.6 vol.% for LTS and a maximum WHSV in the range of 9.5 NL/(h g_{cat.}) for HTS and 18.8 NL/(h g_{cat.}) for LTS. The highest CO-conversion of 90 % for HTS and 82 % for LTS was performed at 260 °C under WHSV of 39 NL/(h g_{cat.}) and 17 NL/(h g_{cat.}) respectively.

An integrated water-gas shift reactor/heat exchanger designed for 2 kW fuel cell systems is presented by Kolb et al. [4]. The internal temperature profile of the reactor was determined. A high initial rate of reaction required a lower temperature at the reactor inlet. The reactor temperature decreases gradually leading to carbon monoxide reduction with a CO-conversion of 91%. The WGS reactors were 200 mm large, 120 mm wide and 120 mm or 130 mm high for HTS or LTS reactor. The numbers of foils were 110 with 16000 channels in HTS reactor and 130 foils containing 19000 channels in the second LTS reactor. The channel dimensions were 600µm width and 800 µm high for both reactors. A 1 wt.% Pt/CeO₂ on alumina layer was used as catalyst for WGTS reactions. A gas with a CO content of 9.4 mol.% was fed to HT-WGS operated under WHSV of 38 Ndm³(h·g_{cat.})⁻¹ and a 1 mol.% of CO was achieved after reaction. A LTS reactor was operated under WHSV of 33 Ndm³(h·g_{cat.})⁻¹ and a CO product in range of 0.6 mol.% was detected.

2.3.3 WATER-GAS SHIFT REACTION IN MICROSTRUCTURES

Tonkovich et al. [5] performed the water-gas shift catalysts in a plug flow reactor. The 5% Ru/ZrO₂ catalysts as powder catalyst and catalyst were fabricated on nickel foam support. The catalysts were packed in a 7 mm ID quartz tube with the thickness from 0.5 to 2.5 cm. Their catalytic activities were compared under WGS-reaction conditions. The highest CO-conversion of 99.8 % was measured at 300 °C and a steam-to-carbon ratio of 3:1. The equilibrium conversion of 99.93 % was calculated for the same inlet gas containing 5 % of CO concentration and 50 ms. However, the monolithic catalyst under the same gas mixture flow and concentration showed to be most efficient at 500 °C, where the CO-conversion reached 94 %.

2.3.4 STACK-LIKE REAKTOR **APPLIED TO WATER GAS** **SHIFT**

Goerke et al. [6] applied the WGS catalysts such as 3 wt.% Au/CeO₂ and 5 wt.% Ru/ZrO₂ onto 25 microstructured foils made of Fecralloy and stainless steel. The catalysts' mass for foil surface area were reached at 0.44 mg/cm² of the Au/CeO₂-and 7.4 mg/cm² of the Ru/ZrO₂-catalyst respectively. The Ru/ZrO₂ catalyst, which was distributed on Fecralloy, achieved 96 % of CO-conversion at 340 °C, 20 ms and at a gas mixture containing 25 vol.% of CO, 25 vol.% of H₂O and 50 vol.% of N₂. Compared to the Ru-catalyst, the Au/CeO₂ catalyst reached only 3.4 % of CO-conversion at 340 °C. However, the Ru/ZrO₂-catalyst showed the CO-conversion exceeded 95 % under low-temperature water-gas shift reactor at 340 °C and CO-content of 3 vol.% and at 270 °C for 1 vol.% CO.

2.3.5 SANDWICH-TYPE REACTOR **(HCR)**

Kolb et al. [24] optimized the high active catalyst for medium temperature of WGS between HTS and LTS. The Pt/CeO₂/Al₂O₃ catalyst was applied for HCR and showed long term stability.

The catalyst tests were performed first under a total flow rate of 60 N cm³/min and corresponding WHSV of 200 N dm³/(h g_{cat}). The 4 wt.% Pt/17 wt.% CeO₂/Al₂O₃ sample showed higher CO-conversion (35 % at 340 °C) compared to the 4 wt.% Pt/3 wt.% Pd/ 12 wt.% CeO₂/Al₂O₃-catalyst under LTS reaction conditions. No methane fraction was detected for either sample in off-gas. The reaction temperature for HTS was kept below 400 °C due to methanation reaction, which is starting at 400 °C for Pt. Thus the activity of the P/CeO₂/Al₂O₃ sample was still too low (55% at 390 °C). After catalyst calcination at 450 °C instead 600 °C, both samples 5 wt.% Pt/12 wt.%CeO₂ and 3 wt.% Pt/24 wt.%CeO₂ showed the highest CO-conversion rate (86 % at 290

°C) near the thermodynamic equilibrium. Therefore the flow rate was increased from 30 Ncm³/min to 60 Ncm³/min. Finally, the highest CO-conversion in the range of 64 % at 340 °C for LTS and 81 % at 365 °C for HTS was found for the 5 wt.% Pt/12 wt.%CeO₂/Al₂O₃ catalyst sample.

2.4 WATER-GAS SHIFT **CATALYSTS**

The requirements for fuel processing are different compared to the industrial WGS catalysts used, due to frequent start-ups and shut-downs of the water-gas shift reactors in a mobile fuel processing system.

The operation requirements for the commercial water-gas shift catalysts such as Fe/Cr and Cu/Zn/Al very often required reactor start-ups and shut-downs and a controlled reduction which activated the catalyst before reaction. To prevent the condensation and re-oxidation of the catalyst after each shut-down of the water-gas shift system, the inert gas needed to be purged through the reactor. The problems of pyrophoricity and deactivation through air exposure may be solved by the application of precious metal catalysts. However, conventional catalysts are still very important in fuel processing for reasons of long-term performance, low cost and low activity temperature.

2.4.1 NON-PRECIOUS-METAL- **CATALYSTS**

Not all WGS catalyst development has focussed on precious metals. Alternative concepts include transition metal carbides, copper or nickel supported on ceria, or cobalt on perovskite, which have lower cost base metal formulations while striving to overcome the pyrophoricity of commercial catalysts.

The given CO conversion rates for the Cu/ZnO/Al₂O₃-catalyst are 86% calcined at 500°C and 61% at 900°C.

Relatively high CO conversions were found at lower water vapour concentrations (<15%) [18].

The activity of the Cu/CeO₂ catalyst was more active than ceria at the much lower temperature range of 175-300°C. The conversion of CO was kept below 15% [19]. Without pre-treatment or activation, the conversion of CO was also kept below 15% for Ni-loaded cerium oxide catalysts in the LTS temperature range of 250-300°C [19].

The H₂ selectivity of the Ni/SiO₂ catalyst was ten times higher than on the Ni/Al₂O₃, which on the other hand had a higher methane conversion. It was proved that the effect of the acid/base groups on the alumina supports play a significantly role in the reaction mechanism. The silica support appeared to have no effect on the reaction mechanism.

2.4.2 PRECIOUS-METAL CATALYSTS

The WGS catalyst systems can produce very low CO concentrations only at low temperatures which are favoured by thermodynamics. For this reason, most of the published work has focussed on precious metal catalysts such as Ru/Fe₂O₃, Au/Fe₂O₃ and Au/TiO₂, with high CO conversion activities at 200°C [7-9].

The catalyst activity differences for both Au/Fe₂O₃ and Au/TiO₂ were correlated with their supports. In contrast to the TiO₂-catalyst with no activity, the Fe₂O₃-support catalyst showed high activity at the same high temperatures. Otherwise, Au catalysts on those supports exhibit similar activity compared to Cu/ZnO - LTS WGS catalyst [21].

The activity order in the WGS reaction for Ru-catalysts was found to be: Ru/La₂O₃ > Ru/Fe₂O₃ >> Ru/Fe₂O₃ > Ru/MgO >> Ru/C. The acidic character of the Ru-catalyst supports exhibit higher activity compared to those supported on basic oxides. It was also observed that the excess of steam (H₂O/CO ratio was 2.5) stabilizes the Fe₃O₄ structure during the WGS reaction [13].

The Ir-catalyst was found to be the least active noble metal compared the activity of alumina supported

Group VII B, VIII and I B metals [15]. The effect of the support adsorption of CO over supported Ir was observed in the following order: TiO₂ > Al₂O₃ > SiO₂ > MgO at 623 K.

The CO conversion was found to decrease in the order Ir/TiO₂ > Ir/Al₂O₃ > Ir/SiO₂ ≥ Ir/MgO [8]. Increasing the CO concentration only for Ir/TiO₂ and Ir/SiO₂ slightly changed the amounts of CO₂ and H₂ formed with the fact that formate may be formed on TiO₂ and not on SiO₂.

In the case of Pt/Al₂O₃ and Pt-CeO₂/Al₂O₃ catalysts, the Pt/Al₂O₃ does not show any CO₂ present due to the catalyst reduction at 973 K. In the case of Pt-CeO₂/Al₂O₃, CO₂ was found to be present, which was started at 413 K.

Other groups of WGS-catalysts are precious metals supported on ceria [10-14] or zirconia [14-17]. The ceria produced 2% CH₄ at 400°C in the dry gas at high space velocity catalyst. On the other hand, the commercial Fe/Cr/Cu catalyst did not reach equilibrium conversion until 450°C but no CH₄ was detected (Fig.3).

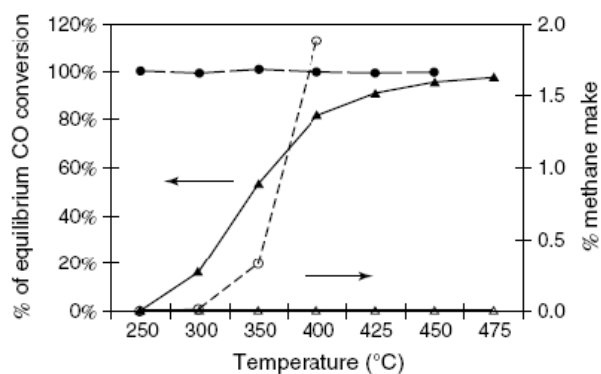


Figure 3 Selectivity of WGS catalysts. (▲, Δ) Commercial Fe/Cr/Cu, (●, ○) 2% Pt/CeO₂. HTS syngas, total gas SV=45000h⁻¹, S/G=0.5 [120].

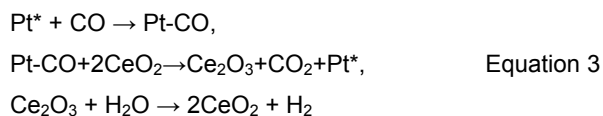
2.4.2.1 Pt/ CeO₂ CATALYST FOR WGS REACTION

Pt/CeO₂ has raised interest for the WGS reaction since the late 1970s, when its high CO conversion activity was discovered. Different groups have reported that

ceria-supported platinum catalysts are more active than alumina supported ones. Recently, the Pt/CeO₂ catalyst has received new interest in the context of fuel cells, as these catalysts are highly active in the range of 250-400°C, and they are nonpyrophoric and do not require any pre-treatment before use.

The WGS reaction mechanism for Pt/ceria catalysts is clearly different than for copper-based catalysts. The WGS reaction proceeds via a bi-functional mechanism (Eq. 3):

- a) The ceria is “temporarily” reduced (Ce⁴⁺ → Ce³⁺) and donates an oxygen ion for the oxidation of carbon monoxide to carbon dioxide
- b) Platinum catalyzes the reduction of water to hydrogen, thus liberating an oxygen ion that re-oxidizes the ceria (Ce³⁺ → Ce⁴⁺). Thus, the mechanism is similar to the “oxygen storage capability” principle that is exploited in ceria-based catalysts used in automotive catalytic converters [20].



Several advantages of Pt/ceria WGS catalysts were demonstrated compared to existing copper-based catalysts:

- Pt/ceria WGS catalysts are sufficiently active and offer a number of practical advantages for fuel processors of PEM fuel cell systems
- They are more active than existing copper-based low-temperature shift catalysts above 250°C, and substantially more active than iron-chrome-based high temperature shift catalysts
- Optimization of formulations and processing required minimizing long-term deactivation of Pt/ceria catalysts. Regeneration of deactivated catalysts can be achieved by heating in air.
- Operation over wide temperature range
- Pt/ceria catalysts can be washcoated using conventional technologies. Washcoating of this catalyst provides a variable path for achieving rugged and volumetrically efficient packaging of catalysts in WGS reactors of automotive fuel processors.

- Resistance to degradation by oxidation, condensation, temperature cycling and to vibrations (ruggedness)
- Non-pyrophoric catalyst
- Potential for lower size/weight/cost (with optimum platinum utilization)

2.4.2.2 Pt/CeO₂/Al₂O₃ CATALYST FOR WGS REACTION IN MICROREACTORS

Table 1 shows several Pt/CeO₂/Al₂O₃ catalysts which were applied for different WGS reactor types. The physical and chemical properties of the catalyst and the CO conversion levels under various reaction conditions (reaction temperature, total flow and inlet gas composition) are additionally presented.

Several 1-2 wt.% Pt/10-20 wt.% CeO₂/Al₂O₃ catalyst samples were prepared by a sol-gel method. The surface area of the catalyst coatings on the microstructured platelets was very high and reached 330 m²/g. The influence of the Pt and CeO₂ amount on their catalytic activity was investigated under a reformat gas at the outlet of an autothermal gasoline reformer with an H₂O/CO of 2.4. The highest activity range was found between the reaction temperatures of 300 and 400 °C. The 1 wt.% Pt/10 wt.% CeO₂/Al₂O₃ catalyst exhibited the better platinum utilization and the maximum CO conversion was 10 % higher for the catalyst layer deposited on microstructured platelets at 380 °C and 47.6 Ndm³/(h g_{cat}) of WHSV than for its powder sample [22].

The platinum/ceria/alumina catalyst preparation methods, such as incipient wetness impregnation with a cerium and then platinum precursor solutions, were performed on the wash-coated alumina layer using the same microchannel stainless-steel platelets [23-25].

The 1% Pt/CeO₂/Al₂O₃ catalyst was applied for the high temperature as well as for the low temperature WGS reactor completing the fuel cell system, which was running on iso-octane. This catalyst obtained up to 90

% CO conversion under a WHSV of 48-98 Ndm³/(h g_{cat}) in a first-stage reactor and less than 50 ppm CO in the outlet of the second LTS-reactor [23]. The final 1.2 wt.% Pt/4.8 wt.% CeO₂/Al₂O₃ catalyst with the much lower surface area of 72 m²/g surprisingly showed 80 % CO conversion at the lower 260 °C operation temperature. However, the CO-conversion result was 10 % higher than for the above-mentioned 1 wt.%Pt/10wt.CeO₂/Al₂O₃; the WHSV was only 9.4 Ndm³/(h g_{cat}) [25]. The other catalysts, such as 4 wt.%

Pt/17 wt.% CeO₂/Al₂O₃, showed higher CO conversions of 35 % at 340 °C compared to the 4 wt.% Pt/3 wt.% Pd/ 12 wt.% CeO₂/Al₂O₃ catalyst under LTS reaction conditions.

No methane fraction was detected for either sample in the off-gas. The reaction temperature for LTS was kept below 400 °C due to the methanation reaction, which starts at 400 °C for Pt. Thus the activity of the Pt/CeO₂/Al₂O₃ sample was still too low for 55% CO conversion at 390 °C.

Table 1 Physical and chemical properties of the platinum catalyst based on the literature

Pt. wt.% [mg]	Catalyst			Coating method	BET SA [m ² /g]	WHSV [Ndm ³ / (h g _{cat})]	Total flow [ml n/min]	Gas content [vol.%]	CO- conv. [%]	Tr** [°C]	Ref.
	CeO ₂ wt.% [mg]	Al ₂ O ₃ wt.% [mg]	Cat. [mg]								
0.9 (1.5)	9.8 (16.1)	89.3 (146.4)	164			73.2			59	420	[22]
1.4 (3.5)	8.3 (20.9)	90.3 (227.6)	252			47.6			70	380	
0.8 (1.6)	20 (40)	79.2 (158.4)	200			60			60	410	
3 (0.4)	24 (3.6)		19,05	IW*-impr.	66	200			80	365	[24]
5 (0.7)	12 (1.8)		17,55	IW*-impr.	69				81	365	
1.2 (7.4)	4.8 (30.4)	94.05 (598.2)	636	IW*-impr.	72	9.4	100	0.1bar-P(CO ₂), 0.1bar-P(CO), 0.2bar-P(H ₂ O), 0.3bar-P(H ₂) in Ar	80	260	[25]
0.8 0.9	3.4 3.4 Ce	46.4 Al	232 (HTS) 274 (LTS)	IW*-impr., dipping	72, 62	39-41 17-32	200-40	10CO, 20H ₂ O, 30H ₂ , 10CO ₂ , 30Ar; 2.6CO, 27.5H ₂ O, 33.8H ₂ , 13CO ₂ , 23.1Ar	90 80 75 82	260 (40 ml/min) 280 (100 ml/min) 280 (200 ml/min) 260 (100 ml/min)	[23]

*-incipient wetness impregnation, **- reaction temperature

After catalyst calcination at 450 °C instead 600 °C, both the 5 wt.% Pt/12 wt.%CeO₂ and 3 wt.% Pt/24 wt.%CeO₂ samples showed the highest CO conversion rate of 86 % at 290 °C, which was near the thermodynamic equilibrium. Therefore the flow rate was increased from 30 Ncm³/min to 60 Ncm³/min. Finally, the highest CO conversion of 64 % at 340 °C for LTS and 81 % at 365 °C for HTS was found with the 5 wt.% Pt/12 wt.%CeO₂/Al₂O₃ catalyst sample [24].

2.5 WGS CATALYST APPLICATIONS

Before the novel WGS catalysts will be successfully applied, many barriers and operation conditions must be changed to achieve the desired requirements of the WGS catalyst used in mobile applications (Table 2). The operability, size, weight and cost targets are rigorous because of the standards set by internal combustion engines. The most important targets are concentrated on the reduction of the volume, weight and cost of the catalyst, which could be attained only when the activity of the catalyst increases. Based on Department of Energy projections, those targets are at least ten times lower than expected [27].

Table 2 WGS catalyst requirements for mobile applications [27]

WGS catalyst attribute	Mobile application
Volume reduction	Critical, <0.1 l kW ⁻¹
Weight reduction	Critical, <0.1 kg kW ⁻¹
Cost	Critical, <\$1 kW ⁻¹
Rapid response	Critical, <15 s
Nonpyrophoric	Important
Attrition resistance	Critical
Selectivity	Critical
No reduction required	Critical
Oxidation tolerant	Critical
Condensation tolerant	Important
Poison tolerant	Desired
Pressure drop	Important

The relative costs of precious metal and of conventional catalysts are:

- Cost of Fe/Cr/Cu and Cu/Zn catalysts are \$10.6 l⁻¹ and \$17.3 l⁻¹, respectively
- Precious metal catalyst: Pt loading at 2 wt% and washcoat loading of 150 g l⁻¹, precious metal cost is 40% of the total catalyst cost, platinum price 38 \$/g, results in 285 \$ l⁻¹

The precious metal catalyst activity has to be increased at least ten times to be competitive on a cost basis. Previous information has shown that the activity must be improved over one hundred times to meet activity requirements for fuel processing. Precious metal catalysts may be profitably compared to the Cu/Zn and Fe/Cr/Cu catalysts if the durability and redox resistance can be proven [27].

2.6 THE ADVANTAGES AND DRAWBACKS OF MICROSTRUCTURED DEVICES

A fuel processor is a complex device which converts conventional fuels such as gasoline or a renewable fuel such as ethanol into hydrogen. Inexpensive fabrication techniques feasible for mass production need to be applied for fuel processors. Catalyst cost may also play a significant role in the overall fuel processor cost and may reach values as high as 38%. Here the microstructured devices offer significant possibilities for cost reduction owing to the improved mass transfer in small channel systems, which allow a highly-efficient usage of the catalyst.

Microstructured devices allow for rapid system stabilization due to the fast dynamic response because of the low residence times applied. Microstructured reactors enable improved catalyst effectiveness and microstructured heat exchangers work at a high efficiency/volume ratio, thus leading to a substantial size reduction potential.

The weight of fuel processing devices is determined by their size and by the material employed. Therefore, a trade-off is necessary for each system and its individual components comparing the benefits of size reduction achieved by applying microstructured devices against the surplus of weight.

Microstructured devices offer benefits concerning the load-change behaviour of fuel processors owing to the small fluid volumes applied.

Various design concepts of microstructured reactors have been realized:

- Testing reactors: these are normally externally or electrically heated and may carry either single plates, a sandwich of plates or stacks of microstructured plates. They serve mostly for catalyst development purposes and to prove the feasibility of design concept.
- Chip-like reactors: these devices utilize the potential of miniaturization and cheap mass production applying silicon as construction material. Future applications are mostly low-power systems.
- Integrated reactors: one type of integrated reactor is microstructured heat exchanger/reactor concepts, which may work as cross- or counter-flow reactors.

Another type couples endothermic and exothermic reactions in two separate flow paths normally operated in the co-current mode. Both reactors are designed as prototype components of future fuel processors for mobile applications.

To achieve the maximum performance, opportunities exist to apply novel reactor concepts to fuel processing. If the exothermic heat of reaction can be removed from the reactor, the thermodynamics can be exploited by driving down the exit temperatures.

Microchannel reactors appear to be able to accomplish the formidable heat transfer task while achieving small reactor volumes. However, it will require high performance catalysts to take advantage of the favourable low temperature equilibria [5].

2.7 CATALYST COATING TECHNIQUES

In order to functionalize microstructured components for heterogeneously-catalysed reactions, the catalytically active layer has to be fixed within the microstructure. Often it is difficult to achieve strong adhesion of the catalyst coating on the microstructured material, which is made of silicon or metal. For some catalyzed reactions, the inner geometric surface area is too small to fix a sufficient number of active centres. It is therefore necessary to develop active coatings with a large surface area on microstructured metal carrier materials for impregnation with catalytically active substances (noble metals).

2.7.1 METALLIC SUBSTRATE PREPARATION

Before catalyst layer coating, the metallic support must be appropriately pre-treated to enhance the adherence for the first catalyst coat.

The ultrasonic cleaning in alkaline was used in a few papers to remove oil, primary oxidation and impurities [22, 30, 31, 33, 40, 42]. The acidic solution such as HNO_3 was needed to eliminate chloride ions after etching of the channels. The ethanol and acetone were also chosen to clean the surface from residues [26, 30, 32]. After that the plates were rinsed, usually with distillate water.

High temperature heat treatment of the foils was the second important pre-treatment step. The metal composition of the support material was the major factor by temperature selection. For the stainless steel the calcination temperature range was varied between 200 and 950 °C [6, 22, 29, 31, 35].

Fe-based alloys consisting of Al were in recent years very often the preferred support material to achieve a more porous, adhered structure for the coating. This

material also enabled the surface area of the catalyst to be increased. The calcination at 900 °C and under an oxidizing environment was facilitated by the migration of Al species from the bulk FeCrAlY alloy substrate to the surface, which is subsequently oxidized to form a native aluminium oxide layer (32, 36-38).

Well-adhered layers can be formed on FeCrAl metallic supports for the preparation of structured catalysts [6, 26, 33, 34, 40, 41, 43]. After heat treatment around 1000 °C, the oxide film was created to enhance the adhesion with catalyst layers. Valentini et al. [26] investigated the coating adherence of Al₂O₃ versus calcination temperature. It was found that after calcination the plate at 900 °C and 10 h the coat weight loss was only 0.08 % and was the lowest comparing the results at lower calcination temperatures of 400 and 700 °C. The continuation of the surface deformation the same material after higher temperature treatments (950 and 1050 °C) was presented by Zhao et al. [40]. They founded the same high adhesion level at 950 °C and 1050 °C after 10 h and 0.5 h respectively.

2.7.2 CATALYST COATING AS SUSPENSION

The catalyst coating on the microchannel plates were mostly achieved by deposition of the suspensions (tab. 3). This largely used suspension usually consisting of the standard ingredients such as powder, binder, acid and solvent. Their concentration and the desired layer thickness varied largely. In this case, the nature of the surface to coat was a great factor in obtaining the coating. The size of the suspended particles had a major influence on the adhesion and the BET surface area on the substrate by different oxides.

Aluminium was the most popular material deposited in the suspension mixture and was used as catalyst support. The suspension usually consists of powder, water, binder and acids for pH adjustment. Zapf et al. [44] prepared the gamma alumina slurry with the following composition such as 20 g gamma alumina (3

µm powder), 75 g deionized water, 5 g binder polyvinyl alcohol (Mw = 100000 g/mol) and 1 g acidic acid. After calcination of the layer at 600 °C for 1 h the surface specific area of 69 m²/g was achieved. The influence of microchannel diameters on alumina coating effect was investigated. A more uniform coat was found for 500 µm x 70 µm channels comparing the other diameters such as 500 µm x 300 µm and 750 µm x 300 µm. No cracks or uncoated surfaces were found and the loss of weight was noted as less than 1 %. The same suspension content and concentration for alumina or commercial catalyst slurries is to be found in many publications in the last four years [24, 35, 45, 46]. After deposition of support material in the microchannel, the excess suspension was wiped off by using a sharp blade [35].

The same type of alumina powder (3 µm) was mixed with a commercial methylhydroxyethyl-cellulose binder. Only minor cracks appeared on the layer after coating of aqueous suspension and calcination at 600 °C for 10 h. The coat thickness in the range of 39-24 µm proved a homogeneous deposition of the microstructured platelet. Additionally, the BET surface area of the alumina coat was decreased from 82 m²/g to 72 m²/g after the washcoating process. The largest lost of the layer was 1.7 % after exposure to ultrasounds for 30 min and no loss after dropping the coated plate from 50 cm was detected [25].

The three high molecular weight polymers (binders) such as PVA (Mw = 95000), Tylose (Mw = 95000) and PEG (Mw = 20000) as 0.5-25 wt.% were mixed in the suspension with 10 g alumina or commercial catalyst, 39.6 g water and 0.4 g of acidic acid. The coating's adhesion was similar to that mentioned before. The layer in the microchannel showed no cracks and a homogenous structure. It was found that the surface specific area decreases. For the suspension with Tylose (cellulose ether) 0.7 wt.% and PVA (polyvinyl alcohol) 2wt.% was above 26 m²/g lower compared to the original powder (68 m²/g). The highest loss of BET surface from 94 m²/g to 54 m²/g was found for PEG (polyethylene glycol) 15 wt.% and the lowest decrease to only 5 m²/g (89 m²/g) was noted for Tylose 0.7 wt.%

without acetic acid content in suspension. No acids added in the suspension with Tylose 0.7 wt. % led to the best adhesion and the highest catalyst activity. The layer thickness between 24 and 40 μm was estimated [29]. Another possibility of gamma Al_2O_3 (185 m^2/g) suspension was its addition to nitric acid solution with a concentration of 2 mol/l. Crack and catalyst layer deteriorations were only found for thicknesses of more than 40 μm [34]. However, the highly active and stable Rh/MgO- Al_2O_3 -catalyst was supported on a gamma Al_2O_3 -layer prepared only from Al_2O_3 -powder (225 m^2/g) and a water-in-weight ratio of 1 to 8 [36].

Pfeifer et al. [47] used the 20 wt. % ZnO nanoparticles (77 nm) or mixed nanoparticles such as CuO, ZnO, TiO_2 and gamma Al_2O_3 (41, 77, 26, 32 nm) [15] and dispersed them in an aqueous solution of 1 wt.% hydroxy ethyl cellulose (HEC) [47, 48] or with hydroxy propyl cellulose (HPC, $\text{Mw}=370000\text{g/mol}$) dissolved in isopropyl alcohol [30]. The foils were calcined at 450 $^\circ\text{C}$ for 5 h. The mean layer thickness was 20 μm . The conversion of methanol was nearly zero after 50 h for suspension with mixed oxides ratio CuO/ZnO = 50/50 dispersed in HEC/water [48].

The easier way to prepare the suspension based on nanometre particles was presented by Goerke et al. [6]. They suspended CeO_2 and ZrO_2 in ethyl alcohol or water and applied it on the foil made of stainless steel and Fecralloy. Adhesion of the premier coats was determined by using an adhesive tape. Adhesion of catalyst supported on ZrO_2 was good compared to CeO_2 -catalyst layers that were not well-adhered, but it was still sufficient to carry out the reaction tests. No significant differences in layer thickness were detected after coating on the different metallic material (DIN 1.4301 and 1.4767) for ZrO_2 -catalysts (1-10 μm).

In the case of Villegas [50], the first support layer was prepared as a mixture consisting of three different boehmites $\text{Al}_2\text{O}_3\cdot\text{H}_2\text{O}$ and one $\gamma\text{-Al}_2\text{O}_3$ (3 μm). HCl was used as the dispersant for boehmites and HNO_3 for γ -

Al_2O_3 powder, than stirred for 15 h. $\alpha\text{-Al}_2\text{O}_3$ /water suspension was prepared by mixing the $\alpha\text{-Al}_2\text{O}_3$ powder with DI-water, which was presented by Pérez-Cadenas et al. [51]. In this work the pH was varied (3-8) using nitric acid and NaOH. It was also proved several times that the amount of alumina increased on the monolith walls with increasing pH and increasing alumina concentration in the suspension.

Some other interesting articles described the Al_2O_3 -suspension coating used as a catalyst distributed on the monoliths. The concentration of solid material in a suspension varied largely and influenced the desired layer thickness, which also depends on the nature of the surface to coat. Agrafiotis et al. [49] showed that the size of the suspended particles has a great influence on the adhesion on the substrate in the case of monolith coating by different oxides. Particle size diameter in the range of 2 μm lead to much more adherent layers than 17 or 52 μm for $\gamma\text{-Al}_2\text{O}_3$ washcoats. The slurries contained 35 wt% of solids.

Table 3 Suspension method used for catalyst coating onto microchannel foils

Substrate material, channel dimensions	Catalyst	Additives	T_{calc} [°C]; t [h]	BET $\left[\frac{m^2}{g} \right]$	Layer thickness [μ m]	Layer quality	Adhesion (loss after adhesion tests)	Ref.
500 x 300 μ m 750 x 300 μ m 500 x 70 μ m	γ -Al ₂ O ₃ (CuO/Cr ₂ O ₃ / Al ₂ O ₃)	γ -Al ₂ O ₃ -powder(3 μ m), water, polyvinyl alcohol (PVA), HNO ₃	600; 1	69	20-70 10-20	Cracks free, no uncovered surfaces	1 wt.% (drop test)	44
500 x 250 μ m	γ -Al ₂ O ₃ (Pt/Rh/CeO ₂ , Pt/CeO ₂ , Pt/Pd/CeO ₂)	γ -Al ₂ O ₃ -powder(3 μ m), water, polyvinyl alcohol (PVA), HNO ₃	600; 2	64-67	17 mg	-	Stable at 340-365 °C for 50 min, feed rate: 30 N cm ³ /min	24
400 x 300 μ m 250 x 125 μ m 250 x 187 μ m	γ -Al ₂ O ₃ (Ru/CeO ₂ , Rh/CeO ₂ ,Pt- Ru, Pt-Co, Pt- Rh)	γ -Al ₂ O ₃ -powder(3 μ m), water, polyvinyl alcohol (PVA), HNO ₃	600; 2	238-50**	40, 250 mg	-	13 min stable (Pt-Ru) at 130°C, 20 h ⁻¹ , 40 °C (Rh), 21.5 h ⁻¹ , 50 °C Pt-Rh; GHSV: 15500h ⁻¹	46
DIN 1.4571 400 x 600 μ m	γ -Al ₂ O ₃ (Pt/CeO ₂ / Al ₂ O ₃)	γ -Al ₂ O ₃ -powder (3 μ m), water, methylhydroxyethylcellulose (MEC)	600	72	24-39	Minor cracks	1.7 wt.% (ultrasounds)	3 25
DIN 1.4571 400 x 600 μ m	γ -Al ₂ O ₃ C18-7	Powder, binders (PEG, Tylose, PVA)	300; 10	94-54	24-39	Free of cracs, homogeneous	2 wt.% (ultrasounds)	29
Aluminium plates, 100 x 100 μ m	a) ZnO b) Pd/ZnO	a) 1 wt.%HEC, 20 wt.% ZnO, H ₂ O; b) HEC, ZnO, H ₂ O, 10 wt.% Pd	450; 5	77nm (ZnO)	20	Very homogeneous	Good stability for 30 h under reaction conditions	47
Aluminium plates, 100 x 100 μ m	CuO, ZnO, TiO ₂ , γ -Al ₂ O ₃ (Nanophase)	a) HEC, H ₂ O b) HPC, isopropyl alcohol	450; 5	7-22, 5	20	Non-obvious change in structure after milling	Good adhesion due to surface roughness and an oxidised aluminium surface	48
Stainless steel (DIN 1.4301), Fecralloy (DIN 1.4767)	CeO ₂ , ZrO ₂ -nanopowders	CeO ₂ -powder with ethyl alcohol or water; ZrO ₂ -powder with water	950; 3 or 450; 1; 350; 1	1.01, 29.8 - Au/CeO ₂ 64.77, 79.32 - Ru/ZrO ₂	5-20, 0.3-3 (Au/CeO ₂); 1-10 (Ru/ZrO ₂)	Small cracks (Ru/ZrO ₂); large cracks (Au/CeO ₂)	Good – Ru/ZrO ₂ , lower – Au/CeO ₂ (tests with adhesive tape)	6
FeCrAl (DIN 1.4767), 100 x 600 μ m	γ -Al ₂ O ₃ (Cu/ZnO/ Al ₂ O ₃)	Al-powder (185 m ² /g), acetic acid	500; -	183	Min. 10 μ m, max. 40 μ m	No detachment and any uncovered areas	Very good, stable after 20h under r. cond. (282 °C, 9 cm ³ /h)	34
FeCrAlY 0.03in. x 0.35in. x 2in.	γ -Al ₂ O ₃ (Ru/MgO- Al ₂ O ₃)	Al-powder (225 m ² /g), water	500; 2	225*	0.065 g	Powder dispersed on the metal fibres, pore size ~150 μ m	Stable 39 h after exposing in steam at 900 °C, contact time = 25 ms	36

*) as-received powder; **) after metal impregnation

2.7.3 SOL-GEL COATING

A solution or a colloidal dispersion of a chemical precursor was the initial point of the material for deposition (tab. 4). The precursor of the sol can be for example hydrated aluminium oxides (pseudo-boehmite or boehmite) [62, 72] or aluminium alkoxides [43, 31]. The ageing time allowing the gelation (peptisation) of the sol was an important factor in the sol-gel coating method, which takes from a few minutes to several weeks, depending on the concentrations in the sol and the size of the object to coat. Sol with high viscosities, obtained after long ageing times, allow the depositing of a thicker layer but are vulnerable to cracks. A compromise has to be found for each preparation and substrate to coat.

Zhao et al. [40] achieved a well-adhered γ -Al₂O₃-layer through double coating deposition. Primer deposition of boehmite sol was used to improve adhesion between the metallic support and alumina layer. After that the second sol containing dispersed γ -Al₂O₃ powder in boehmite sol with 35 wt.% solid content was applied. Both sols were deposited on the foil surfaces by dip coating with the withdrawal velocity of 3 min/min for 15 s. The optimal layer adhesion was found after calcination at 800 °C for 3 h and secondly at 900 °C for 2 h [40]. The catalyst slurry referred as sol-gel was made by adding 5 g of boehmite, 36.5 g of water, 0.4 g of acetic acid and 5 g of catalyst [29]. Conant et al. [60] chose another concentration for the slurry, which consisted of 10 mg of boehmite, 100 ml of DI water, 0.5 ml acetic acid and 25 mg of catalyst. The catalyst slurry was filled into the channels completely using the syringe and then air flow forced out the excess amount of suspension. However, nearly 75 wt.% of water in the slurry caused the layer to crack during drying and a loss of catalyst cohesion.

Hwang et al. [52] prepared the alumina sol and alumina-sol based slurry, which was made of aluminium isopropoxide, DI-water, 1.5 % PVA, HCl and/or commercial catalyst [61]. The two different deposition techniques were examined and compared: flow and fill-and-dry coating [52]. The pure alumina sol coating

without any drying additives (PVA) caused the layer to peel off. The addition of PVA to the sol prevented the layer shrinking during drying already. The alumina layer with the thickness of 0.3 μ m was successfully formed using air flow coating. However, the layer thickness was non-uniform after the alumina sol-based slurry coating inside the microchannels using both mentioned coating methods was coated. The particles in the layer showed high coherence, which caused difficulties in the blowing off of the excess sol from channels without creating any surface deterioration [52]. Boehmite-based sol-gel slurry coating on different structured materials by two deposition methods, dip-coating and spray-coating, was characterized by Meille et al. [62]. With the sol-gel coating using the dipping as the deposition method, the perfect uniform and adhered alumina layer appeared on the silicon material. Comparing the layer quality to those coated on Si-wafers, the alumina coat on the FeCrAlloy fibres showed cracks, non-uniformity, some uncovered areas and poor adherence. However, this problem with the inhomogeneous layer was avoided by choosing the spray-coating technique. A consequence of this deposition was a uniform coat with no weight losses after the ultrasound adhesion test [50].

Kundu et al. [31] achieved the uniform and stable coatings on the stainless steel microchannel plates. The three sols – alumina, zirconia and a mixture of them – were prepared. Aluminium secondary butoxide and zirconium (IV) propoxide were used as precursors. In addition, the acetylacetone, ethyl alcohol, water in a ratio of 2:1 with respect to alkoxide and nitric acid (pH=4.5) were added. The preparation of commercial catalyst-based slurry was undertaken by dispersing the catalyst in sols with weight ratio of 85:15. After six days of reactor operation the layer based on mixed sols (Al₂O₃+ZrO₂) exhibited the lowest catalyst loss, in the range of 15 wt.%, compared to the relatively unstable ZrO₂-coating because of crystalline structure building at 500 °C calcination temperature [31]. However, Lim et al. [58] and Won et al. [59] prepared more diluted catalyst slurries composed of catalyst, zirconia sol solution and isopropyl alcohol, no weight loss occurred. Even after ultrasonic treatments for 1h, it was found that the layer had no cracks. The catalyst layer was intact

after its exposure under reaction conditions for several days. They maintained the excellent adhesion between the catalyst layer and the microchannel.

Chen et al. [53] developed a thin-film deposition method for synthesized Pt/Al₂O₃ catalyst on the silicon channel plate. Hydrogen hexachloroplatine (IV) hydrate was dissolved in 1.3 butanediol. The Pt solution (0.02 g Pt/1 ml solution) was added to sol proposed by Yoldas [61]. The high specific surface area (400-450 m²/g) of catalyst with the 2-8 nm Pt particles was achieved. Catalyst was deposited by closed-channel, open channel and surface selective infiltration. The layer thickness was limited to ~3 μm, because the thicker coat exhibited cracks and layer delamination from the channel corner for thickness in the range of 6-8 μm. The open-channel coating was faster and achieved a more uniform layer than the closed channel method. However, the amount of catalyst during injection could not be controlled precisely. For this reason, a surface-selective infiltration was arranged. The top of the silicon surface was covered with a hydrophobic layer, when the channels were hydrophilic. Therefore the catalyst deposition by infiltration could be better controlled without spillover and surface contamination [53].

Germani et al. [22] prepared the Pt/CeO₂/Al₂O₃ catalyst using the sol-gel method and coated on the stainless steel microchannel plate using the tape-casting technique. The catalyst coatings showed a high BET-surface area of 330 m²/g and good adherence. The Pt/CeO₂/Al₂O₃-catalyst deposition using the sol-gel slurry allowed a better platinum utilization [22]. Stable and porous thin coatings made of alumina, silica and titania prepared by using the sol-gel technique was achieved by Haas-Santo et al. [43]. Alumina coating was obtained when the acetylacetone stabilizer was added. The silica coating was produced by a two-step synthesis and no stabilizer was needed. The alumina

and silica films, whose slurries contained ethanol as solvent and aluminium-sec-butyrate and tetraethyl-ortho-silane as precursors, showed the best oxide layer qualities such as a high surface-enhancement factor of 858 m²/m² and crack-free and adhesive film [43]. Goerke et al. [55] was based on the same preparation of alumina and silica as via the sol-coating method, which was described by Haas-Santo et al. [43]. However no mass loss was observed before or after the reaction experiments; cracks clearly appeared on both coat surfaces coated on the microchannel stainless steel plates and a lower surface-enhancement ratio of 526 m²/m² was determined for the Ru/Al₂O₃-catalyst [55]. Silica-supported Co and Ni catalysts were synthesised using the sol-gel method and deposited on the channel silicon by Shetty et al. using the dip-coating technique [56]. Co/SiO₂ showed a non-uniform layer and a lower specific surface area of 337.7 m²/g comparing Ni/SiO₂ (452.35 m²/g). However, the lower activity was detected for both catalysts after 10 h of reaction [56]. Giornelli et al [57] discovered that the BET-surface area of titania powder increased from 17.5 to 61.5 m²/g after 1.5 wt.% of PEG addition into the sol-gel solution. They also found that the diameter of macropores increased, but the number of pores decreased. In order to increase the thickness of film, the foil immersion needs to be repeated 10 times due to the very dilute slurry by ethanol (Ti(OBu)₄:C₂H₅(OH):H₂O:NH(C₂H₄OH)₂ = 1:25.5:1:1) [45].

Chen et al. [30] prepared Cu-Zn-Al catalyst support for a Pd-Zn catalyst via the sol-gel method with ethanol and aqueous Cu-Zn-Al-nitrates. HNO₃ was added to keep the pH at 3-4. After the sol coating with a brush, the layer was dried at room temperature for 1 h, then at 60 °C for 6 h and 500 °C for 2 h (20 mg/chip). The uniformity of the catalyst layer was controlled by Hwong et al. [63].

Table 4 Sol-gel method used for catalyst coating onto microchannel foils

Substrate material, channel dimensions [μm]	Catalyst	Additives	T_{calc} [$^{\circ}\text{C}$]; t [h]	BET $\left[\frac{\text{m}^2}{\text{g}}\right]$	Layer thickness [μm]	Layer quality	Adhesion (loss after adhesion tests) [wt.%]	Ref.
100 x 500 500 x 500 150 x 75 Stainless steel 400 x 600	Pt/Al ₂ O ₃	AIP, H ₂ O, HNO ₃ , H ₂ PtCl ₆ ·6H ₂ O+1,3 butanediol	500; 2	400 - 450	< 3	> 3 cracks and deterioration	Good adhesion	53
Stainless steel 400 x 600	Pt/CeO ₂ / Al ₂ O ₃	Al(OC ₄ H ₉) ₃ , water, HNO ₃ , H ₂ PtCl ₆ ·6H ₂ O, Ce(N O ₃) ₃ ·6H ₂ O in H ₂ O	500; 2	330	1.1 - 12.3	Very porous, little shrinkage during drying	-	22
FeCrAl alloy foils	γ -Al ₂ O ₃	I dep.) γ -AlOOH II dep.) γ -Al ₂ O ₃ + γ -AlOOH	I)500,8 00; 3 II)500, 900;2	-	-	Homogenous surface with crystal blocks, cracks	10.84 - 2.79 (ultra-sounds), 21 - 0.02 (thermal shocks)	40
300 x 240		boehmite, γ -Al ₂ O ₃ , HNO ₃ , PVA	500; 3	230	75 mg	Homogenous layer	-	29
DIN 1.4571 400 x 600	Comm. catalyst C18-7	boehmite, HNO ₃ , PVA, catalyst (C18-7)	300; 10	128	-	-	-	29
Fe-based alloy	1)Al ₂ O ₃ , 2)Al ₂ O ₃ -TiO ₂ , 3)Al ₂ O ₃ -SiO ₂ , 4)SiO ₂ , 5)TiO ₂	AISB (1,2,3), AIPP (1), butyl glycol (1,2,3,5) ethanol (1,4), TTIP (2,5), TEOS(3) HNO ₃ + acetylaceton (1,2,3,4,5) [54]	500; 5	1) 152-879*, 2) 100*, 3) 193*, 4) 255*, 5) 74*	2 - 3	Continuous, free of peeling flakes, no uncovered areas	Very good	54
Stainless steel 600 x 150	1)Al ₂ O ₃ 2)SiO ₂		500; 3	526* 470*	0.5 - 2	1) Cracks 2) Small cracks	No mass loss	55
Silicon-based foils 50 x 100	1)Ni/Si O ₂ 2)Co/Si O ₂	TEOS, H ₂ O, HNO ₃ , ethanol+Ni- or Si-nitrates in H ₂ O	450; 4	1) 452.35 2) 337.72	-	Non-uniform Co/SiO ₂ -layer	No deactivation after 8 h above reaction	56
500 x 170	Cu-Zn-Al (Pd-Zn/ Cu-Zn-Al)	Cu(NO ₃) ₂ ·6H ₂ O Zn(NO ₃) ₂ ·6H ₂ O Al(NO ₃) ₃ ·6H ₂ O ethanol	500; 2	79.5	20 mg	Homogenous, dense	0.02 wt.% after 1min vibrations	30
Stainless steel 1 x 0.5 mm	ZrO ₂ (ICI33-5/ZrO ₂)	Zirconium alkoxide, HNO ₃ , ZrO ₂ -powder, IPA, comm. Copper-catalyst (ICI33-5)	400; 2	66	25-27 mg	No coat separation after next coating,	No significant weight loss	58, 59
Capillary reactor, d = 500	CuO/ZnO/Al ₂ O ₃ (BASF13456)	Boehmite, comm. cat. (BASF), H ₂ O, HNO ₃	230; -		>75	Non-uniform, cracks	-	48
Silicon wafer 600x240	CuO/ZnO/Al ₂ O ₃ (SüdChemie)	Aluminium isopropoxide				Non-uniform,		52
Stainless steel 300x200	Al ₂ O ₃ /ZrO ₂ CuO/ZnO/Al ₂ O ₃ (SüdChemie)	Aluminium secondary butoxide, zirconium(IV) propoxide, ethanol, acetylacetone, HNO ₃ , commercial catalyst	300; 2	-	45 mg	Uniform	25wt.%(Al) 40wt.%(Zr); 15wt.%(Al+Zr); 6 days under react. conditions	31
a)Stainless steel structure, b) Silicon wafer, c) FeCrAlloy fibers	γ -Al ₂ O ₃	1) γ -alumina (Puralox SBa-200) 2) boehmite, nitric acide	1a) 500, 2 b) 600	1a) 199, 2 b) 195, 2 c) 8.3	1a) 100 (dipping), 2 b) <1 (dipping), 2 c) - dipping, spraying	1a) Uniform non-precalc. layer, 2 b) Well coverage, no cracks, 2 c) Non-uniform, lack of coat, uniform layer, cracks	1a) Best adherence (T _{calc.} : 550°C) 2 c) Poor adherence, no mass loss (ultrasonic.)	62

*) surface enhancement (m^2/m^2)

The viscosity was adjusted by changing the ratio of catalyst to solvent. In this case, aluminium isopropoxide was hydrolysed in DI-water, and then stirred 1 h at 80 °C. Secondly, HCl and PVA were added. HCl was used to peptize the alumina sol to adjust the pH (3.5-3.7). The catalyst slurry prepared by Conant et al. [64] was made with boehmite, DI-water, nitric acid and zirconia grinding media. After that the commercial CuO/ZnO/Al₂O₃ was added and the mixture was milled overnight.

2.7.4 ANODIC OXIDATION

An adherent and homogeneous aluminium oxide layer was achieved by Wunsch et al. [54] using anodic oxidation of microstructured AlMg foils. The oxalic acid electrolyte was pumped through the channels under a constant voltage of 50 V and a temperature of 12 °C. The cathodes were situated on both sides of the channels with a distance of 10 mm. The coating's thickness was influenced by the channel length, width and depth. The film thickness decreased with the higher channel length. At a 15 mm length and 200 µm width, the microchannel generated a 7 µm thick layer after 6 h. A 3 µm thick layer was formed at a channel width of 40 mm. However, the layer growth was more rapid for the open surface coating. The growth rate of 4 µm/h appeared only for the first 4 h; the rate dropped after that (Tab. 5).

2.7.5 ELECTROPHORETIC DEPOSITION (EPD)

Wunsch et al. [54] used the electrophoretic deposition of Al₂O₃-nanoparticles from colloidal solution in microchannels. The same experimental conditions were chosen for the coating. The plates were etched for 45 minutes using 96-98 % H₂SO₄. The property of the layer in the channel was influenced by the composition of the three suspensions. Deposition of Al₂O₃ nanoparticles dispersed in water and glycerol was

found to be the most effective. The oxide layer was well-adhered and relatively homogeneously distributed compared to two other suspensions prepared as oxalic acid solution of Al₂O₃ nanoparticles in water. These layers were non-uniform and insufficiently adhered in the channel (Tab. 5).

2.7.6 FLAME SPRAY DEPOSITION

Thybo et al. [67] presented a flame spray deposition as a very flexible method for catalyst distribution directly on the foil. An organic solution of metal precursor solution consisting of gold-triphenylphosphin-nitrate, Ti-tetraisopropoxide, tetrahydrofuran and isooctane was fed with the spray gas into a spray nozzle. The aerosol with droplets of 10 µm diameter were produced and combusted in the flame. The organo-metallic compounds were decomposed at 1500 K and nanometre-particles were formed. The spray was surrounded by a hydrogen burner. The sample holder was water – cooled to enlarge the thermophoresis and to deposit the particles on the surface. The deposition rate was influenced by the different positions of the sample holder. When the sample high was decreased from 15 to 5 cm, the deposition rate increased by 60 %. The strong dependence of the deposition was the radial distance of the sample to the flame zone. In this experimental work the sample high of 6 cm and a radial position of 0.5 cm was used for deposition. Good adhesion was obtained on the Si, Ti and the H:Si silicon surfaces, where the Au/TiO₂ catalyst coat was difficult to scribe off (Tab. 5).

2.7.7 ELECTROLESS PLATING

The electroless plating of the copper-based catalyst on the inside wall of an aluminium tube was prepared by Fukuhara et al. [66]. The zinc oxide, iron and copper plating solutions were poured into the tube using a suction pump. The tube was then washed with water and dried at 80 °C for 24 h. The undulating porous layer that formed all over the inner surface of the aluminium

tube was 100 μm thick and in tight contact with the surface. The initial catalyst activity was maintained for five days and under a reaction temperature of 150 $^{\circ}\text{C}$. After this time the deterioration in activity was caused by sintering of the copper particles (Tab. 5).

2.7.8 CHEMICAL VAPOR DEPOSITION (CVD)

Janicke et al. [65] investigated the channel coating of stainless steel microreactors with alumina by chemical vapour deposition (CVD). The aluminium isopropoxide was used as the alumina precursor. The gases such as N_2 with a flow rate of 1L/min and then O_2 with 7L/min to decompose of the alkoxide were passed through the molten precursor, which was kept at 160 $^{\circ}\text{C}$ in a glass bubbler. After 1 h of heating at 300 $^{\circ}\text{C}$ and passing N_2 (7 L/min) through microchannels, the reactor was cooled. SEM micrographs showed the well-coated Al_2O_3 layer. The channel surfaces were completely and evenly coated across the entire channel length. A 10 μm layer thickness was formed (Tab. 5).

2.7.9 SPUTTERING VS UV-DECOMPOSITION

Yeong et al. [68] showed different methods of catalyst preparation such as sputtering and UV-decomposition of palladium acetate. These methods did not require the pre-coating of the foil with support material. A 100 μm thick layer formed due to sputtering process, which was operated under vacuum conditions. The substrate was used as the anode and the palladium as the cathode. The coated material (palladium) emitted atoms to the substrate. The active sites were densely packed and the palladium layer was continuously distributed.

In the UV-decomposition method, the channels were coated with a palladium acetate solution and were irradiated for 30 min. using a UV lamp. For this reason, the organic compounds were decomposed leaving only

palladium on the channel surface. After reaction the carbon was detected. This catalyst coated UV-decomposition technique was active for a longer time compared to the catalyst distribution using sputtering, because of higher palladium amounts and a varied catalyst structure caused by the different catalyst preparation method. The catalyst surface was uneven, cracked and rough due to the void regions with palladium crystallites (Tab. 5).

2.7.10 MOLTEN SALT SYNTHESIS

Rebrov et al. [69] obtained highly active and stable catalyst coatings for the water-gas shift reaction in fuel processors. The catalyst layers were synthesized by molten salt synthesis after immersing the molybdenum substrate in a 5 wt.% Li_2CO_3 , NaCl-KCl equimolar mixture and treatment at 1123 K for 7 h with the cathodic current density of 5 mA cm^{-2} . The coatings were stable 500 h under steam at 631 K in a gas mixture containing 0.5 vol.% CO , 1.5 vol.% H_2O and 40 vol.% H_2 . The catalytic activity increases were detected when molybdenum carbide was presented as a catalyst layer on the substrate surface compared to only the Mo_2C phase (Tab. 5).

2.7.11 ZEOLITE CATALYSIS

Rebrov et al. [70] also investigated zeolite coatings of ZSM-5 on AISI 316 stainless steel microchannel plates. The catalyst mixture based on the catalytic reaction of NO with ammonia due to ion exchange with cerium at 97 $^{\circ}\text{C}$ for 24 h. The ratio of cerium ions, which appeared from cerium acetate solution to Al ions, was 10. The influence of the Si/TPAOH ratio, reaction temperature and synthesis time were analysed. It was found that the ratios of $\text{H}_2\text{O}/\text{Si} = 130$ and $\text{Si}/\text{template} = 13$ and synthesis conditions such as a temperature of 130 $^{\circ}\text{C}$ and time of 35 h were optimal for the formation of a homogenous zeolitic layer. The zeolite coating was

more strongly bonded with the metal surface than the zeolite crystal itself, leading to some cracks appearing

in the layer after its exposition in 10 thermal cycles between temperatures of 20 and 400 °C (Tab. 5).

Table 5 Other methods used for catalyst coating onto microchannel foils

<i>Deposition method, Coated material (catalyst)</i>	<i>Substrate material, channel dimensions</i>	<i>Additives (polymer, etc)</i>	<i>T_{calc} [°C]; t [h]</i>	<i>BET $\left[\frac{m^2}{g} \right]$</i>	<i>Layer thickness [μm]</i>	<i>Layer quality</i>	<i>Adhesion (loss after adhesion tests)</i>	<i>Ref</i>
Anodic oxidation of sol-gel (γ-Al₂O₃)	AlMgAlloy, 0.05 x 0.05 x 1.5 mm,	Oxalic acid (electrolyte)	500; 6	-	4	Uniform, homogenous	Adherent layer	54
	0.1 x 0.1 mm,				7			
	0.2 x 0.2 mm				10			
	0.2 x 0.2 x 10 mm				2			
0.2 x 0.2 x 50 mm								
Electrophoretic deposition (γ-Al₂O₃)	1.4335 stainless steel	Al ₂ O ₃ + H ₂ O+ 1. - 2. Al(OH) ₃ 3. glycerol	400; 8	2. 62*	1. -	1. Non-uniform 2. Homogenous and cracks 3. Homogenous	1. Insufficient adhesion 2. Good adhesion 3. Well adhered layer	54
	0.4 x 0.4 mm				2. 2-4 3. 3			
Flame spraying (Au/TiO₂)	Silicon	Gold-triphenylphosphinite, Ti-tetraisopropoxide, tetrahydrofurane, isooctane	1227	350	50-150	Thick layer-cracks (5μm,5mm), thin layer-more uniform	Good adhesion	67
Electroless plating (Cu-Fe/Zn)	Aluminium tube D = 1 mm	Plating solutions: ZnO, FeSO ₄ x 7H ₂ O, Cu(NO ₃) ₂ x 3H ₂ O	80; 24 and 300;1 in steam	33	100	Undulating porous deposits	5 days	66
CVD (Pt/Al₂O₃)	stainless steel 0.14 x 0.2mm	Aluminium isopropoxide (Al(O-i-Pr) ₃)	550	-	10	Uniform coat	-	65
Sputtering (Pd) UV-decomposition (Pd)	stainless steel 0.3 x 0.1 mm	Palladium	450; 4	-	0.1	Cracked, flaky surface	43 h (activity decrease)	68
	stainless steel 0.3 x 0.1mm	Palladium acetate	-; 0.5	-	-	Rough, uneven, cracked surface	Loss of palladium, 33 h (activity decrease)	68
Molten salt synthesis (Mo₂C/Mo) Zeolitic coating (ZSM-5)	Mo-plates 0.13 x 0.4 mm	NaCl-KCl	850; 7	18	4	Porous structure	23h (activity decrease)	69
	AlSi 316 stainless steel 1x1cm	TEOS**, TPAOH***, NaAlO ₂ , H ₂ O	450; 10	435	-1-24 -28-150 -40	- Uncovered areas - Discontinuity of layer - Uniform	Some cracks after 10 thermal cycles	70

*) surface enhancement (m²/m²); **)tetraethylorthosilicate; ***)Tetrapropylammonium hydroxide

2.7.12 **IMPREGNATION** **METHOD**

The impregnation method is used for the distribution of catalyst in the form of aqueous metal salts, which are distributed on the different supports. This method was largely used for catalyst deposition on the wash coated on to microchannel foils of the alumina layer [3, 24, 25, 71].

Pfeifer et al. [47] tested and compared two different impregnation techniques: post-and pre impregnations. For post-impregnation, the ZnO-layer dried at room temperature was impregnated drop-wise with a solution of palladium acetate in toluene. After drying, the foil was calcinated at 450 °C for 5 h. The impregnation included the addition of palladium acetate solution in toluene to ZnO particles before their dispersion. First, the particles were dried and pre-calcinated at 250 °C for 1 h for acetate decomposition. Then the second calcination occurred after the washcoating process and drying step. The catalyst characterisations showed no significant differences between the two layers. They decided to use the pre-impregnation method for further catalyst preparation, due to separate decomposition of acetate during first calcination at temperatures below the sintering of the zinc oxide. However, the investigations concerning the activity test of both catalysts proved that the post-impregnated catalyst was more active and showed higher stability compared to the catalyst prepared by the pre-impregnation method.

Yeong et al. [68] showed the different methods of the catalyst preparation (palladium) on the γ -alumina layer such as wet impregnation and incipient wetness. For the wet impregnation, the 10ml of palladium nitrate solution covered the channels for 2h. After that the surplus solution was removed and the channels were dried in air for 2 h. The coated foil was then pre-calcinated at 120 °C for 30 min and calcined at 400 °C for 3 h. The one difference of the incipient wetness method was that the channels covered with the same solution were then left to dry in a fume cabinet. The plate was then calcined. The catalyst prepared by the first method achieved the complete conversion for 6 h.

Each reactivation step influenced the structural changes of catalyst and led to decreased activity. The catalyst achieved after the incipient wetness impregnation retained the stable activity after 28 h. The catalyst characteristics showed the carbon spaces on the surfaces after reaction and catalyst loss during experiments, but there was still sufficient palladium to sustain stable activity.

The incipient wetness method was chosen by Hu et al [32] to prepare the Sabatier and RWGS catalysts. For the Sabatier catalyst preparation, the solutions containing Ru-or Rh nitrates were impregnated on different supports such as TiO₂, Al₂O₃ and SiO₂. After that the samples were dried at 110 °C overnight and calcined than at 450 °C for 3 h.

Hu et al. [32] investigated the two different ways of Ru- and Rh catalyst deposition by the incipient wetness technique. The impregnated powders were wash coated onto FeCrAlY-alloy substrates. The Sabatier and the RWGS catalysts were distributed on the porous FeCrAlY felt and FeCrAlY foam respectively. Solutions containing Ru- and Rh nitrates were impregnated on different supports such as TiO₂ and ZrO₂. After that the samples were dried at 110 °C overnight and then calcined at 450 °C for 3 h. The RWGS catalyst (Ru/ZrO₂-CeO) was prepared first by the distribution of Ce(NO₃)₂ onto ZrO₂ support, then calcined at 350 °C for 3 h. Secondly, the Ru nitrate solution was impregnated onto ZrO₂-CeO₂. Then calcination was carried out at 500 °C for 3 h. Both catalysts showed highly stability after several start-up and shut-down cycles. The RWGS catalyst obtained the reaction conversion near equilibrium at high temperature operability. However it was sensitive to the reaction temperature changes. For the Sabatier catalyst the parameters such as metal loading, BET surface area and catalyst support significantly influenced the reaction. Moreover, this catalyst showed more significant performance affected by the GHSV compared to the RWGS catalyst.

2.8 CATALYST DEPOSITION

METHODS

2.8.1 DIP-COATING (SPRAY COATING)

In general, the suspension and the sol-gel are applied to the structured object by dip-coating [72]. An alternative to dip-coating is spray-coating. Instead of immersing the structure in slurry, a spray of the suspended powder is applied [73]. The properties of the suspension differ from that used for dip-coating, namely viscosity since the shear rate is many times larger during spraying than immersing. As an example, Sidwell et al. [74] prepared a suspension (hybrid) containing a commercial catalyst (Pd/Al₂O₃), an aluminium oxide (Catapal D) and acetone (acetone/powder ratio = 4/3) [74]. Several layers are applied by spraying until the desired thickness is obtained. Acetone is removed by nitrogen flowing between each sprayed layer. Calcination is carried out at the end of the coating. In that example, the spray is applied to a cast-alumina disk. Spraying is well-adapted to the coating of fibres [62]. Wu et al. [33] used both spray-coating (plasma spraying) and dip-coating methods to apply suspensions on FeCrAl mesh. The same thickness was obtained with both methods but starting from different suspensions: suspended alumina with polyvinyl alcohol and water for plasma-spray coating, suspended alumina in a boehmite sol (hybrid method) for dip-coating. The spray-coated layer was found to be more adhesive. A wash-coating method was developed to deposit the needed γ -Al₂O₃ layer in the microchannels [68, 72] or the monoliths by dipping into the suspension (washcoating), then dried and calcined at 800 °C for 4 h. The same method was used in the second step of the monolith coating during the Ni-nitrate impregnation [50]. In the work of Pérez-Cadenas et al. [51] several alumina coatings were applied on the monolith walls of microchannels by dip-coating with drying under rotation at room temperature and high temperature calcination (2 K/min). The dip-coating

method was used by Kundu et al. [31] for sol coating on the microchannels. A uniform catalyst layer was obtained with the thickness of 25 μ m.

2.8.2 DROP-COATING

In the case of coating deposited before microreactor assembling, drops of the sol-gel can be deposited (drop-coating) with a possible simultaneous heating of the microreactor channels [56, 75].

2.8.3 SPIN-COATING

Spin-coating can also be used for wafers (microstructured or not) [72]. According to this deposition method, a correlation between the film thickness, the sol viscosity and the spin speed was proposed by Huang and Chou [76].

2.8.4 BRUSH, SYRINGE

A less predictable method such as the use of a brush to deposit the liquid as a thin layer is also possible [81]. The sol of Cu-Zn-Al was coated by Chen et al. [30] onto the microchannel plate using a soft fine brush. Stefanescu et al. [80] applied the slurry to the microstructures by using a syringe. It was a way to undertake the catalyst deposition procedure at lab scale with good layer quality. The capillaries inside the microreactor were first filled with the catalyst slurry also using a syringe; the fluid was then forced using air flow [60].

2.8.5 INFILTRATION, GAS FLUID

In undertake a closed microchannel (assembled microreactor or capillaries), the deposition can be

performed by infiltration of the sol-gel [53] or gas fluid displacement, which consists of filling the capillary with a viscous fluid, and clearing the capillary by forcing gas through it [50, 77]. In contrast, in the example detailed by Janicke et al. [65], the excess fluid was not removed. Microchannels were filled with an aluminium hydroxide solution (pH 5.8, 1.70 % Al_2O_3), which was allowed to slowly dry over a 24 h period, and then calcined at 550 °C. Hwong et al. [52] showed the alumina sol coating on the inside of the microchannels by using one of the two methods of flow and fill-and-dry coating. Those two methods proved non-uniformity of the catalyst thickness in comparison to the DI-water-based catalyst slurries, which were affected by those coatings thanks to the lower viscosity.

2.8.6 ELECTROSTATIC SOL- SPRAY DEPOSITION

Electrostatic sol-spray deposition has been used on aluminium surfaces to spray zinc acetate or zirconium propoxide sols [78] or on stainless steel to spray a titanium tetrahydropropoxide sol [79]. By combining the generation of a charged aerosol and the heating of the substrate to coat (100–200 °C), an easy control of the morphology of the deposited layer was obtained.

3 EXPERIMENTAL DETAILS

3.1 CATALYST CHARACTERIZATION METHODS

3.1.1 BET SURFACE AREA MEASUREMENT (S_{BET})

BET surface areas were determined for each catalyst using an *Autosorb-1 (Quanta chrome)*.

The Brunauer, Emmett, and Teller (BET) theory enables the determination of the number of molecules required to build a monolayer of the adsorbate on the adsorbent surface. Before the process of physical adsorption, the surface cleaning takes place through a heating of the sample at a constant temperature of 77 K. Degassing is needed to remove the impurities such as oils and water from the solid surface. The adsorption begins at low relative pressure and during this time the higher energetic sites are covered first by the gas molecules. Those high energy sites lie in the narrow pores where their walls possess overlapping potentials. The other ones could be found between horizontal and vertical edges of the analysed surface sections where the interactions of the adsorbate with the surface molecules take place on two areas. The high energy spots are found wherever the planes provide overlapping potentials. In addition, the nature of the atoms of functional groups of the surface will influence the energy level on the surface, which consists of heteroatoms.

The complete surface coverage including second and higher adsorbed layers occurs during the adsorbate pressure increase and gas molecules are adsorbed on previous bond molecules forming the first monolayer.

The uppermost molecules are in dynamic equilibrium with the vapour (Fig. 5).

The equilibrium in the first layer describes the Langmuir theory with the equation 4

$$N_m \cdot \theta_1 \cdot \nu_1 \cdot e^{-E_1/RT} = k \cdot P \cdot \theta_0 \cdot A_1 \quad \text{Equation 4}$$

where N_m is the number of adsorbate molecules in a completed monolayer of one square centimetre, θ_1 is the fraction of the surface occupied by the adsorbed molecules, E is the energy of adsorption and ν_1 is the vibrational frequency of the adsorbate normal to the surface when adsorbed. The product $N_m \theta_1$ is the number of molecules adsorbed per square centimetre. The term $e^{-(E/RT)}$ represents the probability that an adsorbed molecule possesses adequate energy to overcome the net attractive potential of the surface.

For the fraction of surface coated by nth layer, equation 5 can be expressed as:

$$N_m \cdot \theta_n \cdot \nu_n \cdot e^{-E_n/RT} = k \cdot P \cdot \theta_{n-1} \cdot A_n \quad \text{Equation 5}$$

The terms ν , E , and A remain constant for the second and higher layers, which are all equivalent to the liquid state. Using L as the heat of liquefaction

$$\frac{\theta_1}{\theta_0} = \frac{kPA_1}{N_m \nu_1 e^{-E/RT}} = \alpha \quad \text{Equation 6}$$

$$\frac{\theta_n}{\theta_{n-1}} = \frac{kPA}{N_m \nu e^{-L/RT}} = \beta \quad \text{Equation 7}$$

then

$$\theta_1 = \alpha \theta_0 \quad \text{Equation 8}$$

$$\theta_n = \beta \theta_{n-1} = \alpha \beta^{n-1} \theta_0 \quad \text{Equation 9}$$

The number of molecules adsorbed at equilibrium is

$$N = N_m (\theta_1 + 2\theta_2 + \dots + n\theta_n) \quad \text{Equation 10}$$

Substituting θ from equations 8 and 9 yields

$$\frac{N}{N_m} = \alpha\theta_0(1 + 2\beta + 3\beta^2 + \dots + n\beta^{n-1}) \quad \text{Equation 11}$$

where both α and β are constants.

Replacing the ratio α/β in equation 11 with C gives

$$\frac{N}{N_m} = \frac{C\theta_0\beta}{(1-\beta)^2} \quad \text{Equation 12}$$

Essentially

$$1 = \theta_0 + \theta_1 + \theta_2 + \dots + \theta_n \quad \text{Equation 13}$$

then

$$\theta_0 = 1 - \sum_{n=1}^{\infty} \theta_n \quad \text{Equation 14}$$

From equation 12 after substitution of θ_0 we have

$$\frac{N}{N_m} = \frac{C\beta}{(1-\beta)^2} \left(1 - \sum_{n=1}^{\infty} \theta_n\right) \quad \text{Equation 15}$$

Introducing θ_n from equation 14 with equation 9 and replacing $C\beta$ in place of a α , and the summation of β^n as $\beta/(1-\beta)$, gives

$$\frac{N}{N_m} = \frac{C\beta}{(1-\beta)^2} \left(1 - C\theta_0 \frac{1}{1-\beta}\right) \quad \text{Equation 16}$$

Replacing θ_0 from equation 16 to equation 12 we have

$$\frac{N}{N_m} = \frac{C\beta}{(1-\beta)(1-\beta+C\beta)} \quad \text{Equation 17}$$

Replacing the $N/N_m = W/W_m$ and $\beta=P/P_0$ gives the BET equation in final form

$$\frac{1}{W[(P_0/P)-1]} = \frac{1}{W_m \cdot C} + \frac{C-1}{W_m \cdot C} \cdot \left(\frac{P}{P_0}\right) \quad \text{Equation 18}$$

where W is the weight of gas adsorbed on a unit weight of adsorbent, W_m is the weight adsorbed in a monolayer, P is the adsorbate pressure, P_0 is saturated vapour pressure, C is the BET constant.

Figure 4 presents a plot of $1/W[(P_0/P)-1]$ versus P/P_0 with a straight line in the range $0.05 \leq P/P_0 \leq 0.35$.

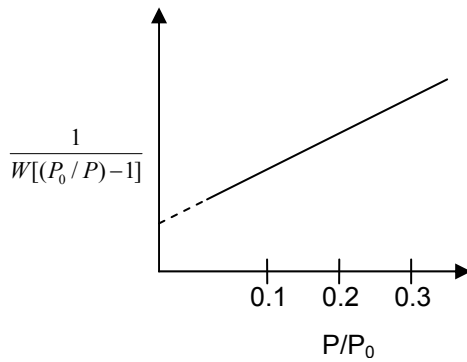


Figure 4 Typical BET plot.

The weight adsorbed in a monolayer W_m presenting the following equation

$$W_m = \frac{1}{s+i} \quad \text{Equation 19}$$

where s is the slope, i is the intercept of a BET plot

$$s = \frac{C-1}{W_m \cdot C} \quad \text{Equation 20}$$

$$i = \frac{1}{W_m \cdot C} \quad \text{Equation 21}$$

and

$$C = \frac{s}{i} + 1 \quad \text{Equation 22}$$

The total surface area can be determined by dividing S_t by the sample

$$S_t = N_m \cdot A = \frac{W_m \cdot \bar{N} \cdot A}{M} \quad \text{Equation 23}$$

where A and M are the cross-sectional area and the molecular weight of the adsorbate, and N is Avogadro's number [82].

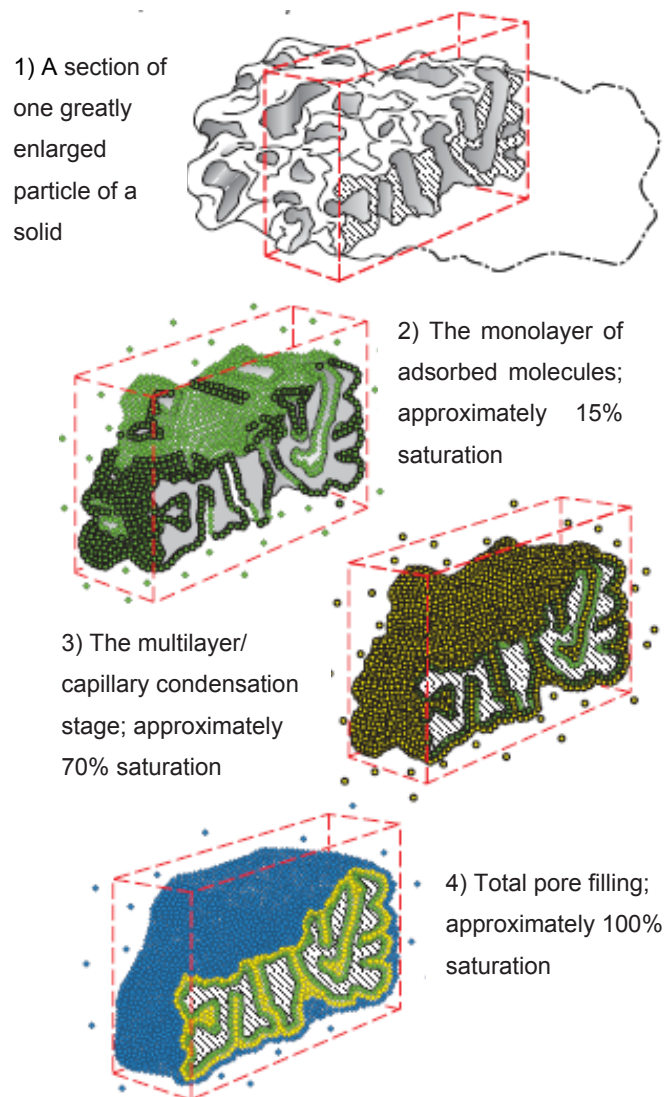


Figure 5 The covering of the adsorbent solid surface with gas molecules in the form of a thin layer [83].

3.1.2 MERCURY POROSIMETRY

Many solid and powder materials contain a certain internal volume of empty space. Porosity strongly determines important physical properties of materials, such as durability, mechanical strength, permeability, adsorption properties, etc. The knowledge of pore structure is an important step in characterizing materials in order to predict their behaviour under different environmental conditions. There are two main and important typologies of pores: closed pores and open pores. Closed pores are completely isolated from neither the liquid nor gaseous phase. They influence parameters like density, along with mechanical and thermal properties. Open pores are connected to the external surface and are, therefore, accessible to fluids, depending on the nature and size of the pore and the nature of the fluid. Open pores can be further divided into dead-end or interconnected pores. Further classification in relation to the pore shape should be determined whenever possible (Tab. 6).

Classification of pores according to their width:

- Micropores: less than 2 nm
- Mesopores: between 2 nm and 50 nm
- Macropores: larger than 50 nm

The principle of the technique is based on the fact that mercury behaves as non-wetting liquid toward most substances. This technique is not advisable when the sample contains metals reacting with mercury (e.g. gold) and forming amalgam. Mercury is forced to enter into the pores by applying a controlled increasing pressure. As the sample holder is filled with mercury under vacuum conditions, mercury surrounds the sample without entering the pores due to the very low residual pressure. During the experiment, the pressure is increased, and the volume of mercury penetrated is detected by means of a capacitive system.

The decreasing volume of mercury in the sample holder represents the pore volume while the

penetration pressure is inversely proportional to the pore size. The method is based on the capillary depressurization phenomenon. In a porous body, the surface tension forces are opposed to the penetration by liquids showing a contact angle higher than 90° (non-wetting liquids). It is necessary to apply a pressure to mercury compensating the pressure difference over the mercury meniscus in the porous body:

$$P = -\Delta P_C = \gamma \left(\frac{1}{r_m} + \frac{1}{r_m} \right) \quad \text{Equation 24}$$

where ΔP_c is the capillary pressure, γ is the surface tension of mercury, and r_m are the principal meniscus curvature radii. These last values are in principle unknown in real porous media; therefore, it is generally considered the curvature of meniscus C: $P = \gamma C$. For mercury, a surface tension of 480 dyne/cm is generally quoted. The curvature C depends on the contact angle between mercury and the solid and on the pore geometry. For cylindrical capillaries:

$$C = \frac{2 \cos \theta}{r} \quad \text{Equation 25}$$

where θ is the contact angle, and r is the capillary radius, the combinations of the two previous equations leads to the well-known Washburn equation:

$$P = \frac{-2\gamma \cos \theta}{r} \quad \text{Equation 26}$$

Although in almost any porous media there are no cylindrical pores, the Washburn equation is universally used to calculate pore size distribution from mercury porosimetry data. The most frequent contact angles of mercury are between 130° and 150°, even though larger values have been reported. If θ is unknown, an average value of 140° is generally used.

Table 6 Classification of porosimeter according to pore sizes

INSTRUMENT	PRESSURE RANGE [MPa]	PORE SIZE r [nm]	PARTICLE SIZE d [μ]
Pascal 140	0.013-0.4	58,000-1,900	330-15
Pascal 140 + ultramacropore	0.0013-0.4	300,000-1,900	3,000-15
Pascal 240	0.1-200	7,500-3,7	40-0.015
Pascal 440	0.1-400	7,500-1,8	40-0.01

- **Specific Pore Volume and Porosity**

Internal void space in a porous material generally expressed as a void volume (in cc or ml) refers to the mass unit (g). The porosity is the ratio of the total pore volume to the apparent volume of the solid or powder (excluding inter particle voids).

The solid mass consists of pores, cavities, and cracks of various shapes and sizes. The total sum of these void volumes is called porosity.

- **Pore Size Distribution**

Pore size distribution is generally represented as the relative abundance of the pore volume (as a percentage or a derivative) as a function of the pore size.

The pore volume V is changed with the variations of a cylindrical pore radius from r to $r - dr$, given by

$$dV = -2n\pi r l dr \quad \text{Equation 27}$$

where n is the number of pores with radius r and length l .

Generally, the equation 27 can be rewritten as

$$dV = -D_v(r)dr \quad \text{Equation 28}$$

where $D_v(r)$ is the volume pore size distribution function, which is defined as the pore volume per unit interval of pore radius.

Using the Washburn's differentiation theory, the following equation yields

$$Pdr + rdP = 0 \quad \text{Equation 29}$$

Substituting equation 28 and 29 gives

$$dV = D_v(r) \frac{r}{P} dP \quad \text{Equation 30}$$

Figure 6 shows the curves plotted based on the function from equation 30.

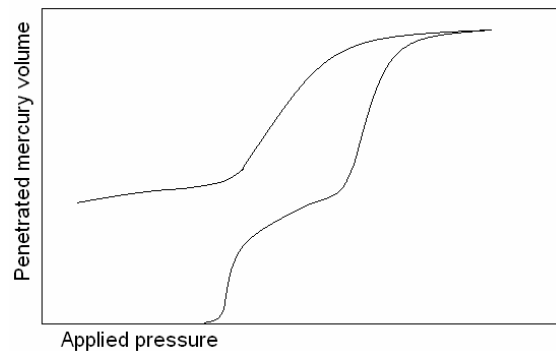


Figure 6 Mercury porosimeter: applied pressure as a function of penetrated mercury volume.

Then

$$D_v(r) = \frac{P}{r} \left(\frac{dV}{dP} \right) \quad \text{Equation 31}$$

The resulting equation (3.5) represents the function $D_v(r)$, whose values are plotted as the distribution curve and gives the pore volume per unit radius interval (Fig. 7) [84, 85, 86].

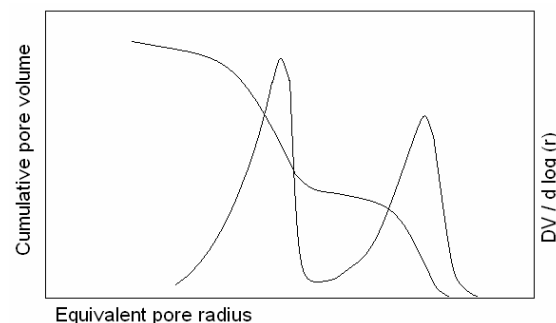


Figure 7 Mercury porosimeter: pore size distribution.

- **Density**
True density.

The true density is defined as the ratio of the mass to the volume of that mass. The mercury porosimetry technique gives the true density of the solid materials excluding their pores and voids smaller than 1.8 nm, which are measured at the highest pressure 414 MPa. This density of the material excludes pores and inter-particle voids.

Apparent density.

Apparent density of the material includes closed and inaccessible pores. Those materials have pores smaller than those corresponding to the highest pressure.

Bulk density (envelope density).

Bulk density of the material includes pores and inter-particle voids. Density is expressed as a mass over the volume.

Effective density

The effective density is given with the measured quantity because some particles have foreign compounds in their bodies which increase or decrease densities. Moreover, they may contain blind pores, which effectively reduce the particle's densities.

- **Specific Surface Area**

The surface area of a solid material is the total surface of the sample that is in contact with the external environment. It is expressed as square metres per gram of dry sample. This parameter is strongly related to the pore size and the pore volume (the larger the pore volume, the larger the surface; the smaller the pore size, the higher the surface). The surface area results from the contribution of the internal surface of the pores plus the external surface of the solid or the particles [82]. The equation of the tensions or forces cancel at the point where mechanical equilibrium was established and it yields

$$\gamma_{SV} = \gamma_{SL} + \gamma_{LV} \cos \theta \quad \text{Equation 32}$$

where γ_{SV} , γ_{SL} , γ_{LV} are the interfacial tensions between solid-vapour, solid-liquid and liquid-vapour; θ is the contact angle.

$$W = (\gamma_{SL} - \gamma_{SV}) \Delta A \quad \text{Equation 33}$$

where ΔA is the area of the capillary wall covered by liquid as it rises. Combining equations 32 and 33 yields

$$W = -(\gamma_{LV} \cos \theta) \Delta A \quad \text{Equation 34}$$

A volume of liquid is forced out of the capillary with gas at a constant, above ambient pressure, that is

$$W = V \Delta P_{gas} \quad \text{Equation 35}$$

Substituting equation 34 and 35 gives

$$\Delta P_{gas} V = (\gamma \cos \theta) \Delta A \quad \text{Equation 36}$$

where ΔP_{gas} is the excess pressure above that of the external pressure and V is the volume of liquid displaced.

The increase in interfacial surface area ΔA is the pore and void surface area S. For pores with the radius range dr and volume dV their area dS is expressed as

$$dS = \frac{PdV}{\gamma |\cos \theta|} \quad \text{Equation 37}$$

The surface area of all pores and voids filled up to radius r and pressure P with pore volume V:

$$S = \frac{1}{\gamma |\cos \theta|} \int_0^V PdV \quad \text{Equation 38}$$

The surface area calculated for different pressure with V [cm³], P [MPa], $\theta = 140^\circ$, $\gamma = 480$ [erg cm⁻²], given by: Contact Angle=141.3°; Hg surface tension=480 dyne/cm; Kp factor=4.65

$$S = 2.72 \int_0^V PdV \text{ [m}^2\text{]} \quad \text{Equation 39}$$

3.1.3 SCANNING ELECTRON MICROSCOPY WITH ENERGY-DISPERSIVE SPECTROMETRY (SEM; EDXS)

Scanning electron microscopy (SEM) analyses of washcoated catalyst surfaces were performed on a JEOL JWS-7515.

Electrons from a field-emission cathode are accelerated by a voltage of 1-50 kV between cathode and anode. The gun cross-over with a diameter of 10-50 μm for thermionic and 10-100 nm for field-emission guns is demagnified by a two-or three-stage electron lens system, so that an electron probe of about 1-1000 nm carries an electron probe current between 1 pA and 100 nA. The final probe-forming lens has to operate with a relatively long working distance (between specimen and lower pole-piece), so that the various particles and quanta emitted can be collected with the desired efficiency. This increases the spherical aberration of the probe-forming lens and, therefore, the smallest attainable electron probe size. A deflection coil system in front of the last lens scans the electron beam in a raster across the specimen in sync with an electron beam of a separate cathode ray tube (CRT). The intensity of the beam in the CRT is modulated by one of the recorded signals to form an image on the CRT.

EDXS measurement was an option of the mentioned electron beam instrument, such as SEM. Its three main parts are the detector, the processing electronics, and the MCA display. The detector generated a charge pulse proportional to the X-ray

energy. This pulse was first converted to a voltage. Then the signal was amplified through a field effect transistor (FET), isolated from other pulses, further amplified, and then identified electronically as resulting from an X-ray of specific energy. Finally, a digitized signal was stored in a channel assigned to the energy in the MCA.

3.1.4 X-RAY DIFFRACTION (XRD)

The crystal structure of the powder catalysts was investigated by powder X-ray diffraction. The results were obtained on a Bruker AXS (Siemens) D5005 θ - θ diffractometer using filtered Cu K α radiation and a graphite secondary-beam monochromator. Diffraction intensities were measured by scanning with steps of 0.05° (2θ) and 5-20 sec/step. X-rays are electromagnetic radiation of wavelength about 1 Å (10⁻¹⁰ m), which is about the same size as an atom. They occur in that portion of the electromagnetic spectrum between gamma-rays and the ultraviolet. The X-rays enabled the analysis of a probe crystalline structure at the atomic level. X-ray diffraction has been in use in two main areas: for the fingerprint characterization of crystalline materials and the determination of their structure. Each crystalline solid has its unique characteristic X-ray powder pattern which may be used as a "fingerprint" for its identification. Once the material has been identified, X-ray crystallography may be used to determine its structure, i.e. how the atoms pack together in the crystalline state and what the interatomic distance and angle are, etc. X-ray diffraction is one of the most important characterization tools used in solid state chemistry and materials science. We can determine the size and the shape of the unit cell for any compound most easily using the diffraction of x-rays.

If an incident X-ray beam encounters a crystal lattice, general scattering occurs.

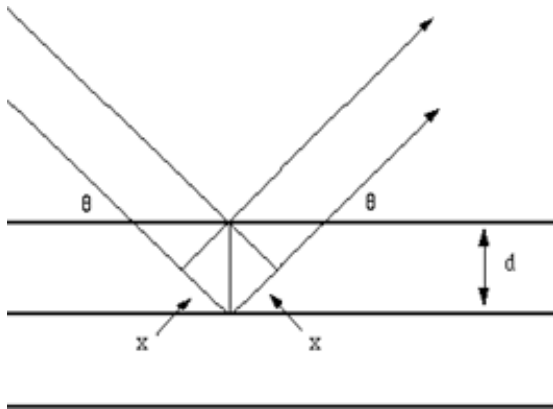


Figure 8 Reflection of X-rays from two planes of atoms in a solid.

The path difference between two waves (fig. 8):

$$2 \times \lambda = 2d \sin(\theta) \quad \text{Equation 40}$$

θ - angles of incidence [°]

d - the distance between atomic layers in a crystal [Å]

n - an integer [-]

λ - wavelength of the incident X-ray beam [Å]

For constructive interference between these waves, the path difference must be an integral number of wavelengths:

$$n \times \lambda = 2x \quad \text{Equation 41}$$

This leads to the Bragg equation:

$$n \times \lambda = 2d \sin(\theta) \quad \text{Equation 42}$$

The X-ray diffraction experiment requires an X-ray source, the sample under investigation and a detector to pick up the diffracted X-rays. Figure 9 is a schematic diagram of a powder X-ray diffractometer.

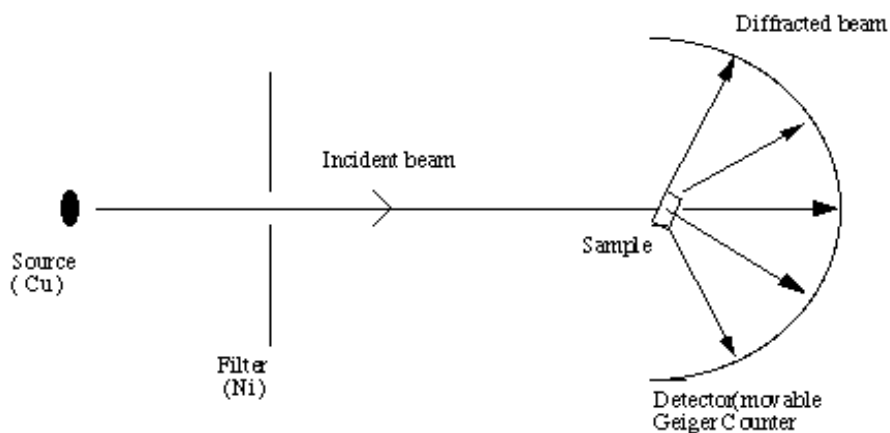


Figure 9 Schematic of an X-ray powder diffractometer.

The X-ray radiation most commonly used is that emitted by copper, whose characteristic wavelength for the K radiation is $\approx 1.5418 \text{ \AA}$. When the incident beam strikes a powder sample, diffraction occurs in every possible orientation of 2θ . The diffracted beam can be detected by using a moveable detector such as a Geiger counter, which is connected to a chart recorder. In normal use, the counter is set to scan over a range of 2θ values at a constant angular velocity. A 2θ

range of 5 to 70 degrees is normally sufficient to cover the most useful part of the powder pattern. The scanning speed of the counter is usually 2θ of $2 \text{ degrees min}^{-1}$ and therefore, about 30 minutes are needed to obtain a trace [87].

3.1.5 THERMO GRAVIMETRIC ANALYSIS (TGA)

The basic principle of thermogravimetry is simple: the sample to be analyzed is placed on a weighing instrument within a furnace or heating device, and subjected to a defined heating program within a furnace or heating device. Time- and temperature-dependent mass changes are monitored continuously. The metrological implementation of this basic principle in a thermobalance, however, is complicated by the need to determine not only sample weight, but the exact temperature in the sample chamber and, in some cases, other parameters as well. As the name implies, it is the balance – its readability and sensitivity – that defines the performance capability of a thermobalance, particularly with respect to initial sample weight and, more importantly, the slightest measurable change in mass.

Advances in simultaneous thermal analysis (STA)

In the early 1960s, thermoanalytical applications called for a move away from symmetrical beam balances to substitution balances operating on the principle of electromagnetic force compensation. The more complex sample carrier systems in the newer type of balance permit heavier loads on the weighing instrument. The new design made it possible not only to use these balances strictly for thermogravimetry, but also to add measuring systems for differential thermal analysis (DTA), to determine both the change in sample mass and energetic changes, with accurate transition temperatures, in a single experiment. NETZSCH-Gerätebau GmbH was among the pioneers in this field and continues developing these simultaneous applications to a high degree of perfection to this day. The leading product for simultaneous thermal analysis is the STA 449C Jupiter®, which is based on an ultramicrobalance from Sartorius (fig. 10). This highly-sensitive system has a readability of 0.1 µg effective over the entire weighing capacity of 5 g (including the sample crucible). The broad selection of furnaces and measuring systems and the choice of sample atmospheres available support a variety of applications

for these high-performance devices in analyses. For example, a high vacuum sample chamber enables accurate determination of vapour pressure in accordance with the Knudsen effusion method.

In addition to the high accuracy and long-term stability of weighing results, the STA 449C Jupiter® delivers unparalleled calorimetric data through the use of special sample carriers for differential scanning calorimetry (DSC). The DCS sample carriers can be used in temperatures ranging from -120°C to 1,650°C, and can be calibrated for determination of enthalpy changes and transition temperatures. In particular, exact determination of specific heat capacity and melting temperatures of solids can be performed at up to 1,450°C.

The most important features are the stability of the top-loading sample carrier and the vertical positioning inside the STA furnace. This ensures that the heat conducted into the chamber is evenly distributed and reproducible on both the sample side and the reference side of the DSC sensor.

Furthermore, the compactness of the ultramicrobalance system facilitates installation in the temperature-stabilized high-vacuum chamber, thus permitting a rapid change of atmosphere in the overall system once the chamber has been evacuated to the pressure required for purity. The vertical flow around the sample is laminar, producing a controlled and effective upward flow of gases escaping from the sample (“chimney effect”).

Moreover, it is easy to couple different gas analyzers to the top side of the furnace; for example, to record the gas composition at any time, simultaneously with the change in mass. Effective protection of the weighing system from corrosive sample by-products is easily provided by flushing a small amount of protective gas through the weighing chamber with the vertical outlet. A unique sample carrier lift mechanically protects the expensive weighing system when samples are placed on the sample carrier by breaking mechanical contact to the weighing instrument as soon as the motorized lifting device, which we call a hoist, opens the STA furnace.

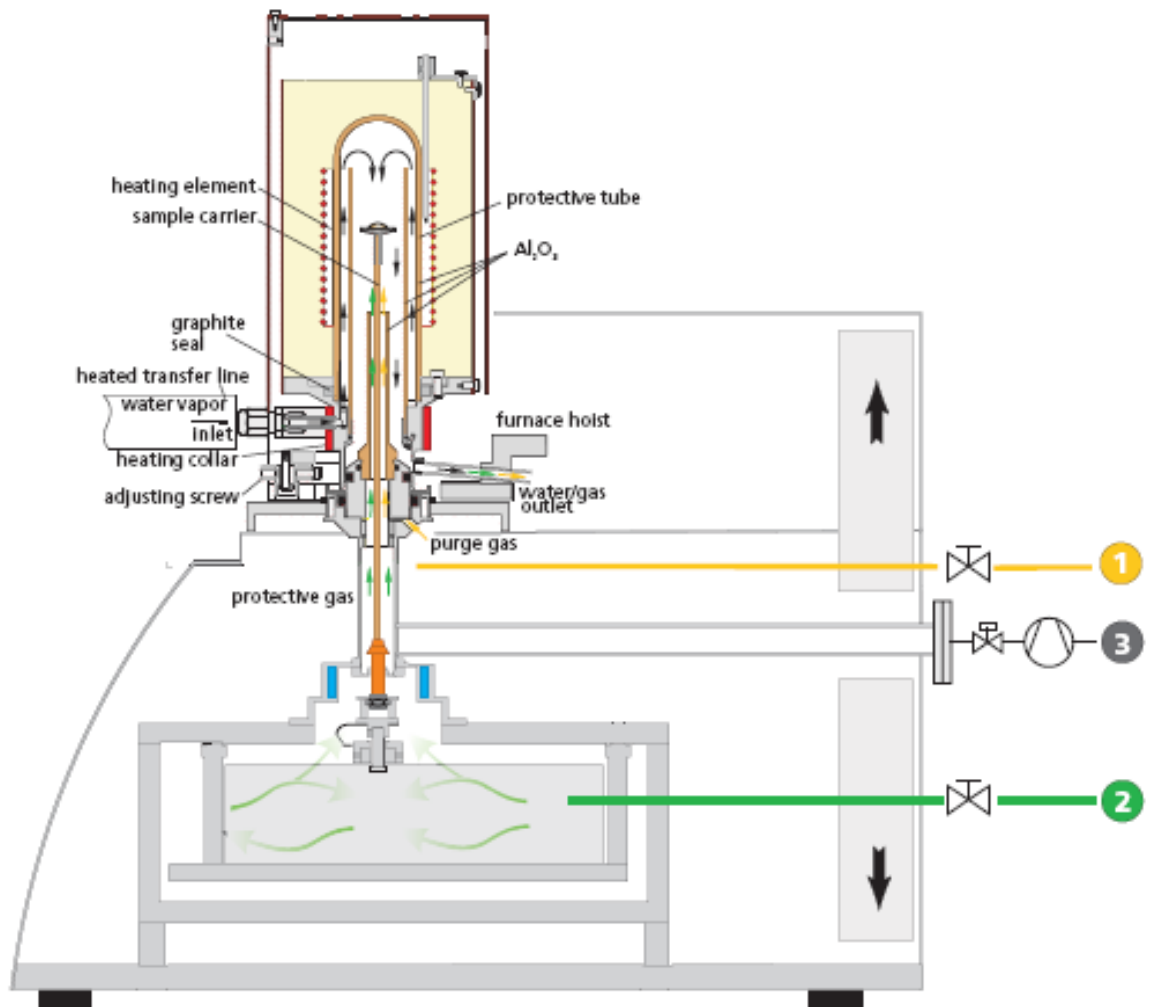


Figure 10 Furnace system for measurements under water vapour atmosphere.

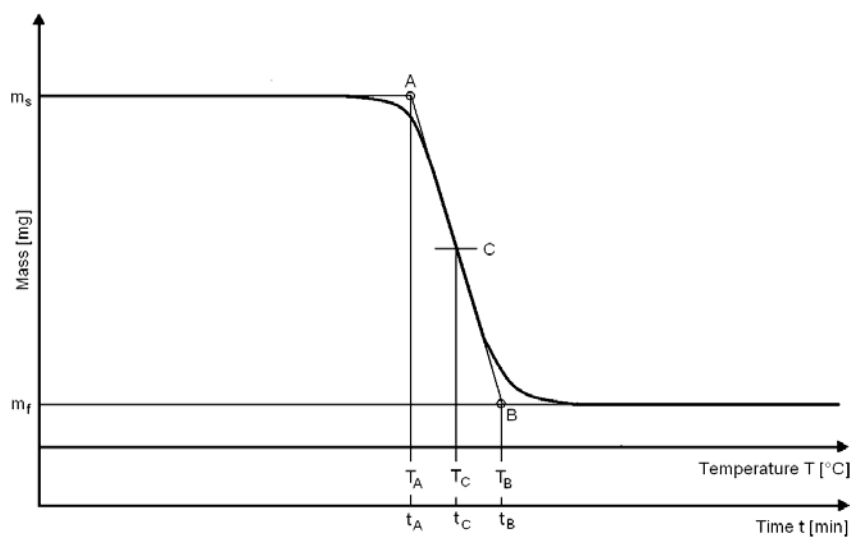


Figure 11 TG-curve (1) with one-level mass reduction according to DIN EN ISO 11358.

Interpretation of a typical TG-curve is as follows:

1. One-level mass reduction (Fig. 11):

- Mass reduction ML:

$$M_L = \frac{m_s - m_f}{m_s} \times 100\% \quad \text{Equation 43}$$

- Mass increase MG:

$$M_L = \frac{m_{\max} - m_s}{m_s} \times 100\% \quad \text{Equation 44}$$

A (initial point) – intercept point of extrapolation straight line for the initial mass with the tangent on the TG-curve in maximal gradients

B (end point) - intercept point of extrapolation straight line for the end mass after reaction with the tangent on the TG-curve in maximal gradients

C (middle point) - intercept point of the TG-curve with the parallels to the x-axis across the middle point between A and B

T_A/t_A (initial temperature/time) – temperature/time in middle point

m_s (initial mass) – mass before the heating-up

m_f (end mass) – mass after achievement of end temperature

2. Multistage mass reduction (Fig. 12)

m_1 – mass between two mass reductions

Mass reduction for multistage mass reduction of TG-curve (2):

$$M_{L1} = \frac{m_s - m_i}{m_s} \times 100\% \quad \text{Equation 45}$$

$$M_{L2} = \frac{m_i - m_f}{m_s} \times 100\% \quad \text{Equation 46}$$

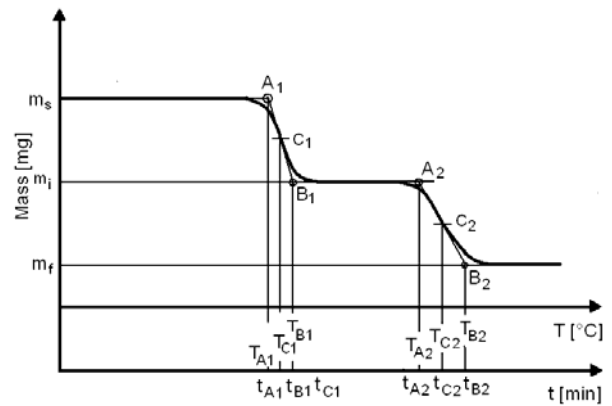


Figure 12 TG-curve (2) with two-levels mass reduction according to DIN EN ISO 11358.

3.1.6 PARTICLE SIZE ANALYSIS BY LASER DIFFRACTION

All powder particles were analysed by a laser particle size analyzer CILAS 1180 in the range of 0.04-2.500 μm in a wet dispersion mode before and after the millings.

The CILAS 1180 uses a new patented technology (laser diffraction and CCD camera) which allows, in one single range, the measurement of particles between 0.04 and 2,500 μm (Fig. 13). The fine particles are measured by the diffraction pattern, using the Fraunhofer or Mie theory. The coarse particles are measured using a real-time Fast Fourier Transform of the image obtained with a CCD camera equipped with a digital processing unit (DSP).

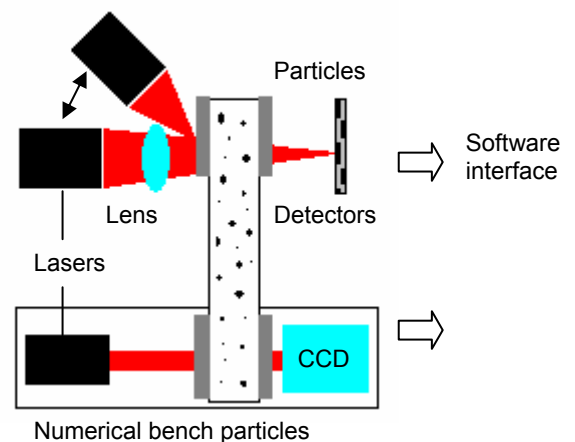
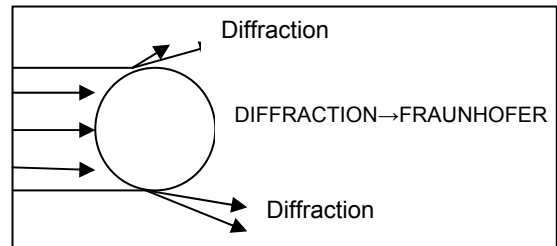


Figure 13 CILAS 1180 system for particle size measurements.

Two theories are used depending on the size of the particles:

- **Fraunhofer Theory (diffraction)**

The Fraunhofer theory is applicable for large particles compared to the wavelength λ (diffusion and absorption are not considered) (Fig. 14).



For smaller particles, it is appropriate to use the Mie Theory. The Mie model takes into account both diffraction and diffusion of the light around the particle in its medium (Fig. 15). To use the Mie model, it is necessary to know the complex refractive index of both the sample and the medium. This complex index has a real part, which is the standard refractive index, and an imaginary part, which represents absorption.

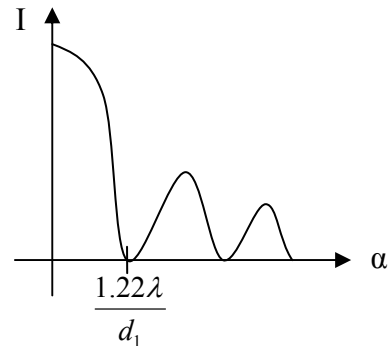


Figure 14 System for a large particle (Fraunhofer theory).

Complex index m : $m = a + b$

a - real part; b - imaginary part

- **Mie Theory (diffraction - diffusion)**

The observation of the diffraction pattern at finite distance is done through a lens placed between the laser source and the detector. The diffraction patterns of particles of the same size converge at the same point whatever their location with respect to the lens. The first zero on the detector is $1.22 \lambda f/d$ where f is the focal length. Because of the importance of this model, CILAS has created a fast algorithm which enables the user to get, within seconds, diffusion results using the Mie theory and taking into account the complex index of the sample (Fig. 15) [88].

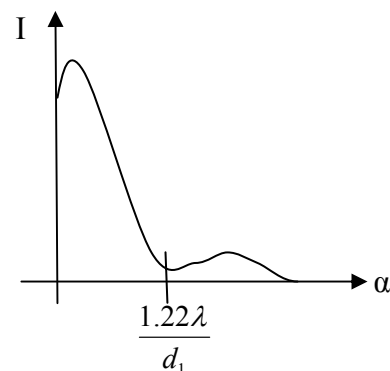
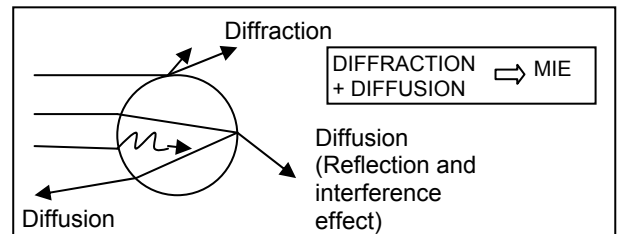


Figure 15 System for a small particle (Mie Theory).

3.1.7 PARTICLE SIZE ANALYSIS AND ZETA POTENTIAL MEASUREMENTS

Stern Double Layer

Stern considered the possibility of specific ion adsorption giving a compact layer of counter-ions attached to the surface by electrostatic and van der Waals forces strongly enough to overcome thermal agitation. The total double layer is considered to be two separate parts – a compact (Stern) layer, where the potential changes from ψ_0 to ψ_δ , and a diffuse layer, where the potential drops from ψ_δ to zero – with the two layers in equilibrium. The potential charge in the Stern layer increases with electrolyte concentration (Fig. 16).

Zeta Potential

Electrokinetic behaviour depends on the potential at the slipping plane between the charged surface and the electrolyte solution. This potential is called the electrokinetic or ζ (zeta) potential. The water layer around a molecule is bound to the charged surface by charge-dipole interaction. The surface of shear is located outside the Stern layer, and ζ is smaller in magnitude than ψ_δ . The potential drop will occur by increasing the electrolyte concentration.

The ionization of carboxyl and amino groups, i.e. the primary charges on the protein molecule, depend strongly on the pH of the solution. At low pH the protein molecule will be positively charged and at high pH it will be negatively charged. The pH at which the net charge is zero is called the isoelectric point.

The ZetaPALS equipment utilizes phase analysis light scattering to determine the electrophoretic mobility of charged, colloidal suspensions. The zeta potential of colloidal dispersions was routinely measured using the technique of microelectrophoresis. In this technique, a voltage was applied across a pair of electrodes at either end of a cell containing the particle dispersion. Charged particles were attracted to the oppositely-charged

electrode and their velocity was measured and expressed in unit field strength as their mobility.

Calculation of Zeta Potentials

Reference will frequently be made to " κa " (the ratio of particle radius to double layer thickness). When κa is small, the particle may be considered as a point charge. When it is large, the double layer is almost flat and the treatment outlined is applicable.

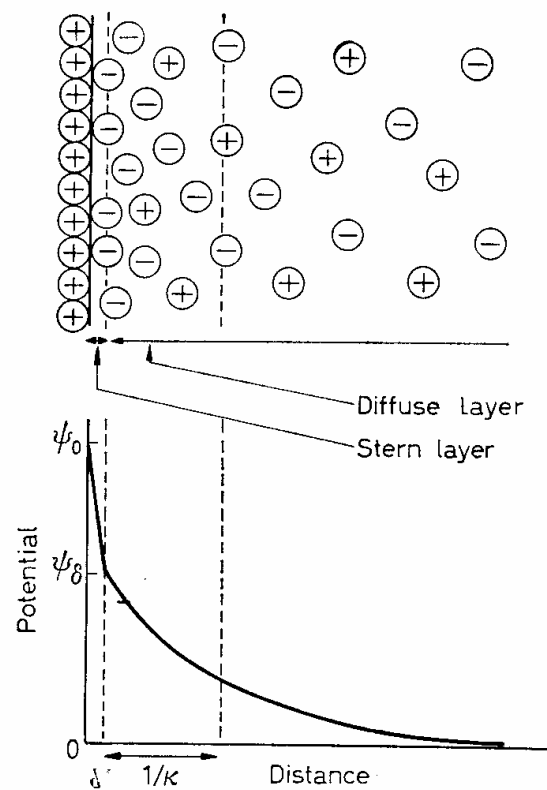


Figure 16 Schematic representation of the structure of the double layer according to Stern's theory.

- **Hückel's equation** for small values of κa -Consider κa to be small enough for a spherical particle to be treated as a point charge., but let the particle be large enough for Stokes' law to apply. Equating the electrical force on the particle with the frictional resistance of the medium

$$QX = 6\pi\eta\alpha g_E \quad \text{Equation 47}$$

$$\text{or } u_E = \frac{g_E}{X} = \frac{Q}{6\pi\eta\alpha} \quad \text{Equation 48}$$

where Q is the net charge on the particle, X the potential gradient, η the viscosity of the medium, α the radius of the particle, \mathcal{G}_E the electrophoretic velocity, and u_E the electrophoretic mobility.

The zeta potential is the resultant potential at the surface of shear due to the charges +Q of the particle and -Q of the ion atmosphere:

$$\zeta = \frac{Q}{D\alpha} = \frac{Q}{D(\alpha + 1/\kappa)} = \frac{Q}{D\alpha(1 + \kappa\alpha)}$$

Equation 49

where D is the dielectric constant of the medium. Therefore

$$u_E = \frac{\zeta D}{6\pi\eta}$$

Equation 50

- **Smoluchowski's equation** for large values $\kappa\alpha$: Consider the relative motion of a non-conducting flat surface and the liquid in the diffuse double layer when an electric field X is directed parallel to the surface (Fig. 17).

The integration constant is zero, since at $x = \infty$, $d\psi/dx = 0$ and $dv/dx = 0$.

Integrating

$$-\frac{DX}{4\pi}\psi = \eta\mathcal{G} + const$$

Equation 51

If the shear plane is assumed to be in the diffuse part of the double layer, then $\psi = \zeta$ and $v = -v_E$ at the shear plane (v_E =electrophoretic velocity). Therefore

$$\frac{DX}{4\pi}\zeta = \eta\mathcal{G}_E$$

Equation 52

or

$$u_E = \frac{\mathcal{G}_E}{X} = \frac{\zeta D}{4\pi\eta}$$

Equation 53

To convert from electrostatic units of potential difference to volts, both ζ and X must be multiplied by 300. In aqueous medium at 25 °C, with mobility expressed in $\mu \text{ sec}^{-1}/V \text{ cm}^{-1}$

$$\zeta = 12.9 u_E \text{ mV}$$

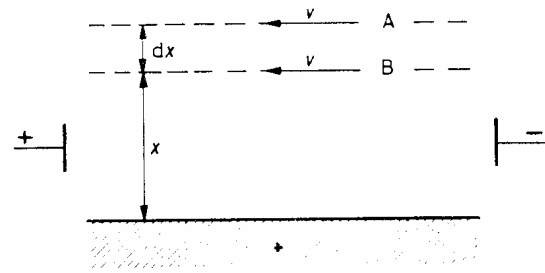
Equation 54

- **Henry's equation** for any value of $\kappa\alpha$: Henry derived a general electrophoretic equation for non-conducting spheres, which can be written in the form

$$u_E = \frac{\zeta D}{6\pi\eta} f(\kappa\alpha)$$

Equation 55

$f(\kappa\alpha)$, known as Henry's function, varies between 1.0 for small values of $\kappa\alpha$ and 1.5 for large values of $\kappa\alpha$ (Fig. 18). The Hückel and Smoluchowski equations hold to within 1 per cent for $\kappa\alpha \leq 0.5$ and $\kappa\alpha \geq 300$ respectively. Unfortunately, much of the field of interest in colloid science lies between these values [89].



Along plane A, shearing force per unit area = $\eta \frac{dv}{dx} + \frac{d}{dx} \left(\eta \frac{dv}{dx} \right) dx$
 Along plane B, shearing force per unit area = $\eta \frac{dv}{dx}$

Figure 17 Derivation of Smoluchowski's equation.

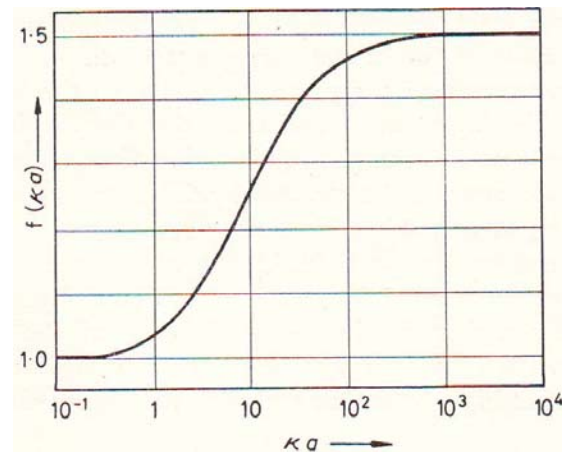


Figure 18 Plot of $f(\kappa a)$ against κa .

3.2 EXPERIMENTAL SET UP

3.1.8 TEST STAND

The gas flow was controlled by mass flow controllers. Water supervised by a water pump was vaporized by an evaporator and subsequently mixed with the gaseous reactants. The inlet and outlet gas concentration was detected by online gas analyser (Fig. 19).

3.1.9 REACTOR

The catalyst coating was applied to five microstructured foils (50 mm x 50 mm x 1 mm), containing 49 channels: 400 μm deep and 600 μm wide (Fig. 20b). The coated foils were stacked with filler plates inside of stainless steel housing. Microreactor (Fig. 20a) and foils (Fig. 20c) were made of stainless steel (DIN 1.4571). Four 250 W heating cartridges were installed into the microreactor housing, two of them in the upper and two in the lower part of the reactor. The reactor temperature was measured with two thermocouples located in the housing. The gas flow was controlled by mass flow controllers. Water supervised by a water pump was vaporized by an evaporator and subsequently mixed with the gaseous reactants. The inlet and outlet gas concentration was detected by online gas analyser (Fig. 19).

3.1.10 ONLINE GAS ANALYSIS

3.1.10.1 INFRARED ANALYSER

MODULE: URAS 14

The Infrared analyser Module *Uras 14* is a non-dispersive infrared photometer (NDIR) for the

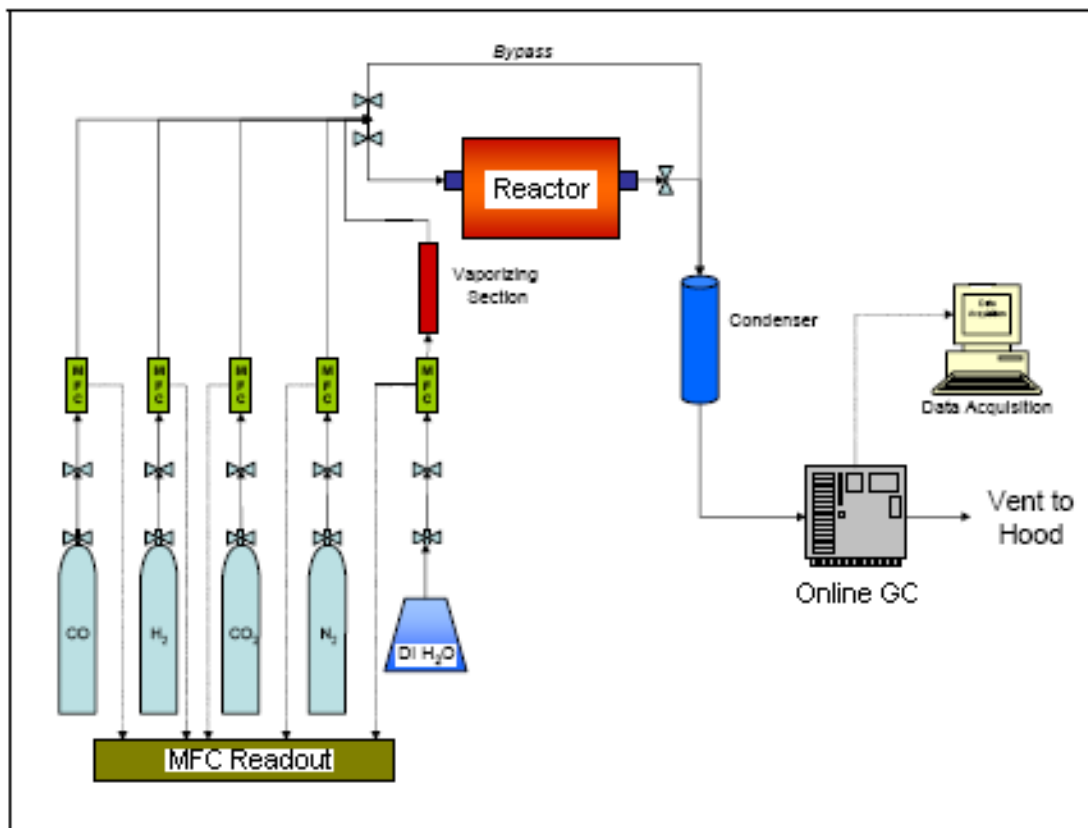
simultaneous and continuous measuring of 1-4 components. Typical measuring components include CO, CO₂, NO, SO₂, N₂O, CH₄, C₃H₈ and C₂H₄.

The NDIR-method is based on the resonance absorption of IR radiation by characteristic swinging rotation band of non-elementary gases in the average infrared between 2 μm and 12 μm . The gas molecules interact with the infrared rays due to their dipole moments.

The photometer consists of a thermal radiator, whose radiation falls due to a modulation device in measuring cuvette through a modulation device. The measuring cuvette is designed as a tube divided on measuring and comparative side by a bridge. The measuring effect is a pressure effect accompanied by frequency of the receiver that is absorbed by a membrane condenser and transformed into an electrical signal in an affiliated preamplifier (Fig. 21).

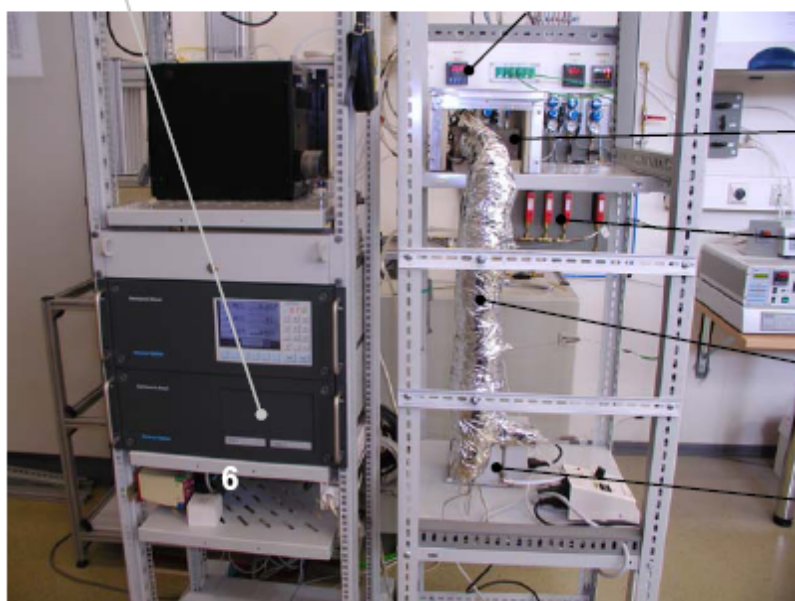
The receiver is based on a two-layer receiver. It has an optical transparent window on the backside so that the residual radiation is attained in a second receiver, which is sensitized to the second component. 1-4 measuring components are simultaneously detected through the integration of a second optical path with radiator, measuring cuvette and receiver.

The calibration of the infrared analysis module ensues with a zero gas for a zero point and with an end point gas for an end point. Non-measuring component ambient air is used as zero gas and will be piped through the measuring cuvette. A gas filled calibration cuvette is moving in to the optical path for the end point calibration; therefore the application of bottles with test gas is not required for the routine calibration.



Gas analyzer

Temperature control



Micro reactor

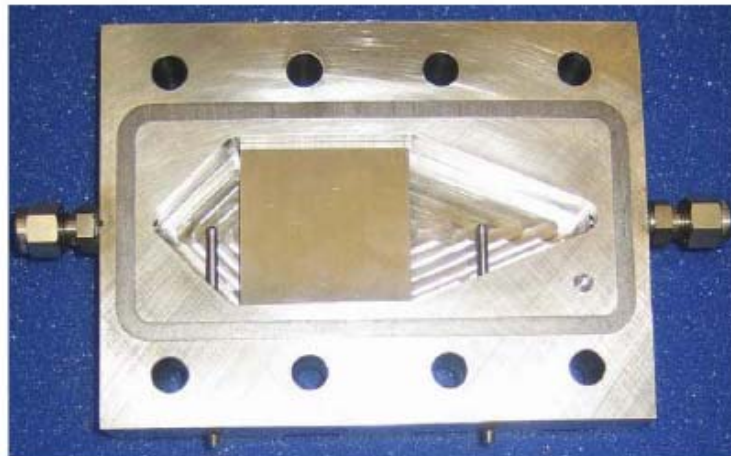
Mass Flow Controller

Evaporator

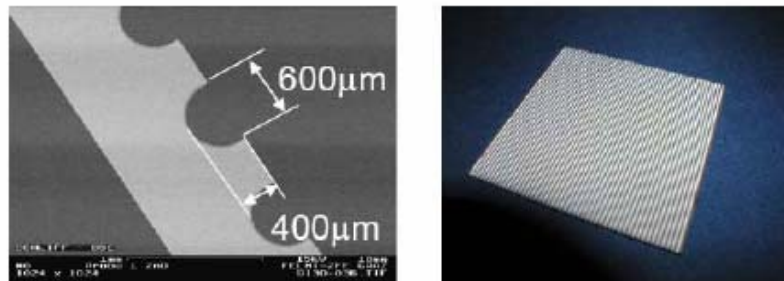
Water pump

Figure 19 Test stand equipment.

(a)



(b)



(c)

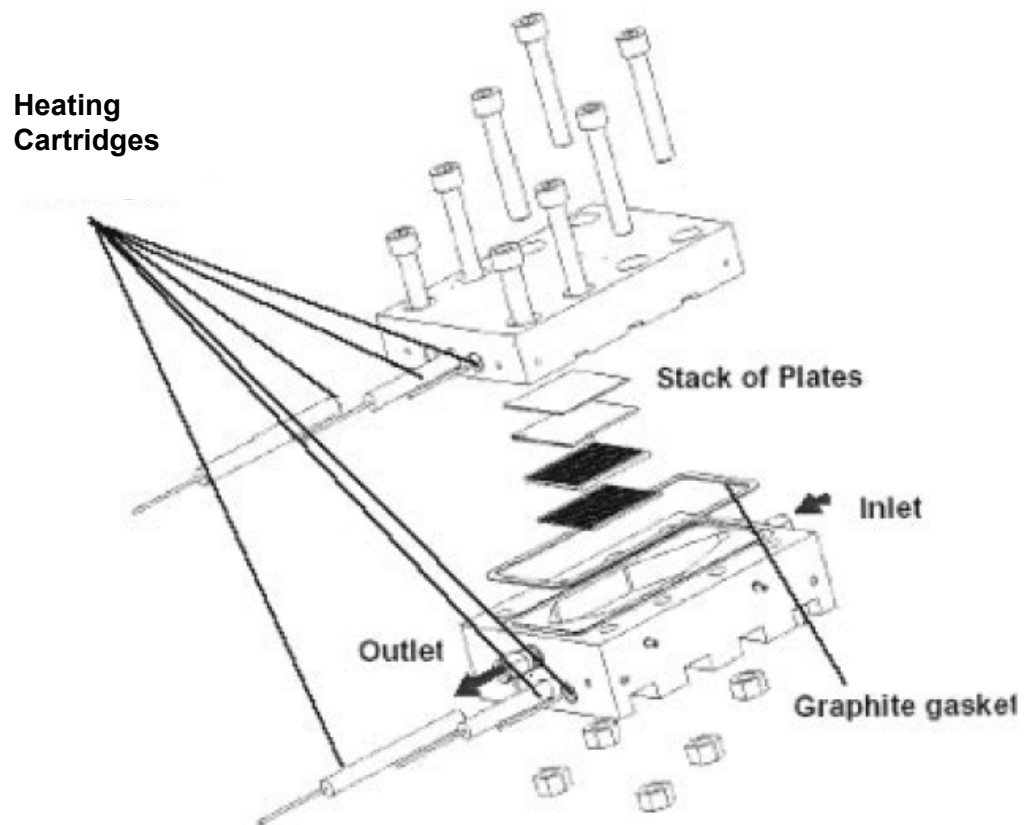


Figure 20 Microreactor (a); microstructured devices (b). Reactor housing with microstructured platelets (c).

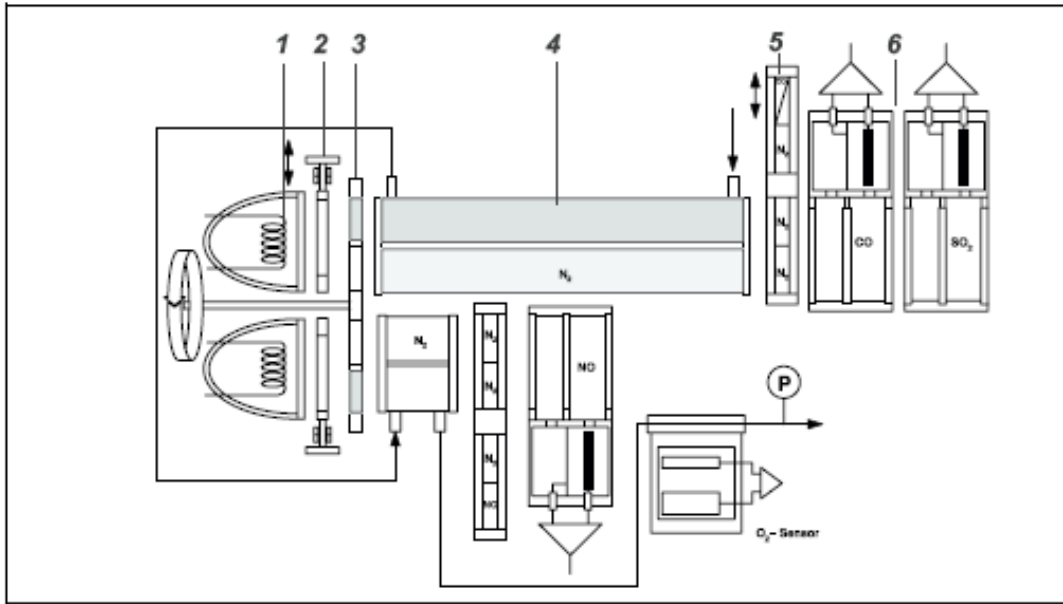


Figure 21 Measuring principle (1 – radiator, 2 – aperture, 3 - modulation device, 4 - measuring cuvette, 5 - adjustment unit / calibration unit, 6 – receiver).

3.1.10.2 THERMAL CONDUCTIVITY

ANALYSER MODULE:

CALDOS 17

Caldos 17 exploits the varying thermal conductivities of different gases such as Ar in O₂, H₂ in Ar, H₂ in N₂/air, CH₄ in N₂/air, Ar in N₂, He in N₂. Measurement is carried out by a silicon sensor that allows especially rapid gas measurement and extremely small measuring ranges.

The thermostat space is a cylinder-shaped polyester body, which is closed with gas-proofed mounting flange down. The gas-proof analyser modules could be flush separately from the centre unit. The analysed gas diffuses into the measuring chamber, where a heat conductivity sensor composed of three silicon chips is situated. The middle chip contained a membrane covered with two thin-film resistors. The resistors are heated-up by electric current (Fig. 22). The resistance switches off the measuring gas. The thermal energy will

be dissipated from the membrane due to heat conductivity of measuring gases. The electricity used for the temperature difference retention between the resistors is a quantity for the concentration of the measuring gas components. The measuring unit is situated in thermostat housing, where the measured variable is largely independent from fluctuations in room temperature [90].

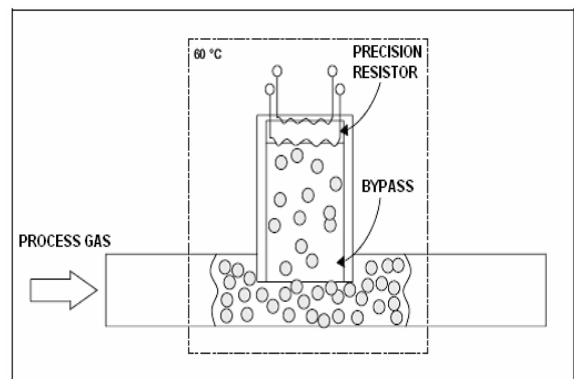


Figure 22 Measuring principle.

CHAPTER B

HANDS-ON WORK

4 CHARACTERIZATION OF HTS AND LTS REACTIONS IN MICRO-STRUCTURED REACTORS ^[121]

4.1 EXPERIMENTAL

4.1.1 CATALYST PREPARATION

The four commercial powder catalysts were first dry milled for 10 h by using a planetary mill (Pulverisette 4, Fritsch) by rotation of a supported disc (rotation velocity of 229 min^{-1}) and grinding bowls (238 min^{-1}). This preparation method was based on a concept proposed by Y. Men et al. [35]. The coating slurries were prepared from the untreated (I-PtX-1, II-PtY-1, RuZ-1 and CuXY-1) and the milled (I-PtX-2, II-PtY-2, RuZ-2 and CuXY-2) powder catalysts. The slurries consisted of binder (polyvinyl alcohol-PVA), acetic acid with a weight ratio 5:1, commercial powder catalyst and de-ionized water (1:3.75). PVA was improved adhesion between layer and metal (stainless-steel) substrate during drying and calcinations and reduced cracks formation of the layer. Thermo gravimetric analysis (TGA) was conducted to confirm the reducing effect of evaporation rate by PVA addition in each slurry.

The PVA-binder was dissolved in water and the solution was stirred at $60 \text{ }^\circ\text{C}$ for 2 h and then left overnight in a vessel for the release of air bubbles. The powder catalyst and acetic acid were next added and stirred overnight. The acidic components were used to peptize the slurry. In this way the pH was controlled, which adjusted at the variances for viscosity of the catalyst slurries. All catalyst samples were rested than for two weeks to release air bubbles.

In case of the Pt/CeO₂ catalyst CeO₂-nanopowder (Aldrich), acetic acid and 1 wt.% H₂PtCl₆ x H₂O were added to prepared slurry consisted of PVA and water

and then stirred together overnight. The lower water content in the first step of preparation was compensated than with the aqueous H₂PtCl₆ x H₂O.

4.1.2 COATING OF THE PLATES (WASH COATING)

The micro-structured substrates were first cleaned in an ultrasonic bath with 2-propanol, then dried and heated in air at $900 \text{ }^\circ\text{C}$ for 3 h. After positioning and masking the substrates, the prepared wash coat slurry was deposited onto the micro-structured channels. The micro-channels were filled completely and surplus slurry was removed by a stainless-steel knife with a flat edge. After coating, the plates were dried overnight at room temperature [97]. Then the wash coats were calcined in hot air at temperatures and time suitable for different types of catalysts. The amount of catalyst applied with each plate was approximately 0.1 g. This was determined by the amount of catalyst powder in the aqueous suspension.

4.1.3 CHARACTERIZATION OF THE CATALYST

The crystal structure of the powder catalysts was investigated by powder X-ray diffraction. The results were obtained on a Bruker AXS (Siemens) D5005 θ - θ diffractometer using filtered Cu K α radiation and a graphite secondary-beam monochromator. Diffraction

intensities were measured by scanning with steps of 0.05° (2θ) and 5-20 sec/step. Scanning electron microscopy (SEM) analyses were performed on a JEOL JWS-7515. BET-surface areas were determined using an *Autosorb-1 (Quanta chrome)*. The powder catalyst samples were first dried at elevated temperatures. Then the surface area values were gathered at a constant temperature of 77 K (liquid nitrogen). All powder particles were analyzed by a laser particle size analyzer CILAS 1180 in the range of 0.04-2.500 μm in a wet dispersion mode before and after the millings.

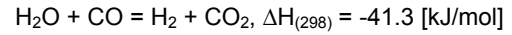
4.1.4 EXPERIMENTAL CONDITIONS

The catalyst coating was applied to five micro-structured foils (50 mm x 50 mm x 1 mm), containing 49 channels (400 μm deep and 600 μm wide). The coated foils were stacked with filler plates inside of a stainless steel housing. Micro-reactor and foils were made of stainless steel (DIN 1.4571). Four 250 W heating cartridges were installed into the micro-reactor housing, two of them in the upper and two in the lower part of the reactor. The reactor temperature was measured with two thermocouples located in the housing. The gas flow was controlled by mass flow controllers. Water was vaporized and subsequently mixed with the gaseous reactants. The temperature of the reactor was raised to 350 °C at a rate of 4 °C/min and then kept constant for 1 h (300 °C for 40 min for RuZ catalyst) in a gas flow of 10 % H₂ in N₂ with all of the measurements. After this procedure, the reactor temperature was set to the first reaction temperature and the reactor was purged with pure nitrogen. Then the experiments started with the corresponding feed gas compositions (Tab.7).

The gas mixture was applied in microchannel volume V_R [mm³] with the total inlet mass flow [ml/min]. The variation of residence time can be calculated by following equation 49:

$$\tau = \frac{V_R [mm^3]}{\dot{V} [l/min]} \quad \text{Equation 56}$$

The different water content in the feed gas had a strong influence on the catalysts CO-conversion rate, following the WGS reaction equation 50. These variations in the input gas water concentration were compensated with nitrogen as a balance factor.



Equation 57

The CO-conversion was compared between unmilled and milled catalysts. The measured inlet concentrations [CO]_{in} and outlet concentrations [CO]_{out} were used to calculate the conversion X[CO], which is can be defined:

Table 7 Experimental Conditions for HTS and LTS

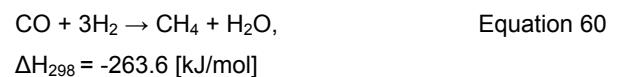
Gas composition [vol.%]		
	HTS	LTS
H ₂	22.6	31.37
CO ₂	11.6	18
CO	8	2.24
N ₂	30.6	21.16
H ₂ O	27.2	27.2
Reaction temperature [°C]		
	300	200
	350	250
	400	300

$$X(CO) = \frac{[CO]_{in} - [CO]_{out}}{[CO]_{in}} \times 100\% \quad \text{Equation 58}$$

The CO-conversion rate in the water gas shift reaction each catalyst was compare with the equilibrium curve using the equation:

$$K^{eq} = \frac{[CO_2] \cdot [H_2]}{[CO] \cdot [H_2O]} \quad \text{Equation 59}$$

The undesirable methanation occurs in parallel to the water gas shift reaction were defined as follows:



An important sequence in which the metals promote methanation was reported as Ru>Rh>Ni>Pt>Pd. Methane formation on platinum (Pt) and palladium (Pd) was about 1%, and approximately 10 % on ruthenium (Ru). It was also found, that the addition of ceria had a small effect on CH₄ formation [94]. From literature, another following activity ranking as Ru > Rh >> Pt/CeO₂ >> Pd/CeO₂ was reported for the methanation reaction, which starts at temperatures higher than 300 °C for ruthenium (Ru) and rhodium (Rh) and reaches its maximum at 500 °C, whereas it initiates at 400 °C for platinum (Pt) and 500 °C for palladium (Pd) [98].

4.2 RESULTS AND DISCUSSION

4.1.5 GEOMETRIC STRUCTURE OF THE CATALYST LAYERS

Many factors such as the time, the temperature and particle sizes influence strongly on the changes in catalytic crystalline structure and its activity during the powder milling and catalyst layer calcinations process. Pfeifer et al. [48] investigated the washcoat properties of mixed systems of CuO milled powders. They proved that these layers were just a little more active in the initial state. However, the addition of TiO₂ to the mixture of CuO, ZnO and Al₂O₃ decreased the initial activity but elevated the stability of the catalyst.

Zhao et al. [96] studied the coating properties of a milled powder of Al₂O₃ strengthened NiCr after the spraying process. The coatings were harder and more resistant than the homogenous microstructures of the milled powders. In addition, these homogenous coatings had a lower hardness than their powders.

In this work the uniformity of the catalyst layer was considerably affected by the catalyst particle size reduction. Additional to better understand their impacts on a coating effect, Fig. 23 and Fig. 24 present the particle sizes distribution for commercial catalysts

before and after the milling process. Two clearly visible peaks are situated in the highest (10- 170 μm) and lowest (0.04-1.3 μm) particle size areas for each untreated powder (Fig.23).

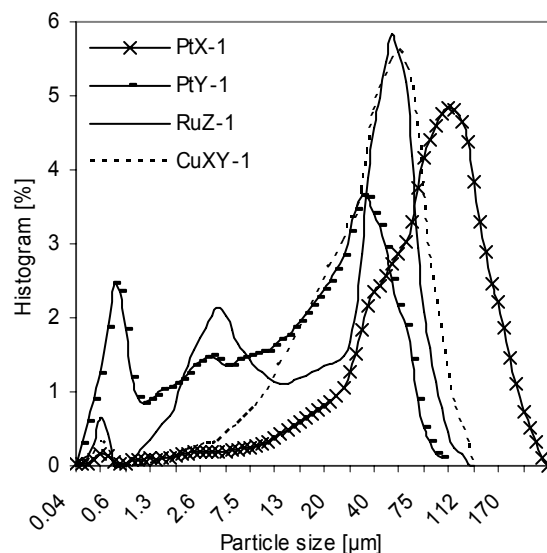


Figure 23 Particle size of catalyst powder before milling.

Table 8 Specific mass, BET surface area, and calcination parameters for the catalyst samples applied onto the microstructured foil

Catalyst type	Catalyst mass [mg]	BET SA [m ² /g]	Calcination temperature [°C]	Calcination time [min]
PtX-1	513	86.6	400	60
PtX-2	471	82.7	400	60
PtY-1	455	102.3	400	60
PtY-2	443	92.8	400	60
RuZ-1	453	381.1	540	100
RuZ-2	484	255.3	540	100
CuXY-1	421	Not measured	480	80
CuXY-2	646	Not measured	480	80
CeO ₂ *	-	80-100	-	-
Pt/CeO ₂	513	-	400	60

(*) – Particle diameter for CeO₂: d = 10-20 nm

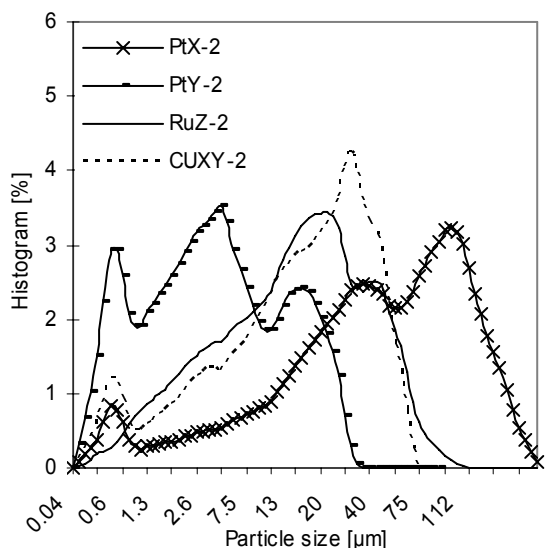


Figure 24 Particle size of catalyst powder after milling.

Moreover a one additional peak is located in between for the PtY-1, RuZ-1, PtX-2 and PtY-2-catalysts. Milling reduced the catalyst particles in size of 40-120 μm (Fig. 24) as well as the BET surface areas given in Tab.8 for all commercial powders (catalyst-1: before milling; catalyst-2: after milling).

Although the PtX and the PtY catalysts in Fig. 25 to Fig. 28 have a very good adhesion for both particle size forms, but their milled particles were more homogeneously distributed in micro-channel after coating. Just these untreated catalyst layers show small local holes with planar surfaces around, which are caused by the diffusion at high temperature during calcinations.

However the largest particle sizes in the region of 75-170 μm are noted for the PtX-1-catalyst in Fig. 23, only the particle sizes in 10-30 μm were very visible on the surface layer after calcinations in Fig. 25. The PtY-1-catalyst had smaller amount of regional particles in diameter of 30-50 μm in compare to the PtX-1.

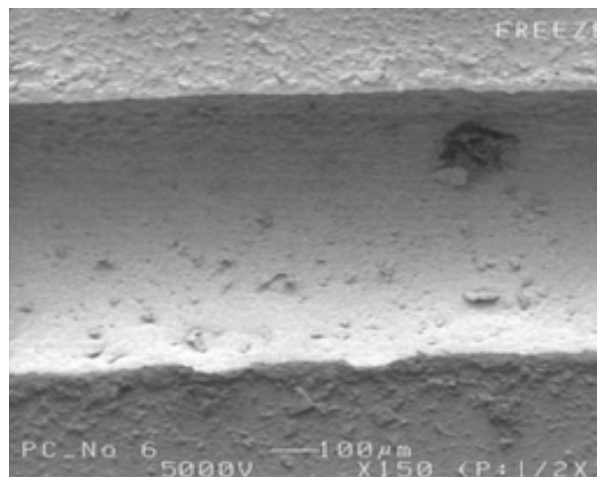


Figure 25 SEM of the PtX-1 catalyst on a microstructured stainless steel foil.

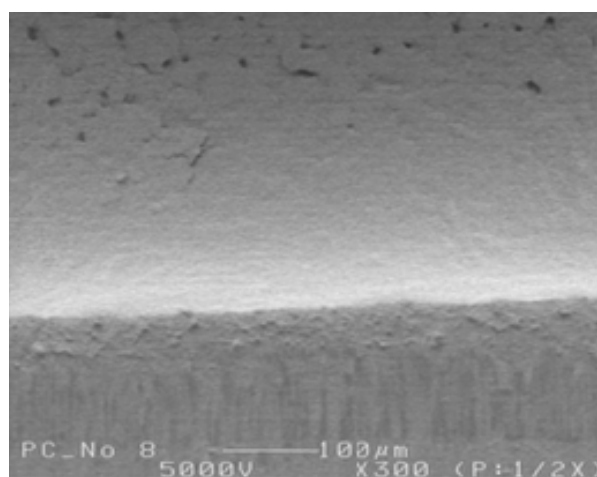


Figure 26 SEM of the PtX-2 catalyst on a microstructured stainless steel foil.

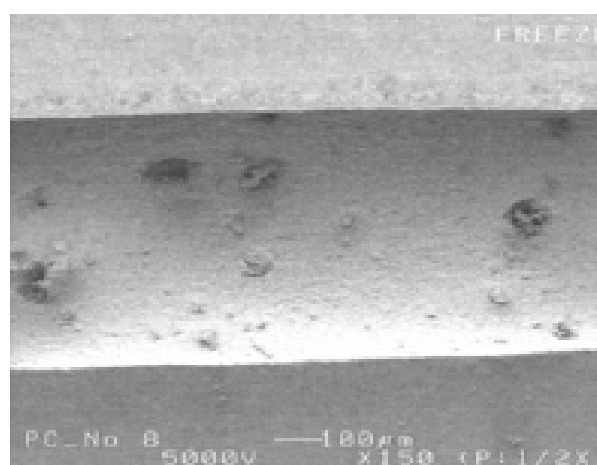


Figure 27 SEM of the PtY-1 catalyst on a microstructured stainless steel foil.

Fig. 29 shows perfect adhesion properties for the RuZ-1-catalyst compare to all presented catalyst coats. It reached subsequently two highest volume dispersions for the grain sizes of 57.5 μm and 5 μm . In the contrast to the morphology of the RuZ-1, the catalyst layer of the RuZ-2 with one highest concentration in 20 μm particle diameter has only few cracks on the catalyst surface, as shown in Fig. 30. For this catalyst was observed that choose of the favourable calcination parameters like temperature and time was depended on the catalyst particle sizes. The preceding factors were the one most important in the optimisation of the stable catalyst layers. CuXY-1, 2-catalyst, as Fig. 31 shows, exhibit the same large cracks on the layer surfaces with the one clearly particle size ranges of 75 μm before and 35 μm after milling.

Cracks in last two catalyst coats were showed after solvent diffusion during calcinations, wherein atoms were moved from their original sites after bonds broking. Atoms move more easily over the surface of catalyst layer or along grain boundaries than through its bulk, as it was observed for RuZ-2 catalyst. Less densely packed coats promote diffusion over more densely packed planes, which were noted for catalysts such CuXY- 1-2, RuZ-2 and Pt/CeO₂ with narrow particle size range responsible for higher porosity. Density is influenced by structure, phase and porosity. During calcinations the reduction in porosity was preceded with grains growth and significant strength decrease, which were leaded to catalyst layer breakages.

The commercial catalysts were deposited on to micro-channels using aqueous slurries (PtX, PtY and RuZ) and one sol-gel-based slurry (CuXY). As shows Tab. 8, the CuXY layer is thicker than for the aqueous slurries, which is improved by larger catalyst mass on the microstructures after coating and calcination. At the moment of drying of the CuXY coat the constituent particles were submitted to a large capillary tension which decrease as the diameters of the pores increase and leaded to cracks. This capillary force was bringing the particles closer together as the liquid (solvent) was removed.

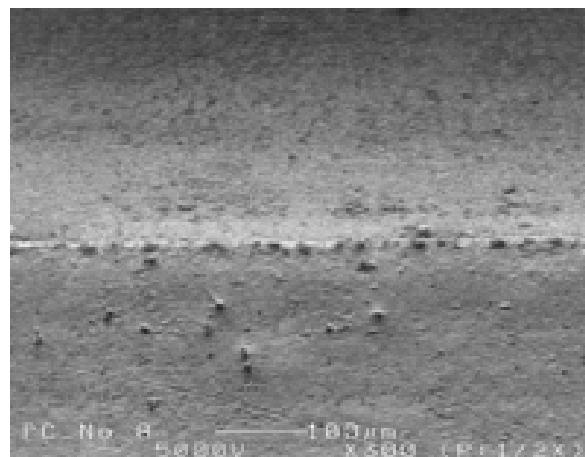


Figure 28 SEM of the PtY-2 catalyst on a microstructured stainless steel foil.

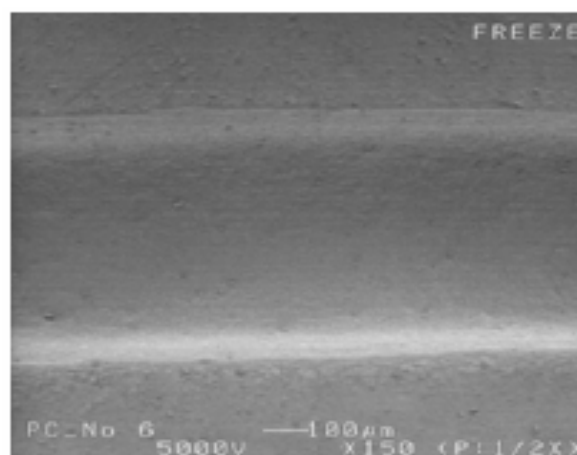


Figure 29 SEM of the RuZ-1 catalyst on a microstructured stainless steel foil.



Figure 30 SEM of the RuZ-1 catalyst on a microstructured stainless steel foil.

During calcination a macroporous texture with cracks was created through decomposition and volatilization of substances previously added to the solid. The texture was partially modified through sintering, wherein small particles were turned into bigger ones. Wear in this coat was undesirable in the sense of losing material. Shrinking of the catalyst layer caused uneven surface removal which encouraged grain pull-out. Catalyst grain with less dense packing orientated along the surface of the coat were suffered the most degradation. Therefore, the aqueous catalyst slurries such as PtX, PtY and RuZ thanks to their great layer uniformity turned out that they were better favourable for the distribution on to microchannels than the CuXY-gel. Additionally, the effect of the acid concentration (the pH of slurry) was examined for the commercial and Pt/CeO₂ catalysts. In this way their layer uniformity was achieved by the viscosity variation. The commercial aqueous catalyst slurries had the lower viscosity and pH of 7, than Pt/CeO₂-catalyst. A clearly higher viscosity was observed for this nanocatalyst coat due to the pH of 3 after addition of acidic components such as H₂PtCl₆ x H₂O.

Fig. 31 shows cracks on the layer surfaces, which were appeared after the solvent evaporation during calcinations. As a result it was lead to the layer shrinkage. The aqueous solutions indicate a high degree of agglomeration, as it was demonstrated in literature for CeO₂ [44]. The subsequent huge capillary force and the bridging of adjacent particles with water by hydrogen bonds are mainly due the formation of hart aggregates with cracks around during drying. Fig. 32 exhibits smaller cracks in 1-5 μm for the Pt/CeO₂ catalysts after layer shrinking in compare to CuXY. This very compact solid mass, thanks to the CeO₂ particle size of 10-20 nm, which was observed by scanning microscope with the larger enlargement (Fig.32), caused the dislocation of the CeO₂ particles in larger crystals as a reason of their compounds on the coat surface during diffusion at high calcinations temperature. Pt particles of 2-8 μm in size are homogeneously distributed on the CeO₂ layer.

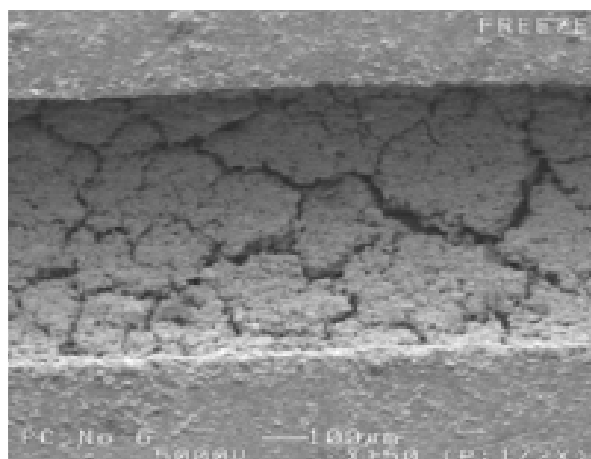


Figure 31 SEM of the Cu-XY-1 catalyst on a microstructured stainless steel foil.

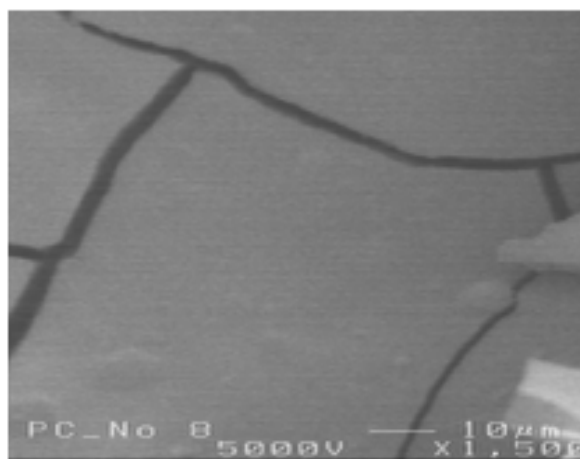


Figure 32 SEM of the Pt/CeO₂ catalyst on a microstructured stainless steel foil.

XRD measurements were performed with the self-prepared Pt/CeO₂-catalyst. No other metallic peaks such as Pt are observed in the Pt/CeO₂ wash coat by reason of the average crystallite amount of this metal was not detectable. This analysis (Fig. 33) shows CeO₂ peaks and measurable amounts of elementary iron (Fe). O. Goerke et al. [6] found other components of stainless steel such as chrome (Cr) in a Ru/ZrO₂ catalyst layer, which was distributed on stainless steel (1.4301) foils. This was probably caused by reduction of the stainless steel at high temperatures (350 °C) and from the diffusion during the calcination.

In following work only the aqueous catalyst layers with the ratio catalyst to solvent of 1:3.75 and pH of 7 proved a great distribution in micro-channel. However the

coatings can keep a uniform thickness since the suspension was of suitably concentration and viscosity but they are not the last decisive factors which determine layer equality. For all given solid catalysts descriptions were also showed the important variables on which their uniformity depended such as the size of the particles undergoing drying and than calcination, and the nature of the catalyst and solvent.

4.1.6 DETERMINING CATALYTIC PROPERTIES

In the next part of this work all catalyst coats were examined in WGS reaction conditions. Their layer uniformity was chosen to maintain their ability for CO reduction. Three different residence times were used in these tests to bring the catalytic activity in the higher levels. An increase of conversion was observed at longer residence time with decrease reaction temperature. The catalytic activity was certainly affected by the wet coating for aqueous PtX, PtY and RuZ layers. After this coating procedure their coat uniformity was observed in each micro-channel and the active sites of catalyst were the mostly open, which was resulted in the highest catalytic activity in WGS reaction. In these reasons this preparation and coating method was the most effective to catalyst coating in microstructures for WGS.

The highest CO-conversion rates were obtained with the longest residence time of 558 ms and 250 °C for all investigated catalysts (Fig.34). The PtX-1 sample reached its maximum CO-reduction rate of 81% compared with all unmilled catalysts. The second highest activity was observed for the PtY-1, which achieves 76 % CO-conversion at lower temperature than it was at shorter residence times. The temperature reduction for the highest activity was noted also for CuXY-1 catalyst. Additionally, the positive effect of milling on perfect coat uniformity in micro-channel was observed especially for the aqueous catalyst slurries.

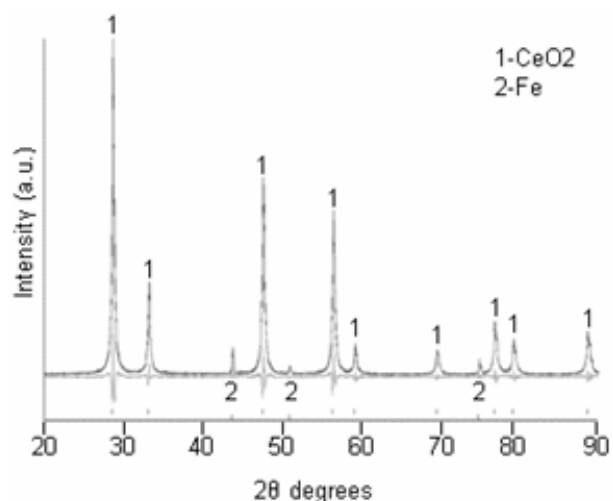


Figure 33 XRD pattern obtained for the 1 wt.% Pt/CeO₂ catalyst.

This grate layer distribution already without any particle agglomerations was observed for PtX-2-catalyst. Above mentioned catalyst shows the highest activity after milling process with 90 % CO-conversion. It attained the closest conversion near the thermodynamic equilibrium conversion rate (Fig. 35). The PtX-catalyst was obtained 1 vol.% of CH₄- concentration at the same reaction conditions.

The excellent distributed RuZ-1-2 catalyst became most active at 350 °C with the maximum CO-conversion of 74 %. Moreover, it was achieved the highest activity increase due to the predominantly parallel methanation reaction. The noticeable methane increase was observed with the longer residence time for RuZ-1-catalyst and reached its maximum of 6 vol.% at 350 °C and 558 ms. The milled form showed higher methane content only at 400 °C comparing untreated form.

On the other hand, the morphology of CuXY and Pt/CeO₂ layers proved the lower coherence, which was contributed to nonuniformity. The numerous of open active sites were reduced after their slurry covering. These coating methods were responsible the low catalyst activity for mentioned more viscous coats.

The largest CO-conversion drop was also found for CuXY-2 between 200 °C and 350 °C in compare with CuXY-1. The layer thickness increased with higher

viscosity of the catalyst slurry. The uneven catalyst surface was formed on to the channel walls after calcination. Moreover it was may be blocked partially the gas flow and led to layer looses. Therefore, CuXY-1 attained the second lowest activity, which was not sufficient to drive the CO-conversion higher than 50 % at 300 °C.

Pt/CeO₂-catalyst was seemed to be very active at the higher reaction temperature range between 350 °C and 400 °C in contrast to other catalysts. Pt/CeO₂ catalyst achieved the lowest CO-conversion of 30 % at 400 °C. It should be noted that catalyst preparation method allows for a different dispersion of the active agent. The metal dispersion resulting after Pt/CeO₂-preparation was not sufficient because only the small amount of platinum was deposited on the support reached 1 wt.%.

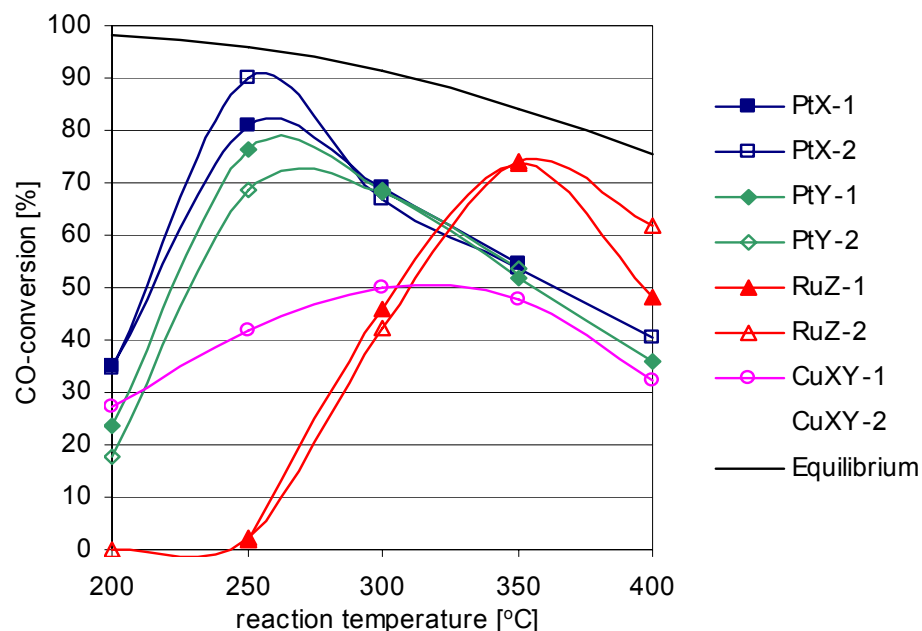


Figure 34 CO-conversion at 558 ms residence time and 2.1 H₂O/CO-ratio over the industrial catalysts as a function of reaction temperature [°C]; HTS-inputgas: CO=8 vol.%, CO₂=12 vol.%, H₂=23 vol.%, N₂=30.6 vol.%, H₂O=17 vol.%.

An addition a solution of H_2PtCl_6 to the CeO_2 -support as a slurry led to the formation of large crystallites whose size was depended on the deposited amount of platinum and which do not enable a surface proportional to the platinum concentration. Additional, the unexpected elementary of iron could also influenced on the catalyst activity reduction.

The promoting effect of water on catalyst was explained as oxidation of the metal oxide support by water. The water in hydroxide form plays an important role as a good oxidant in WGS reaction. The activity of catalyst depends both on the texture and the kind of support.

A surface formate mechanism is one mechanism proposed for WGSR, wherein the generation of active site bridging OH groups was included with the removal of H_2 during water-supported surface formate decomposition. Both water and metal type/loading on ceria support were considered to enable formate decomposition and enhanced CO-decomposition to CO_2 and H_2 production rate [101, 102]. The increased catalysts activity for WGSR was found also by Wheeler et al. [94] due to rather H_2O adsorption on ceria than on metal surface saturated with CO with the copper– ceria catalyst. Moreover the reaction rate between adsorbed CO on the metal and O on ceria was increased by the effect of ceria [99]. It was also suggested, that metal was involved in the formate decomposition. The decomposition rate was 20 times faster for Pt/ceria than with Au/ceria. The metal catalyzes the surface reduction and it was needed for bridging OH on the ceria surface, which were used as the active sites [100].

The steam excess was used to drive this reaction to equilibrium constant to achieve the visible higher CO-conversion. It was talked into consideration, that an elevated temperature of WGS reaction is thermodynamically unfavourable. Fig. 36-38 present the influence of the H_2O/CO -ratio on the CO-conversion at different reaction temperature, constant residence time and different reactant gas concentration. The dependence of catalyst activity on water vapor concentration was tested by increasing the steam to carbon monoxide ratio in the feed 1.3 to 3.7 for HTS and 7.5 to 13.3 for LTS. The CO-conversion increased

with rise in the water to carbon monoxide ratio for all catalysts in both forms (milled/ unmilled). The PtY-2 catalyst achieved the highest CO-conversion of 83 % for the lower H_2O/CO -ratio of 3.0 at 300 °C (Fig. 34). For another reaction conditions the CO-conversion is almost the same for both forms. No significantly differences in HTS reaction activity were observed also between two catalyst forms for PtX-1,2 at temperature 300 °C-400 °C with H_2O/CO -ratio increase (Fig. 36). This catalyst achieved the second highest CO-conversion of 82 % for H_2O/CO -ratio of 3.7 at 300 °C. At these reaction conditions the PtX-1,2-catalysts were achieved maximum CH_4 composition of 1.2 vol.% and 0.7 vol.%.

CuXY-2 showed a worse conversion only for 2.1 H_2O/CO - ratio in compare to its unmilled form but the same highest CO-conversion of 69 % for both CuXY-1, 2-catalysts for the highest ratio (Fig. 37).

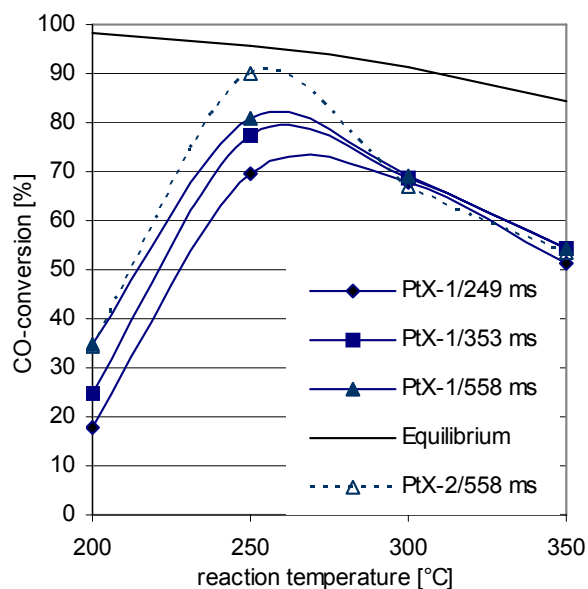


Figure 35 CO-conversion at different residence time as a function of reaction temperature [°C] over PtX-1-2; HTS-input gas: $CO=8$ vol.%, $CO_2=12$ vol.%, $H_2=23$ vol.%, $N_2=30.6$ vol.%, $H_2O=17$ vol.%.

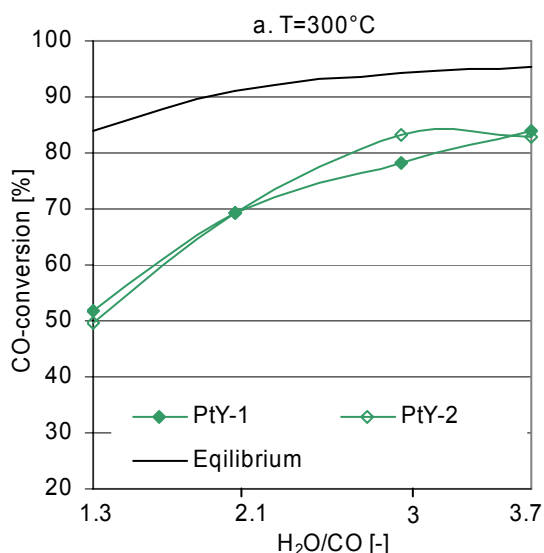


Figure 36 CO-conversion at 353 ms, different temperature and H₂O/CO-ratio over the PtY-1-2 catalysts (300 °C); HTS-input gas: CO =8 vol.%, CO₂=12 vol.%, H₂=23 vol.%, H₂O =17-47 vol.%, N₂=31-10 vol.%.

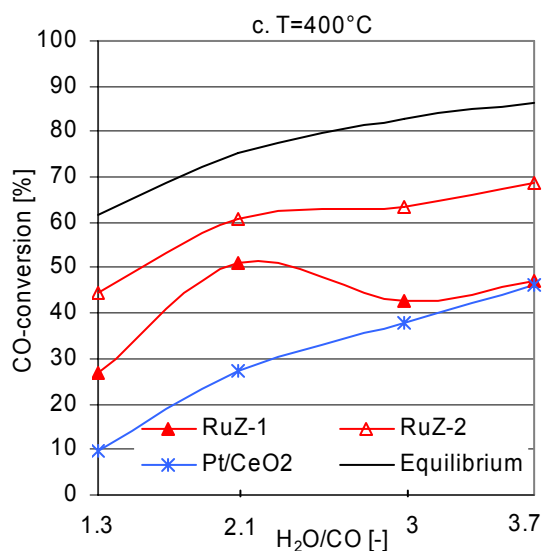


Figure 38 CO-conversion at 353 ms, different temperature and H₂O/CO-ratio over the RuZ-1-2 and Pt/CeO₂ catalysts (400°C); HTS-inputgas: CO=8 vol.%, CO₂=12 vol.%, H₂=23 vol.%, H₂O=17-47 vol.%, N₂=31-10 vol.%.

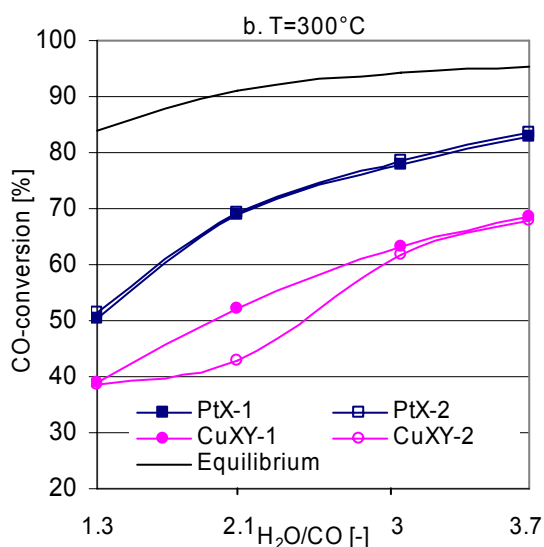


Figure 37 CO-conversion at 353 ms, different temperature and H₂O/CO-ratio over the PtX-1-2 and CuXY-1-2 catalysts (300 °C); HTS-input gas: CO =8 vol.%, CO₂=12 vol.%, H₂=23 vol.%, H₂O =17-47 vol.%, N₂=31-10 vol.%.

PtY and RuZ catalysts show a higher activity in the milled form. At the highest operating temperature of 400 °C, the milled form of RuZ-2 achieves the higher CO-conversion of 69 % and 3.7 H₂O/CO-ratio (Fig. 38), which was correlated exactly with the methanation. It showed the elevated methane content with its maximum 4 vol.% after powder milling for 2.1 H₂O/CO-ratio and 3 vol.% for its untreated powder. The methanation decreased for RuZ-2 with increase of steam to carbon monoxide ratio higher than 2.1 at 400 °C. In contrast to the RuZ-2, the RuZ-1 achieved the higher CO-conversion of 50 % at 2.1 H₂O/CO-ratio. In these reaction conditions the maximum of methane production was obtained.

All presented catalysts in this work demonstrated lower activity results for LTS reaction conditions in compare to HTS. The most catalysts presented the best activity for the highest H₂O/CO-ratio with the maximum CO-conversion at 250 °C. The PtX proved again the best activity not only for HTS but also for LTS reaction (Fig 39). Just for this catalyst the milling process seems to have a positive influence, which was expressed in its maximum CO-conversion of 69 % at 250 °C. Almost the

same high CO-conversion (67 %) was observed at 200 °C, which is mean that this milled catalysts could be operate at lower reaction temperature and exhibited still the highest reaction efficiency.

Although other catalysts performed better in the untreated form, only PtY-1 achieved the CO-conversion more than 50 % for the highest water concentration. However differences in the water content had no influence on their activity in temperature range of 200-250 °C, a performance increase was observed only at 300 °C and 7.5 H₂O/CO-ratio for the RuZ-1, 2 and Pt/CeO₂-catalysts, which were attained their maximum CO-conversion subsequently 46 % and 10 % (Fig. 40).

High conversion at lower temperatures was explained in literature as higher loading of noble metals and their better dispersion of active spaces on the catalyst surface with smaller particle sizes [71]. It was found, that the catalytic activity in WGSR depended on the nature of the metallic and the metal oxide support. Moreover platinum catalysts were generally more active than other noble catalysts and achieved higher activity with reducible support such as CeO₂ rather than on irreducible oxides like Al₂O₃. Additional, activity of Pt/CeO₂ was not depended on the structural characteristic of the support. Only the support nature was contributed to the active energy for the catalysts. No influences of metal loading, dispersion and crystallite size was observed on reaction rate for all metal supports [103].

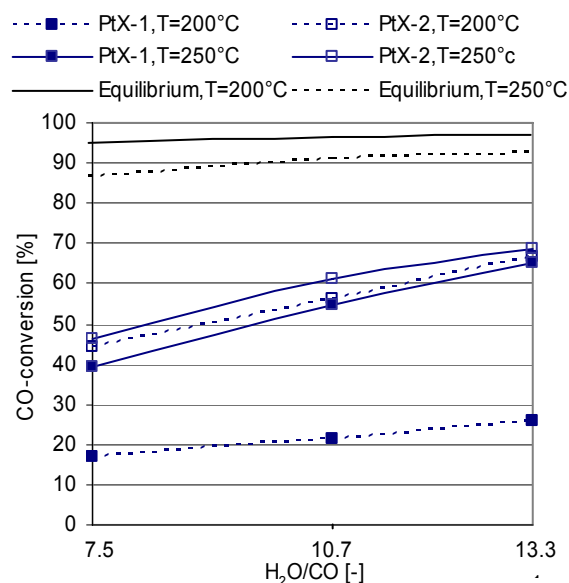


Figure 39 CO-conversion at different temperature and 353 ms residence time as a function of the H₂O/CO-ratio for the PtX-1-2-catalysts; LTS inputgas: CO=2 vol.%, CO₂=18 vol.%, H₂=31 vol.%; H₂O=27-42 vol.%, N₂=21-0.4 vol.%.

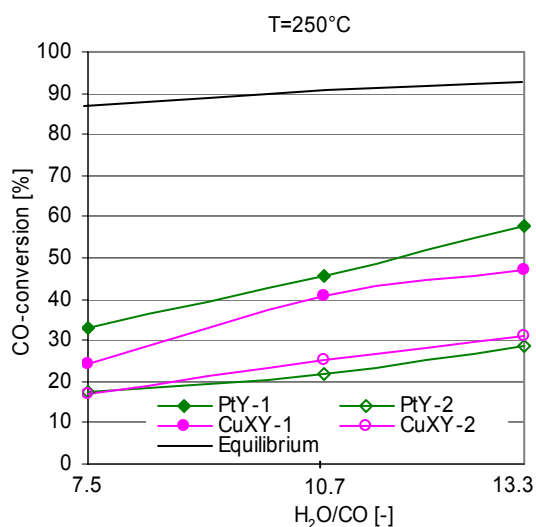


Figure 40 CO-conversion at 353 ms residence time and 250°C as a function of H₂O/CO-ratio for the PtY-CuXY-1-2-catalysts; LTS-inputgas: CO=2 vol.%, CO₂=18 vol.%, H₂=31 vol.%; H₂O=27-42 vol.%, N₂=21-0.4 vol.%.

5 HYDROGEN PURIFICATION USING MICROSTRUCTURES

PART I: PREPARATION OF Al_2O_3 AND CeO_2 WASHCOATS IN MICROCHANNELS ^[116]

5.1 EXPERIMENTAL

5.1.1 EXPERIMENTAL SET-UP

The catalyst coating was applied to micro-structured foils (50 mm x 50 mm x 1 mm), containing 49 channels: 400 μm deep and 600 μm wide. Each coated foil was stacked with filler plates inside a stainless-steel housing. Micro-reactor and foils were made of stainless steel (DIN 1.4571).

The adherence of the Al_2O_3 and CeO_2 layers has been determined according to a method described in the literature [26, 110]. The coated micro-channel platelets were immersed in petroleum ether inside a sealed beaker, and then treated in an ultrasound bath for 1-40 min. The weight loss caused by the exposure to ultrasounds was calculated based on the weight measurements of the coated plates before and after the vibration. The thermal shock was carried out by heating the coated foils to 450 °C, and cooling quickly to room temperature. This thermal shock process was repeated ten times for each sample, after which the weight loss was measured.

5.1.2 CATALYST PREPARATION (SUSPENSION)

The gamma alumina (Alfa Aesar) and CeO_2 (Sigma-Aldrich), with a mean size of 20 nm ($180 \text{ m}^2/\text{g}$) and

smaller than 25 nm, respectively, were used as the main materials. Polyvinyl alcohols (PVAs from Sigma-Aldrich) with three different molecular weights such as 13000-23000 g/mol (PVA_1), 31000-50000 g/mol (PVA_2) and 124000-186000 g/mol (PVA_3) were used as binders. Their viscosities measured by the distributor were given as 4% of PVA in water and were as follows: 3.5 – 4.5 cP, 5.4 – 6.5 cP and 55 – 65 cP, respectively. The stability of the slurries was studied with the aim of gathering zeta-potential measurements. Small samples from slurries were diluted in an aqueous solution of 10 mM KCl. The pH adjustment was followed by either HCl or NaOH 1M, 0.1M and 0.01M. The samples of the solution were injected in the electrophoresis cell and the two measurements of zeta-potential and particle sizes were obtained.

The same solid content was prepared for the procedure of the micro-channel platelets coating with the suspensions. The binder weight was chosen based on the results of the smallest Al_2O_3 and CeO_2 particle sizes presented in Table 3. The literature demonstrated that the highest adhesion of the powder used as a catalyst carrier and coated on microstructures belong to the smallest particles [49]. Firstly, the each of three PVAs were dissolved in water at 60 °C with the concentration of 16% of PVA_1 , 16% of PVA_2 and 1.6% of PVA_3 for three samples of the Al_2O_3 suspension. The aqueous CeO_2 suspension samples were made of the same PVAs but with different concentrations such as 20%, 15% and 5% for the PVA_1 , PVA_2 and PVA_3 , respectively. The 20 % of powders were added to each of six suspension samples and stirred overnight. The addition of Na_2SO_4 (20 mM) replaced the KCl to dilute the thicker suspension in order to avoid the corrosion effect. The cationic or anionic surfactant such as

certimonium bromide (CETAB, 20 mM) and sodium dodecyl sulfate (SDS, 80 mM) 1:10 were then dropped in to the Al₂O₃ or CeO₂ suspensions, respectively. The surfactants were used to receive the lower surface tension of suspension and avoid the layer splitting after coating and during the reaction tests. The HNO₃ and NaOH were used for pH adjustment. The HNO₃ was found to be more effective than HCl, too high a concentration of which also caused the corrosion effect and catalyst losses from the metallic plates.

5.1.3 COATING OF THE PLATES **(SPIN COATING)**

The micro-structured substrates were first cleaned in an ultrasonic bath with 2-propanol, then dried and heated in air at 900 °C for 3 h (Fig. 41). After the positioning and masking of the substrates, the prepared slurry was deposited into the micro-structured channels. The micro-channels were filled completely with a syringe and surplus slurry outside the channels was removed by a stainless-steel knife with a flat edge. After coating, the plates were put into a spin coater. The surplus slurry inside the channels was removed due to the rotation of the plate. The spin coater was programmed in two steps with speeds of 500 rpm for 5 s and then 1000 rpm for 10 s. The coats were then calcined in hot air at a temperature and time determined by TGA analysis (Table 4). The amount of catalyst applied with each plate was then measured by weighing.

5.1.4 CHARACTERIZATION OF **COATED LAYERS**

5.1.4.1 SCANNING ELECTRON **MICROSCOPY (SEM; EDX)**

The catalyst samples were analyzed using a Zeiss Ultra 55 scanning electron microscope (SEM) equipped with an EDAX Phoenix energy dispersive X-ray spectroscopy (EDXS) unit.

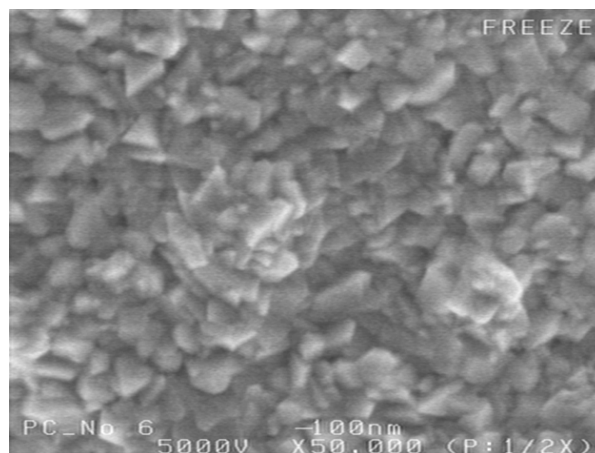


Figure 41 SEM picture of microchannel stainless plate after calcination at 900 °C for 3 h.

5.1.4.2 PARTICLE ANALYSIS

The CILAS 1180 used a laser diffraction and CCD camera which allowed, in one single range, the measuring of powder particles between 0.04 and 2,500 μm in a wet dispersion mode. The fine particles were measured by the diffraction pattern, using the Fraunhofer and Mie theory. The coarse particle analysis was performed by a real-time Fast Fourier Transform of the image, which was obtained with a CCD camera equipped with a digital processing unit (DSP).

5.1.4.3 THERMO-GRAVIMETRIC **ANALYSIS (TGA)**

The STA 449C Jupiter® (NETZSCH-Gerätebau GmbH) method is based on an ultra-microbalance from Sartorius and was used for simultaneous thermal analysis of the dried suspension samples to determine the change in sample mass and calcination

temperature. The samples were heated in temperatures ranging from -120°C to 600°C under air flow. Then the parameters such as temperature and the time was chosen under which the sample mass was stable. After that, the calcination parameters were calculated and the second analysis was performed under the constant temperature of 500 °C. This lower temperature was chosen in order to avoid the deterioration of the high surface area of the coat. The new sample was heated until the constant mass weight was reached. The time and the temperature of the burnout of the suspension's additives were taken as the calcination parameters for the support.

5.1.4.4 MERCURY POROSIMETRY

The small fragments of the calcined suspension were analysed in the mercury porosimeter. The apparatus consisted of two parts – Pascal 140 and Pascal 240 – where under the pressure of 0.013-0.4 MPa and 0.1-200 MPa the pore-size areas of 58000-1900 nm and 7500-3.7 nm resulted. The Washburn equation was universally used to calculate pore size distribution. The most frequent contact angle of mercury was found between 130° and 150°.

5.1.4.5 ZETA POTENTIAL

The Zeta-potential analysis was made in the Brookhaven ZetaPlus analyser. This measurement covered the potential range of $\pm 6 - 100$ mV, which corresponds to mobilities of $\pm 0.5-8 \times 10^{-8} \text{ m}^2/\text{V}\cdot\text{s}$. The sample materials (nm particles) were scattered by incoming laser light. Due to the random Brownian motion of the particles, the scattered light intensity fluctuated over time. The equivalent spherical particle sizes were calculated using the Stokes-Einstein equation. Molecular weights can also be calculated from the scattered intensities measured at different concentrations. The particle sizes, their distribution and the electrostatic repulsion of colloidal particles were the

key to understanding the stability of the dispersion in this paper. A simple measurement of the electrophoretic mobility and yields give valuable information for the optimization of coated suspension.

5.2 RESULTS AND DISCUSSION

5.2.1 PARTICLE SIZE AND MORFOLOGY

Particle size analysis of the as-received powders of Al_2O_3 and CeO_2 prepared as wet dispersion mode is presented in Fig. 42. The results showed that the diameter of ~90% dispersed particles for Al_2O_3 and CeO_2 were smaller than 21.1 and 10.23 μm , and ~5% particles had the diameter of 0.31 μm and 0.19 μm respectively. The particle diameters were mainly 0.04-0.4 μm (one peak) and 1-35 μm (1-8, 8-35 μm of two peaks) for Al_2O_3 powder. Compared with the Al_2O_3 powder, the CeO_2 particles were smaller and indicated a characteristic diameter of 0.01-0.5 μm (one peak) and 0.6-18 μm (0.6-7 μm , 7-18 μm of two peaks), respectively. However, the Al_2O_3 as-received powder showed the narrower particle size distribution of the two separated peaks.

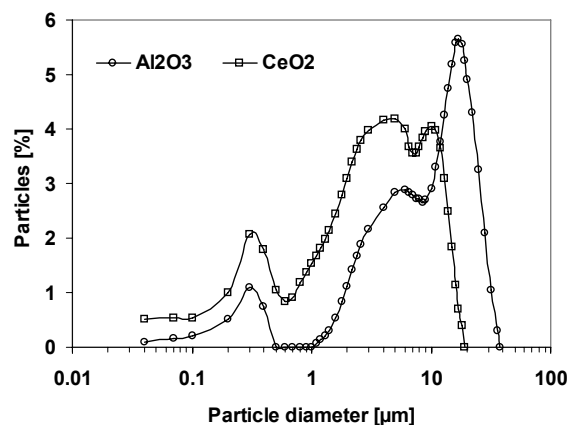


Figure 42 Particle size distribution of the Al_2O_3 -and CeO_2 powders.

Fig. 43 and 44 show the morphology of the Al_2O_3 and CeO_2 as-received dry powders achieved by a scanning electron microscope analysis (SEM). The γ -alumina powder consisted of the primary particle sized at 37-85 nm, so the surface structure was compact due to its narrow particle-size distribution (Fig. 43a). On the higher picture magnification, it was easy to notice that the Al_2O_3 powder assumed flake forms (Fig. 43b). The larger agglomerates in the range of 250 nm were made of smaller primary particles with a diameter of approximately 25 nm.

Fig. 44a indicated that the ceria powder exhibited a greater variety of particle sizes than alumina, which was confirmed by the SEM results in Fig. 43. The small aggregates in the sizes between 38 and 85 nm built the bigger submicron particles of 339 nm. This specificity of size variations influenced the unevenness of the powder surface and the lower solid packing in comparison to alumina. The smallest primary particles of 13 nm were founded in higher SEM-picture magnifications (Fig. 44b).

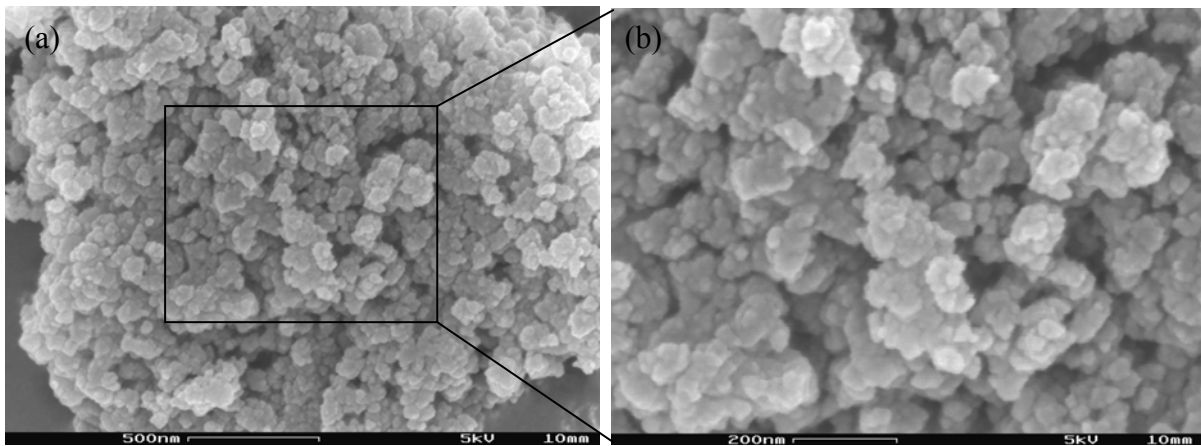


Figure 43 SEM pictures of Al_2O_3 - powder. (a) Low magnification. (b) High magnification.

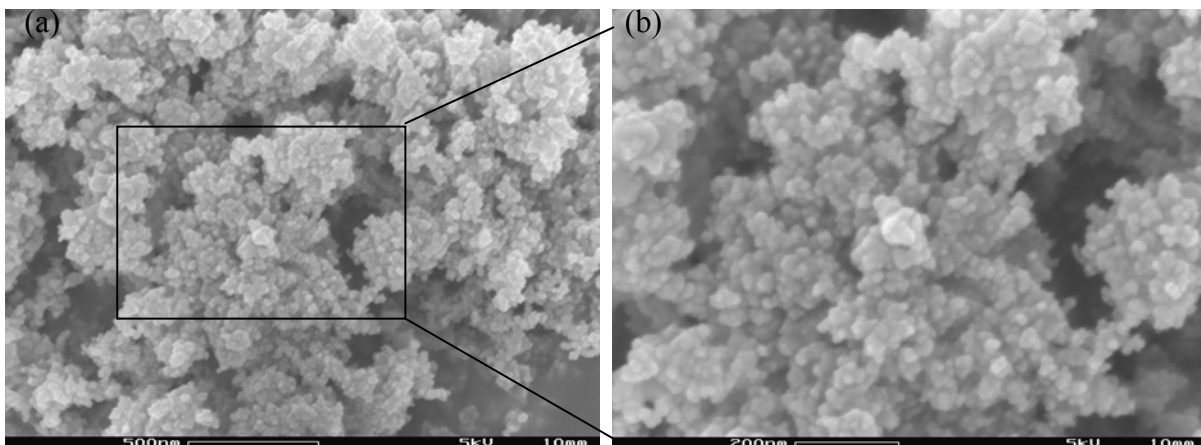


Figure 44 SEM pictures of CeO_2 - powder. (a) Low magnification. (b) High magnification.

5.2.2 CHARACTERIZATION OF SUSPENSIONS

5.2.2.1 ZETA POTENTIAL

The homogenization of the powders in a liquid medium was necessary to produce the sufficiently-packed and well-adhered coats which were used as the catalyst support. The suspension preparation should be provided as follows: 1) wetting of the external particles, 2) breaking-down of the clusters and agglomerates into primary units, 3) dispersion of primary particles in the liquid medium, and 4) prevention of reagglomeration through a stabilization mechanism [111]. The suspensions were stable when the repulsion forces of the dispersed particles sufficed for the flocculation prevention. The charge interactions between particles could be described by the zeta potential. The results from zeta-potential measurements allowed the controlling of the dispersion process, especially the rising agglomerates, which influenced the defects' appearance in the support layer.

Fig. 45 illustrates the zeta potential of CeO_2 and Al_2O_3 suspensions as a function of pH. For this type of measurement, the powder particles were suspended in 10mM KCL, since they didn't adsorb on specific surface sites of suspended powders. After that the pH was adjusted with HCl and NaOH solutions. The effect of pH on the zeta potential was significant for both Al_2O_3 and CeO_2 powders. The zeta potential of alumina was increased from 0 mV (isoelectric point) at pH=8 to 38 mV at pH = 2. The CeO_2 powder showed elevated stability with an increase in pH. The isoelectric point was found at pH 3.5 and the highest particle dispersion of -22mV at pH 8. pH 8 and 4 were chosen for CeO_2 and Al_2O_3 suspension optimization in the next steps of this experimental work.

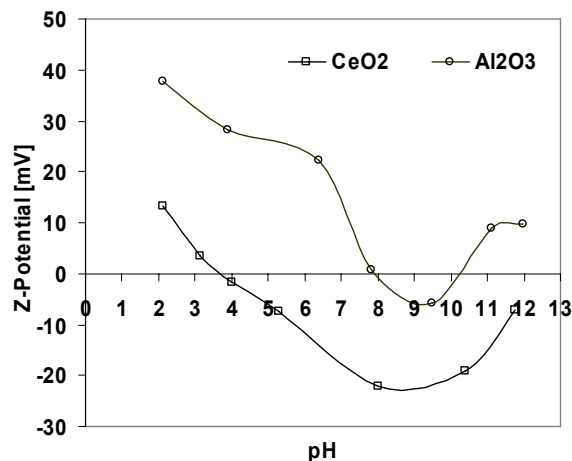


Figure 45 Zeta potential as a function of pH for CeO_2 - and Al_2O_3 -powders.

5.2.2.2 EFFECT OF SURFACTANT AND PVA ADDITION

Before the suspension preparation, the particle diameters were measured in natural pH and without any addition of binder. The differences of particle diameters between the two powders were significant in this surrounding environment. The dependence of effective particle size on the surfactant/suspension weight-ratio and flocculation level is described in Table 9. The important influence of surfactant concentration on the particle diameter changes was observed for the CeO_2 . The agglomerates diminished when the surfactant weight was extended. The maximum agglomerate size of 694.1 μm was measured for the surfactant/suspension weight-ratio of 20:1. However, only a small additional amount of surfactant in the suspension with a ratio of 0.1 was sufficient for achieving the smallest particle diameter in the range of 8.7 nm.

The poly-vinyl alcohol (PVA) was chosen as a binder to improve adhesion between the layers and the substrate metal made of stainless steel during the drying and calcination procedure and also to achieve crack-free catalyst layers. The PVA addition caused the prevention of layer shrinking at the initial

stage of drying already. The influence of PVA molecular weight, the concentration at a stable pH value (3 for Al₂O₃ and 8 for CeO₂) versus the effective particle diameter is shown in Table 10. The highest dispersion of solid medium was observed for the CeO₂ suspension with a PVA molecular weight of 18000 and a concentration of 20 wt. % in H₂O. For the Al₂O₃ dispersed powders in suspension, the two comparable smallest particles were achieved after the addition of PVA with a molecular weight of 18000 g/mol and 405000 g/mol and the concentration of 10 wt. % in H₂O. The largest agglomerates in the range of 117-166 μm appeared in the CeO₂ suspension after the addition of the highest PVA molecular weight of 155000 g/mol.

5.2.2.3 THERMO-GRAVIMETRIC ANALYSIS (TGA)

The thermo-gravimetric analysis was carried out to improve the decomposition of the binder at a constant temperature of 500 °C. The dried suspension samples were heated from room temperature to 500 °C at a rate of 5 °C/min and left until the binder burned out.

The binder decomposition for a CeO₂ sample was accomplished before the calcination temperature of 500 °C was reached. However, the PVA weight in the analysed sample was higher than for the alumina fragments; the PVA decomposition occurred more rapidly. The weight loss of the Al₂O₃ samples was completed in the time range of 4 and 9 h at 500 °C. The calcination temperatures were approved for both Al₂O₃ and CeO₂ suspensions from the results of the TGA analysis since the time of PVA decomposition was known (Table 11).

Table 9 Influence of surfactant addition in to the suspension containing 8 wt.% of PVA (Mw=18000g/mol) on effective particle diameter of the Al₂O₃ and CeO₂

Support	Surfactant/ susp.	pH [-]	d _{ef} [nm]
CeO ₂	No	6	345*
	surfactant		
	0.1	8	8.7
	10	8	348
Al ₂ O ₃	20	8	694
	No	6	n.d.**
	surfactant		
	0.1	3	42

*) No pH adjusting and no binder addition,

***) particle diameter > 30 μm

Table 10 Influence of polymers on the effective particle diameter

Mw _(PVA) [g/mol]	PVA _(H2O) [wt.%]	d _{ef} [nm]	
		Al ₂ O ₃ , pH=3	CeO ₂ , pH=8
13000	10	27.2	29.1
	15	N.M.	23.2
	20	42	8.7
31000	10	28	21
	15	N.M.	13.2
	20	82.4	21.9
124000	0.5	15.4	166.2
	2	34.9	148.6
	5	51.4	117.2

Table 11 Calcination parameters for Al₂O₃ and CeO₂; T_{calc}=500°C

Support material	Mw [g/mol]	t _{calc}
Al ₂ O ₃	13000	8,5 h
	31000	4,5 h
	124000	9 h 10 min
CeO ₂	13000	1h
	31000	1h
	124000	1h

5.2.3 CHARACTERIZATION OF LAYERS

5.2.3.1 EFFECT OF DRYING ON

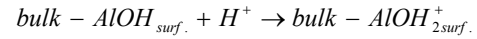
Al₂O₃ LAYER

Figures 46a and 46b represented the SEM micrographs of Al₂O₃ layers, which were dried first in air at room temperature and then on a hot plate at 60 °C. A fine mesh of small cracks appeared on the layer surface during the liquid evaporation from the spin coated layer at room temperature (Fig. 46a).

When the pH value was increased from 2 to 3.5, the particle attractions following the clusters formation started until the liquid medium was completely evaporated from the coating. However, when the coating was dried on the hot plate, only some breakage around the bigger grains and on the channel edges could be seen (Fig. 46b). The EDX analysis proved that those grains were the metallic fragments of supported foils. In this case, the top surface has to be mechanically polished before the coating-procedure treatment to remove the residue of the plate from the channel surfaces, which were also not removable during vibration in an ultrasound bath filled with 2-propanol. The drying of coated foil on the hot plate stopped the particle migration and agglomeration. Also the layer thickness was crucial for gaining a uniform layer surface. Therefore the two opposite channel edges showed no bigger clusters due to the faster drying of the thinner layer comparing the channel bottom. For this reason the time of drying and layer thickness were important parameters in avoiding the cracks forming and the delamination of the Al₂O₃ layer. The two drying methods were performed for the Al₂O₃ coating and compared to find what was causing the layer deterioration.

After HNO₃ adjusting, the pH value increased from 2 to 3.5 in about two days. The solution then slowly approached the final pH of about 4 when acid (HNO₃) consumption was stopped, thus reaching a stable pH. The same plateau was reported in the

literature for alumina suspensions [112-114]. The processes such as surface charging and dissolution could precede the acid consumption by alumina powder. For these processes the following two reactions (eq. 61, 62) were recommended [113, 114]:

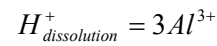


Equation 61



Equation 62

The acid consumption as a result of dissolution (H⁺_{dissolution}) could be equal the amount of Al³⁺ formed during aging [13, 48]:



Equation 63

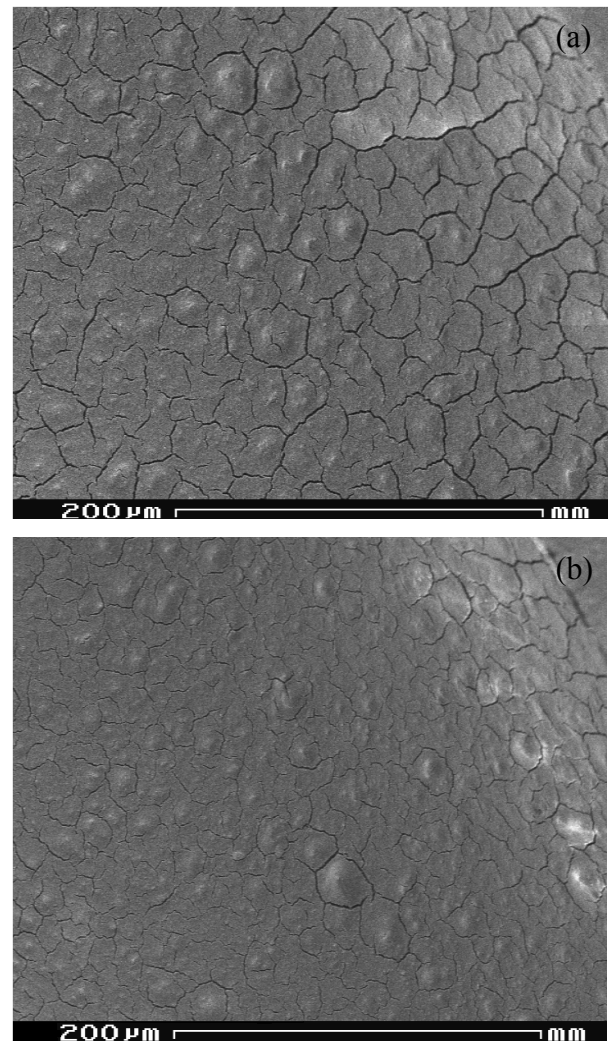


Figure 46 SEM micrographs of Al₂O₃-layers dried in air (a) and on hot plate (b).

For the acid consumption due to surface charging, (H^+ surface charging) could be calculated by the following reaction:

$$H^+_{\text{surface charging}} = H^+_{\text{initial}} - H^+_{\text{dissolution}} - H^+_{\text{final}} \quad \text{Equation 64}$$

where H^+_{initial} is the initial amount of acid in the suspension and H^+_{final} is estimated by the final pH.

It was found in the literature that surface charging was faster than dissolution, when the small amount of acid was added. Then the protons were quickly adsorbed on the surface, but after some time the rate of this reaction decreased and the surface charging increased. When more acid was added, the charging and the dissolution appeared simultaneously [113, 114]. The literature reported that the surface charging was needed for the

dispersion of the large powder aggregates to form a continuous particle network [115].

5.2.3.2 EFFECT OF SOLID CONTENT VARIATIONS ON LAYER FORMATION

The relations of the solid content in the slurry on the catalyst support uniformity are shown in Fig. 47. The results show that the solid content in the slurry greatly affects the layer loading and uniformity. The more solid content in the slurry, the more loading of coating and the larger the defects such as cracks were shaped in the layer (Figs. 47a and 47c). For this reason the solid concentration was decreased until the highest layer uniformity was achieved.

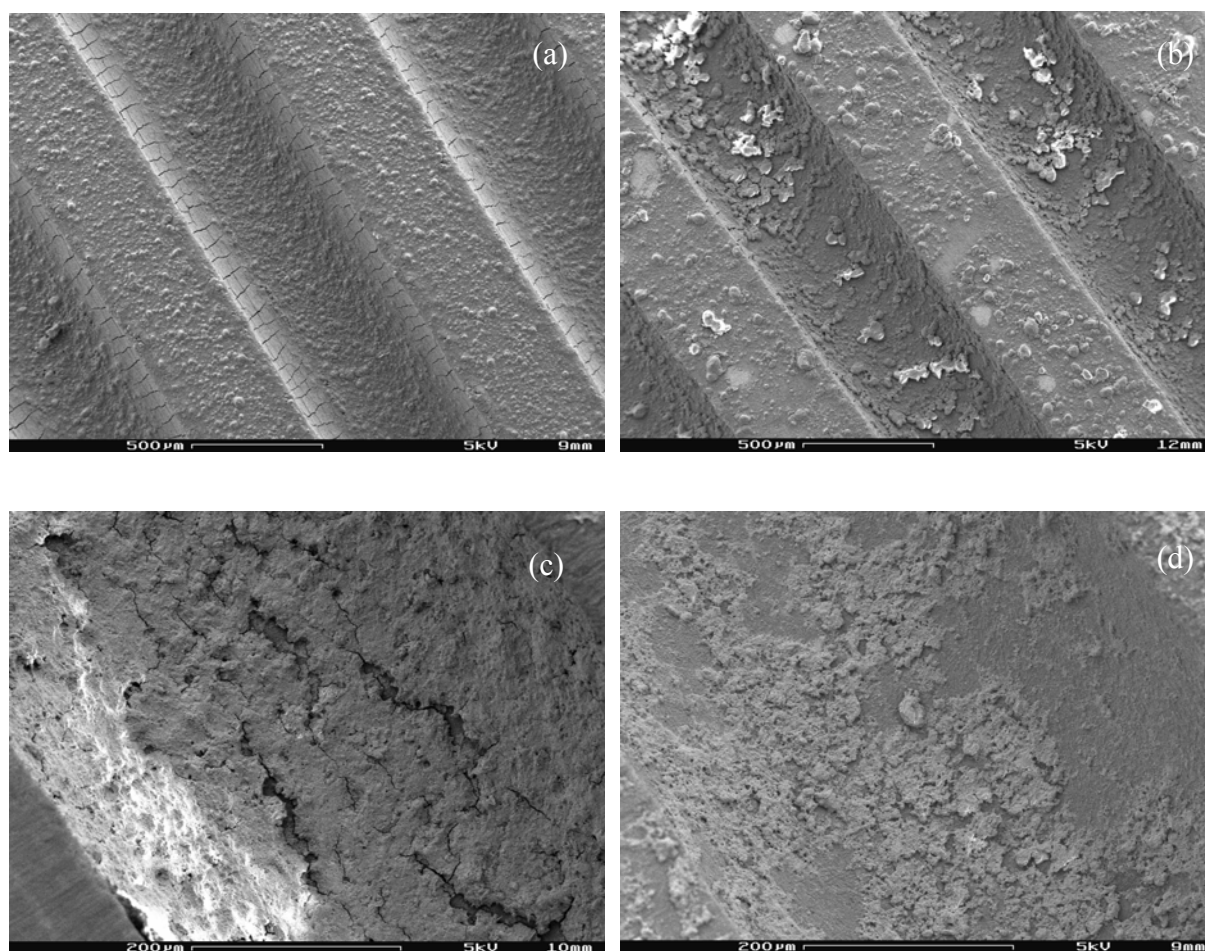


Figure 47 SEM micrographs of layers for different solid content: Al_2O_3 – 16/32 (a), 18/36 (b), CeO_2 - 30/30 (c), 20/20 (d) containing PVA (Mw of 31000 g/mol).

For the alumina coating the cracks were found on the opposite channel walls after the suspension coating with the initial powder content of 40 wt.%. In these regions the layer structure was very dense and sintered. However the very porous and homogeneous surface was presented on the middle channel. The lower suspension volume deposition with 32 wt.% Al_2O_3 powder caused the very porous coating to cover the entire channel. For the CeO_2 layer, no optimal layer quality was performed with a suspension coating with 30 wt.% solid content or with 20 wt. % suspended powder. Even after the thinner suspension coating, the uniform channel covering was not achieved. It was noted that the layer shrinkage during liquid evaporation by heating caused particle creeping and the appearance of holes in the coating on the channel bottom (Fig. 47c). The very dilute suspension still had no positive influence to completely cover the channels and only a rather heterogeneous layer was formed (Fig. 47d). The layer optimization was evaluated in the next part of this study.

5.2.3.3 EFFECT OF CALCINATION TEMPERATURE FOR THE Al_2O_3 LAYER

After the Al_2O_3 spin-coating method and drying, the treatment of the samples by heating in air at a different temperature was very substantial. Calcination improved the cohesion of the coat on the metallic substrate. Calcining the coating was also favourable for removing the organic additives which were only useful during the process of the particle dispersion and deposition.

Figs. 48a and 48b show the Al_2O_3 (PVA_2) layers after calcination at two different heating temperatures such as 700 °C and 500 °C for 2 h. After calcination at 700 °C, the alumina surface layer was more heterogeneously distributed. The large microparticles in the range of 10-111 μm were formed due to sintering of the smaller submicro- and

nanoparticles. However the layer strongly adhered in the entire channel. The fine particles and small grains coalesced to form a dense structure without any cracks. The layer surface was still porous and very rough.

The lower temperature calcination of the alumina layer affected the higher uniformity, which is shown in Fig. 48b. Only some larger particles at a size of down to 44 μm stuck out of the homogeneous coating, but no cracks or layer splitting from channel walls were detected. The layer was well-adhered to the metallic foil.

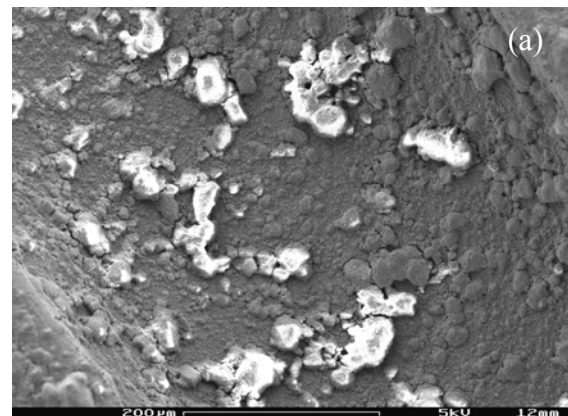


Figure 48 SEM micrographs of calcined alumina (Al_2) coating at 700 °C (a) and 500 °C (b) for 2h.

In order to evaluate the effect of heat treatment on the layer adhesion, the mass losses of coats was determined after each adhesion test of the thermal shocks ($n=10$) and ultrasonic vibration. It resulted that the coating calcined at 700 °C showed no mass losses after either adhesion test. However the second sample – heated at 500 °C for 2 h – was

stable after the fourth thermal shock and lost only 5.7 wt.% of mass; no layer losses were found after ultraconication. In this case the lower calcination temperature of 500 °C was chosen due to the higher surface area of the layer compared to the same layer calcined at 700 °C [24].

5.2.3.4 POROSIMETRY (PORE DIAMETER)

The Al₂O₃ and CeO₂ suspensions containing PVAs were poured into the glass beaker to a height of about five millimetres. The dried slurries were calcined at 500 °C in an oven for the time given in the TGA analysis (Table 12). The Al₂O₃ and CeO₂ as received powders were first dried at 500 °C for 1 h. These prepared fragments were analysed in the mercury porosimeter. The results of suspension porosity measurements are given in Table 12.

The cumulative volume plot of the mercury porosimetry data is shown in Fig. 49. It can be seen that the macroporosity of the Al₂O₃ (PVA₁) sample starts up to 100 µm of pore radius, whereas the other samples, including Al₂O₃ and CeO₂ as-

received powders (Fig. 49b), showed the presence of macropores up to 10 µm. The use of PVA with the 13000 g/mol molecular weight was affected on the lowest bulk density of the Al₂O₃ coat. However, a bulk density of more than four times the size was found for the Al₂O₃ (PVA₁) sample compared to the as-received powder sample and six times higher for the CeO₂ (PVA₃) coat fragment.

5.2.3.5 EFFECT OF FREQUENCIES OF COATING ON METAL LOADING

The relation of the loading of coating and the number of coating cycles is shown in Fig. 50. Each support weight gain increased linearly with the number of coating cycles. The optimization of the CeO₂ suspension with PVA (124000 g/mol) was excluded in the next steps of this experimental work due to its fast flocculation, which prevented stable coating from being established.

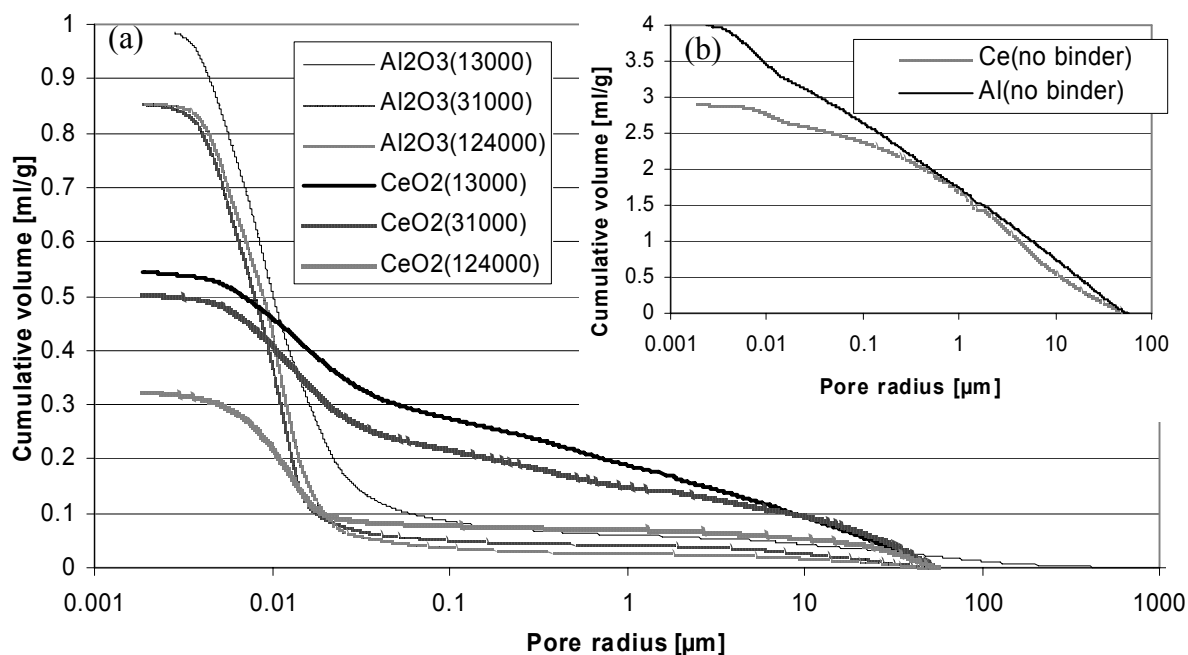


Figure 49 Mercury porosimetry. Cumulative volume plot for different samples.

Table 12 Mercury porosimeter analysis of the different suspensions

Washcoat	Al ₂ O ₃			CeO ₂			Al ₂ O ₃ *	CeO ₂ *
Sample	Al1	Al2	Al3	Ce1	Ce2	Ce3	-	-
M _w (PVA) (g/mol)	13000	31000	124000	13000	31000	124000	-	-
Total SA (m ² /g)	213.32	216.40	200.69	47.63	51.50	54.21	267.21	86.60
Total porosity (%)	79.77	72.70	74.79	71.29	71.23	59.58	90.43	91.69
Bulk density (g/cm ³)	0.81	0.85	0.87	1.31	1.42	1.85	0.23	0.32
Apparent Density (g/cm ³)	4.01	3.12	3.46	4.57	4.94	4.58	2.37	3.79

*) 500°C,1h

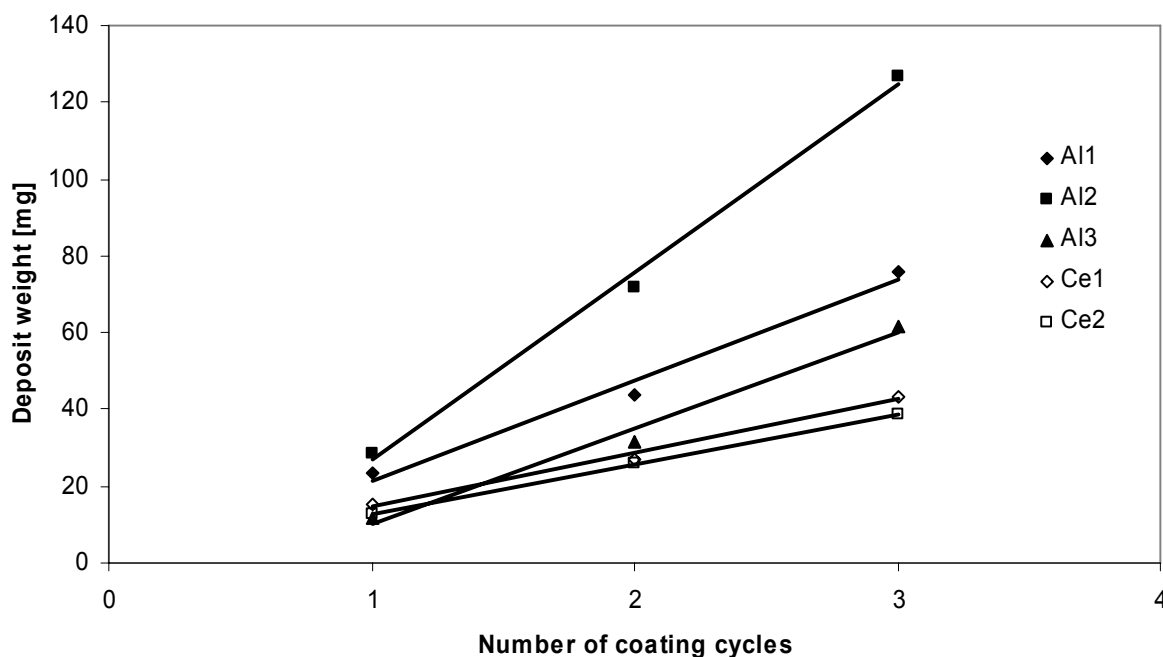


Figure 50 The Al₂O₃-and CeO₂-catalyst coating into microchannels as a function of coating cycles.

The fundamental reason for the large coating variation was the exact controlling with the layer volume injection in proving their uniformity, adhesion and long stability on the metallic micro-channel plates during real reaction conditions. However it should be considered that the tensile stress of the layer provoked the cracking and delamination when its critical thickness value was

exceed [53]. The spin-coating method was used in this experimental work to avoid the higher accumulation of suspension volume, which caused cracks on the channel bottom, and to receive a porous basis to enhance the catalyst dispersion of solution used for impregnation. This also achieved an efficient utility of catalyst with its small weight.

The average weight of the CeO₂ supports deposited per coating cycle was about 15 mg/cycle and 13 mg/cycle for the Ce1(PVA₁) and Ce2(PVA₂) samples and they were the thinnest layers compared to other alumina samples. This small difference of 3 mg/cycle in weight was influenced by the higher PVA molecular weight of 31000 g/mol of the Ce2 sample, which increased the suspension viscosity by more than 5 % of PVA with 13000 g/mol.

The first coating cycle of the Al₃ suspension resulted in 11 mg of Al₂O₃ layer loading on the micro-channel plate, which increased linearly with

32 mg and 62 mg after the second and third cycles. The Al₁ layer-loading rose with the same weight rate of 20 mg and 30 mg for the two last cycles, and the three measured Al₁ mass weights were 12 mg higher than the Al₃ layer loading. The coating masses were measured after calcinations following each coating cycle. The Al₂ coating reached the highest loading at 25 mg after the first cycle and 50 mg after the last two coating procedures, which gave the total mass of 125 mg. However, the samples Al₁ and Al₂ had the same concentration of PVA; the longer chains of PVA with a molecular weight of 31000 g/mol affected the higher suspension viscosity.

Table 13 Effect of binder and number of layers on the catalyst deposition

Sample	Layer no.	Mw of PVA	Phenomena
Al1/I	I	13000	A thin and even deposit layer with cracks situated in the middle and on the opposite channel walls; good adhesion, a porous structure.
Al1/II	II	13000	A thin layer with cracks on the opposite walls and no cracks in the middle-channel; good adhesion, porous layer surface
Al1/III	III	13000	A thick and uneven deposit layer with deep cracks; layer separations from channel walls; porous layer structure
Al2/I	I	31000	A thick deposit layer with cracks; well adhered and very dense (packed) structure
Al2/II	II	31000	A thick and uneven deposit layer; cracks were seen; a very dense, packed structure and poorly-adhered coat
Al2/III	III	31000	A thick and porous layer with deep cracks; the catalyst was more widely distributed on the catalyst support due to its high porous structure
Al3/I	I	124000	A thin and even layer, very porous and a well-adhered coat had only very small cracks
Al3/II	II	124000	A thin and porous layer with a dense mesh of small cracks
Al3/III	III	124000	A thick, uneven deposit layer with cracks; a highly-dense layer on opposite walls and porous structure in the middle of channel; low adhesion
Ce1/I Ce2/I	I	13000;31000	A very thin and even layer with some metallic grains from the plate on the washcoat surface (EDX), crack-free, good adhesion
Ce1/II Ce2/II	II	13000;31000	A thin and even layer with no cracks, a porous and well-adhered catalyst layer
Ce1/III Ce2/III	III	13000;31000	A thick and perfectly-even layer without any cracks and larger particles with good adhesion

The Al₂O₃ coatings showed more rapid growth of the layer thicknesses with each cycle compared to the thinner CeO₂ coatings, which was caused by the higher suspension viscosity due to higher PVA concentration and their molecular weight and the Al₂O₃ surface area that was three times the size.

5.2.3.6 EFFECT OF LAYER NUMBER AND BINDER MOLECULAR WEIGHT ON STRUCTURE MORPHOLOGY

The micro-channels were coated one to three times with each suspension in order to find the optimum layer thickness. In addition, the different weights of loaded catalyst supports affected the changes in structure morphology. Table 13 shows the results of the layer loading and PVA molecular weight effects on the Al₂O₃ and CeO₂ washcoat texture deformations based on the SEM analysis.

The increase in the number of Al₂O₃ layers clearly led to the increase of their poor deposition. The largest layer deteriorations such as cracks in the range of 25 μm were found for the Al2/III sample, with the highest viscosity due to a higher PVA molecular weight. The Al1/III sample had the same PVA binder content of 7 wt.% but a lower molecular weight of 13000 g/mol. However, the PVA₃ (124000 g/mol) addition with a concentration of 0.7 wt.% influenced the achievement of adhesive, even and porous Al3/I layer in the micro-channels.

For the CeO₂ samples, the perfectly even and well-adhered layers were achieved even for the thrice-coated channels. There were no significant texture differences between the all-Pt/CeO₂ catalyst layers coated with the same number of layer but with different binder additions.

5.2.3.7 ADHESION

In order to improve the coat adhesion, three layer loadings (thicknesses) were achieved after the coating of each Al₂O₃ and CeO₂ suspensions. Beyond the effect of layer loading, the effect of PVA molecular weight on the layer adhesion was analysed

The CeO₂ coatings showed the highest adhesion and long-term stability during the thermal shock tests compared to the Al₂O₃ layers. For the Ce1(I-coat) and Ce2(II-coat) samples, no coating losses resulted. However, although complete stabilization was found for all CeO₂ layers after different shock times, the Ce2(I-coat) sample showed the maximum weight loss at 7.5 wt.% after the third shock (Figs. 51 and 52). In the case of Al₂O₃ layers, the adhesion was still increasing with PVA molecular weight for all Al1 samples. The first layer stabilization was noted for the Al2(I-coat) and then for the Al3(I,III-coat) samples, with the least loss at 2 wt.% after the fifth shock (Fig. 53).

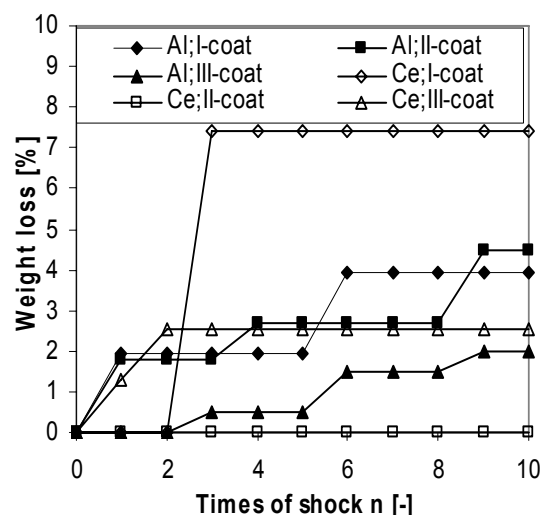


Figure 51 Mass loss of Al₂O₃ and CeO₂ washcoats for three different layer thicknesses and PVA addition (Mw=13000) vs. frequencies in the thermal shock test.

Figs. 54-56 show that the CeO_2 layers in ultrasonic tests were also more adhesive than Al_2O_3 coatings. Adhesion characteristics in this case were also still connected with the layer number and binder molecular weight. The weight loss of coating increased with the decreasing layer number for all samples. The highest coating stability was found with the Ce1(II-coats) sample after 10 min of ultrasonication with 9 wt.% weight loss, but the lowest mass losses were shown by the Ce1(III-coat) after 30 min (Figs. 54 and 55).

For the effect of different PVA influences on the adhesion of the Al_2O_3 catalyst support, it was clear to see that the PVA molecular weight of 124000 g/mol affected adhesion of the Al3(III-coat) washcoat the greatest, compared to the other two Al3 samples (Fig. 56). It was significant to observe that only coated Al_2O_3 layers (A1 and A2-samples) showed complete weight losses after 40 min of ultrasonic vibration (Figs. 54 and 55).

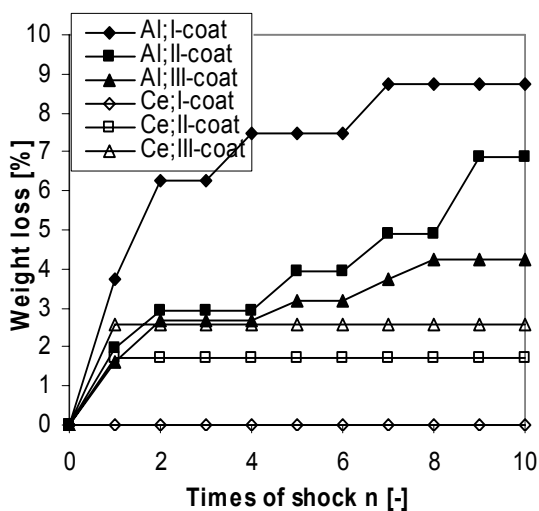


Figure 52 Mass loss of Al_2O_3 and- CeO_2 -washcoats for three different layer thicknesses and PVA addition ($M_w=31000$) vs. frequencies in the thermal shock test.

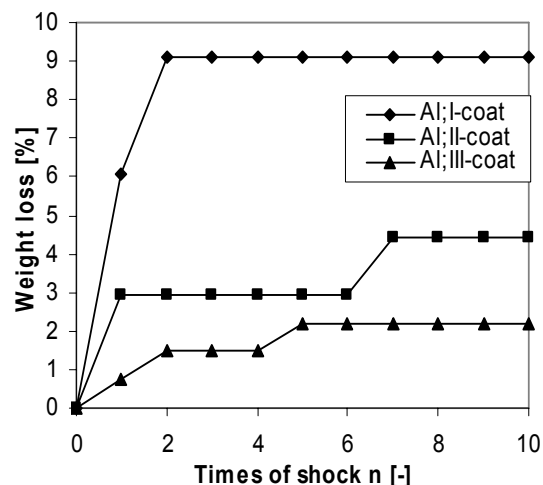


Figure 53 Mass loss of Al_2O_3 and- CeO_2 -washcoats for three different layer thicknesses and PVA addition ($M_w=124000$) vs. frequencies in the thermal shock test.

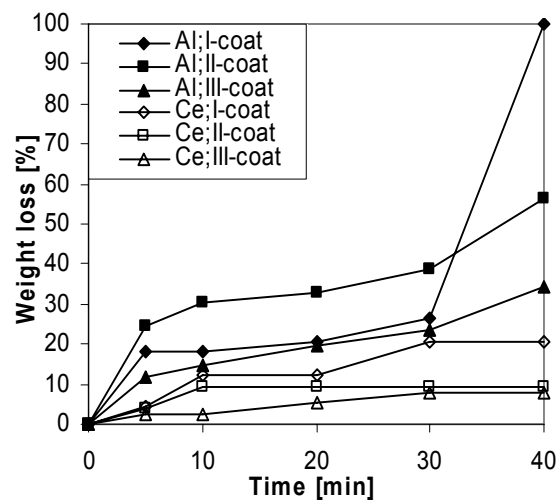


Figure 54 Mass loss of Al_2O_3 and- CeO_2 -washcoats for three different layer thicknesses and PVA addition ($M_w=13000$) vs. time in the ultrasonic vibration test.

In the results of mercury porosimetry (Table 12), the correlation between the bulk density and the adhesion of the layers was found. The higher the bulk density for each sample, the lower the weight loss during the thermal shocks and ultrasonic

vibration tests. The bulk density increase resulted from the increased PVA molecular weight and for this reason the Al₃ sample with the highest bulk density of 0.87 g/cm³ had the highest structure quality compared other Al₂O₃ layers.

The CeO₂ coating showed the perfect heat resistance during the thermal shocks, with no weight loss and the highest cohesive ability after ultrasonic vibration. For this coating, 1.31-1.42 g/cm³ of bulk density resulted according to the PVA molecular weight increase.

The significant differences in the surface texture of both Al₂O₃ and CeO₂ supports were presented in Table 13. Based on the SEM micrographs, it can be seen that the Al₂O₃ layers had an uneven, porous structure with some nm-cracks but the highest BET surface area (216.4 m²/g). On the other hand, the more densely-packed particles of the CeO₂ layer formed the even and highly-adhesive layer with the highest total specific surface area (Table 12).

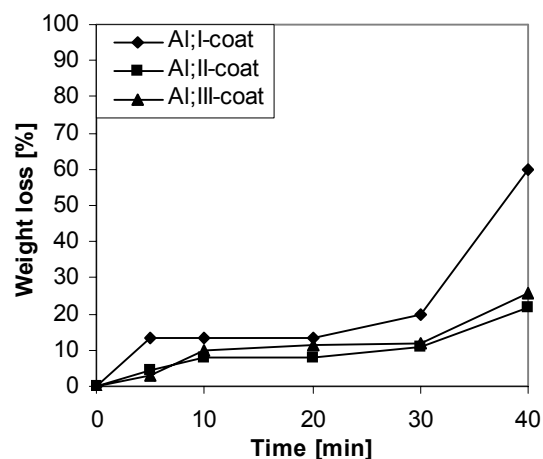


Figure 56 Mass loss of Al₂O₃ and-CeO₂washcoats for three different layer thicknesses and PVA addition (Mw=124000) vs. time in the ultrasonic vibration test.

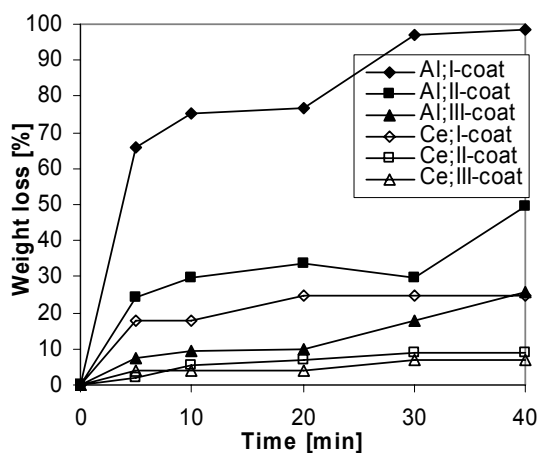


Figure 55 Mass loss of Al₂O₃ and-CeO₂washcoats for three different layer thicknesses and PVA addition (Mw=31000) vs. time in the ultrasonic vibration test.

6 HYDROGEN PURIFICATION USING MICROSTRUCTURES

PART II: CATALYTIC PERFORMANCE OF NM-Pt- CATALYST FOR WATER GAS SHIFT ON MICROSTRUCTURED PLATES ^[122]

6.1 EXPERIMENTAL SECTION

6.1.1 EXPERIMENTAL SET-UP (MICROCHANNEL PLATES)

The catalyst coating was applied to micro-structured foils (50 mm x 50 mm x 1 mm) containing 49 channels that were 400 μm deep and 600 μm wide. The micro-reactor and foils were made of stainless steel (DIN 1.4571). The test reactor was applied with one micro-structured platelet. Each plate was coated with the individual support (Al_2O_3 or CeO_2) and the catalyst system (Pt or Pt/ CeO_2). The coated foil was stacked with filler plates inside of the stainless-steel housing. The housing was sealed with graphite seals. The heating was performed by heating cartridges of 250 W power placed in the boreholes of a metal block in the upper and lower parts of reactor. The reactor temperature was measured by two thermocouples located in the reactor housing close to the exit for the analysing of the inlet and outlet temperatures of the gases. The temperature deviation between the reactor inlet and input was less than 2 $^\circ\text{C}$. Mass flow controllers regulated the gas flows (BRONKHORST HI-TEC). Water was dosed by a dosing liquid controller (BRONKHORST CEM). The water tank was pressurized with nitrogen supplied to the controller with liquid water. The product-gas analysis was carried out at the reactor exit by an on-line gas analyser (Advance Optima).

Each plate was reduced with a flow-gas mixture containing 10 % H_2 in nitrogen under 100 ml n/min. The temperature was raised from 25 to 450 $^\circ\text{C}$ at a rate of 5 $^\circ\text{C}/\text{min}$, and then kept at 450 $^\circ\text{C}$ for 30 min. After that, the temperature was lowered to 200 $^\circ\text{C}$ and switched to reactive flow with a feed composition to start the WGS-reaction tests (Table 14).

6.1.2 CATALYST PREPARATION (SUSPENSION)

The gamma alumina (Alfa Aesar) and CeO_2 (Sigma-Aldrich) were used as the main materials, with a mean size of 20 nm (180 m^2/g) and smaller than 25 nm, respectively. Polyvinyl alcohols (PVAs from Sigma-Aldrich) with three different molecular weights such as 13000-23000 g/mol (PVA_1), 31000-50000 g/mol (PVA_2) and 124000-186000 g/mol (PVA_3) were used as binders. Their viscosities measured by the distributor were given for 4% of PVA in water and were as follows: 3.5 – 4.5 cP, 5.4 – 6.5 cP and 55 – 65 cP, respectively.

The stability of the slurries was studied with the aim of zeta-potential measurements. Small samples from slurries were diluted in an aqueous solution of 10 mM KCl. The pH adjustment was followed by either HCl or NaOH 1M, 0.1M and 0.01M. The samples of the solution were injected in the electrophoresis cell and the two measurements of zeta-potential and particle size were obtained.

Table 14 Feed gas composition – WGS reaction

	Mol.%	vol.%	ml/min	ml/min	ml/min	ml/min	ml/min	ml/min
CO	0.119	11.942	4.76	3.99	3.43	8.34	6.99	6.01
CO₂	0.067	6.675	2.66	2.23	1.92	4.66	3.90	3.36
H₂	0.191	19.107	10.51	8.8	7.58	18.39	15.41	13.26
N₂	0.264	26.351	14.33	12	10.33	25.07	21.01	18.08
H₂O	0.359	35.925	7.74	12.97	16.74	13.55	22.7	29.3
Total	1	100	40	40	40	70	70	70
H₂O/CO			1.6	3.2	4.9	1.6	3.2	4.9
S/G			0.24	0.48	0.72	0.24	0.48	0.72

Table 15 Pt/CeO₂/Al₂O₃-and Pt/CeO₂-catalyst compositions

Sample	Catalyst weight [mg]	Pt [mg]	CeO ₂ [mg]	Layer nr.	PVA [g/mol]
1- Pt/Ce/Al	15.8	0.15	3.8	I	124000
2- Pt/Ce/Al	29.8	0.3	6	I	13000
3- Pt/Ce/Al	38.5	0.4	9.6	I	31000
4- Pt/Ce/Al	40.6	0.4	8.7	II	124000
5- Pt/Ce/Al	58.2	0.55	13.8	II	13000
6- Pt/Ce/Al	81.9	1	19.2	III	124000
7- Pt/Ce/Al	95.6	1	22.6	II	31000
8- Pt/Ce/Al	100.9	0.96	24.96	III	13000
9- Pt/Ce/Al	168	1.6	39.8	III	31000
1- Pt/Ce	12.3	0.1	12.2	I	13000
2- Pt/Ce	15.05	0.15	14.9	II	13000
3- Pt/Ce	25.6	0.2	25.4	III	13000
4- Pt/Ce	26.15	0.25	25.9	I	31000
5- Pt/Ce	37.9	0.4	37.5	II	31000
6- Pt/Ce	42.4	0.4	42	III	31000

The same solid content was prepared for the procedure of the micro-channel platelets coating with the suspensions. The binder weight was chosen based on the results of the smallest Al₂O₃ and CeO₂ particle sizes presented in Table 15. The literature showed that the highest adhesion of the powder used as a catalyst carrier and coated on microstructures belong to the smallest particles [117]. Firstly, each of three PVAs were dissolved in water at 60 °C with the concentration of 16% of PVA₁, 16% of PVA₂ and 1.6% of PVA₃ for the three

samples of the Al₂O₃ suspension. The aqueous CeO₂ suspension samples were made of the same PVAs but with different concentrations of 20%, 15% and 5% for the PVA₁, PVA₂ and PVA₃, respectively. The 20 % of powders were added to each of six suspension samples and stirred overnight. The additive of Na₂SO₄ (20 mM) replaced the KCl to dilute the thicker suspension to avoid the corrosion effect. The cationic or anionic surfactants such as certimonium bromide (CETAB, 20 mM) and sodium dodecyl sulfate (SDS, 80 mM) 1:10 were then

added to the Al_2O_3 and CeO_2 suspensions, respectively. The surfactants were used to lower the surface tension of the suspension and to avoid the layer splitting after coating and during the reaction tests. The HNO_3 and NaOH were used for pH adjustment. The HNO_3 was found to be more effective than HCl , too high a concentration of which also caused a corrosion effect and catalyst losses from the metallic plates.

6.1.3 COATING OF THE PLATES (SPIN COATING AND IMPREGNATION)

The micro-structured substrates were first cleaned in an ultrasonic bath with 2-propanol, then dried and heated in air at $900\text{ }^\circ\text{C}$ for 3 h. After positioning and masking the substrates, the prepared wash-coat slurry was deposited onto the micro-structured channels. The micro-channels were filled completely with the syringe and surplus slurry outside of the channels was removed by a stainless-steel knife with a flat edge. After coating, the plates were putted into a spin coater before the suspension dried. The surplus slurry inside the channels was removed due to the rotation of the plate. The spin coater was programmed in two steps with speeds of 500 rpm for 5 s and then 1000 rpm for 10 s. The coats were then calcined in hot air at a temperature and time determined by TGA analysis. The amount of catalyst applied with each plate was then measured by weighing. This was determined by the amount of powder in the aqueous suspension.

The $\text{Pt/CeO}_2/\text{Al}_2\text{O}_3$ and Pt/CeO_2 catalysts were prepared by impregnating the spin-coated Al_2O_3 and CeO_2 layers with aqueous solutions of $\text{Ce}(\text{NO}_3)_2$ (99.9% purity, purchased from Fluka) and H_2PtCl_6 (99.9% purity, purchased from Fluka). Then the coatings were dried at $110\text{ }^\circ\text{C}$ for 0.5 h and calcined at $400\text{ }^\circ\text{C}$ for 2 h and $450\text{ }^\circ\text{C}$ for 4 h after impregnation with an aqueous solution of Ce-nitrate and H_2PtCl_6 , respectively. The loading of CeO_2 and

Pt was controlled and determined by weighing. In addition, the EDAX analysis was performed to determine the catalyst dispersion on the Al_2O_3 and CeO_2 supports.

6.2 RESULTS AND DISCUSSION

6.2.1 EFFECT OF IMPREGNATION NUMBER ON CATALYST LOADING

The relation between an Al_2O_3 support loading and the loading of CeO_2 coatings is shown in Fig. 57. It was found that the BET surface area and the loading of the coating greatly affected their mass weight level, which increased linearly.

For the first impregnation, using the slurry with 0.7 wt.% PVA (124000 g/mol), the loading of the coating was 1.7 wt.%. When the PVA₁ (13000 g/mol) or PVA₂ (31000 g/mol) with 7 wt.% concentration in the slurry was used, the loadings of coatings could reach 8.9 or 15. wt.%, respectively.

The loading of the catalyst by the impregnation method depends on the support density and the material loading in the micro-channels. The different slurry viscosities were achieved through the addition of three PVAs (13000, 31000 and 124000 g/mol), which influenced the bulk structure (densities) and also changed the layer loading. Therefore, multi-impregnation was often required, because a suitable loading of the catalyst can not generally be coated sufficiently by a single impregnation. For the second application by an impregnation, the loading amount on the support Al_2O_3 was much lower than the first loading. The highest coating loading during first impregnation was caused by the higher capillary attraction of the support and due to the absorption of the particles on the surface of Al_2O_3 .

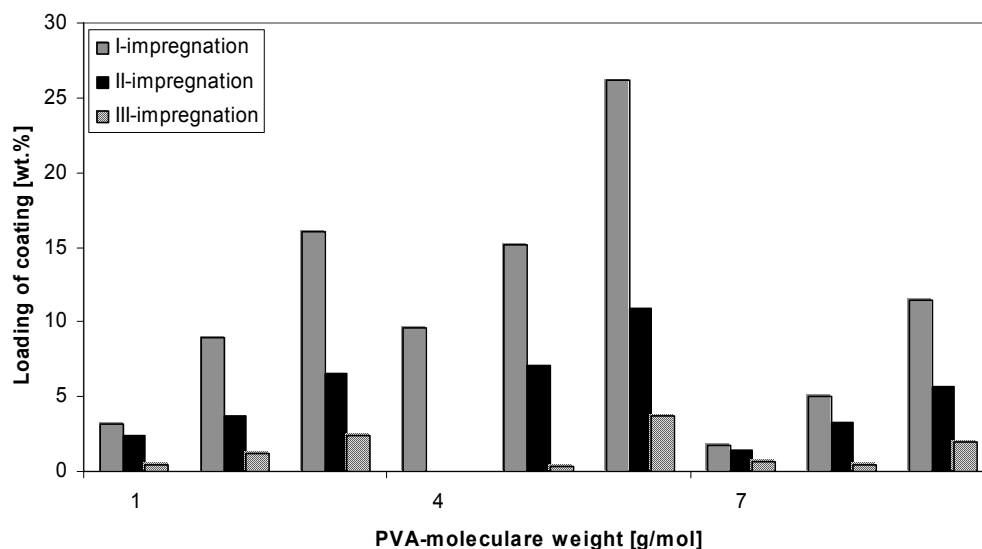


Figure 57 The loading of CeO₂-coating by impregnation on the Al₂O₃-support, which contained different PVAs (13000, 31000 and 124000 g/mol).

The results show that the higher support loading with its lower bulk density was advantageous for enhancing the catalyst loading. In this experimental work the Pt impregnation was carried out in the channels under one run on the both CeO₂ and Al₂O₃ supports. It caused the metal species to become embedded on the surface and in pores, which could block them up. This leads to a decrease in the interior surface area. It was also found that if the loading of the aqueous solution with catalyst precursors was too high, the coating deposited on the supporting Al₂O₃ or CeO₂ coat peeled off easily from the micro-channel platelets during the calcination process. This was also the reason for choosing multi-impregnation to achieve 1 wt. % of Pt on the CeO₂ and Al₂O₃ layers.

6.2.2 MORFOLOGY OF THE COATED CATALYSTS

Fig. 58 and Fig. 59 illustrate the morphology of the coated micro-channel platelets with Pt/CeO₂/Al₂O₃ and Pt/CeO₂ catalysts. The Al₂O₃ surface exhibits porous deposits with heterogeneous spreading of cerium oxide particles, whose high concentration was clear to see in the form of the crack-free white areas on the support surface in the channels (Fig.58). The best quality of the Al₂O₃ layer was achieved for the thinnest coatings, but some micro-cracks were still observed on the surface. The Pt/CeO₂ catalyst was distributed homogeneously on the stainless-steel foil without any cracks. All channels are covered by perfectly-even catalyst coating (Fig. 59), which was achieved after variations in the CeO₂/H₂O ratio in the suspension.

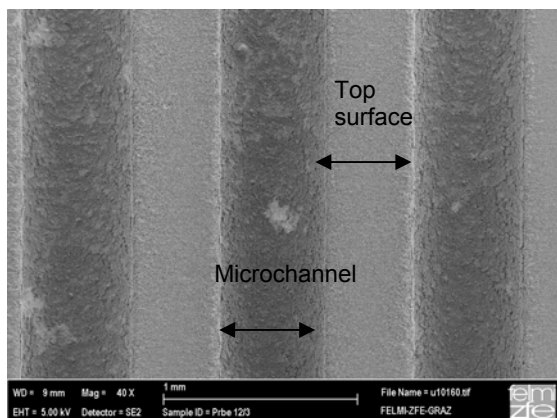


Figure 58 The surface morphology of Pt/CeO₂/Al₂O₃ catalyst in microchannels.

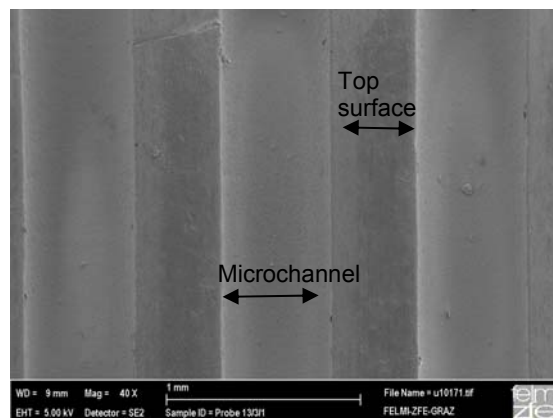


Figure 59 The surface morphology of Pt/CeO₂ catalyst in microchannels.

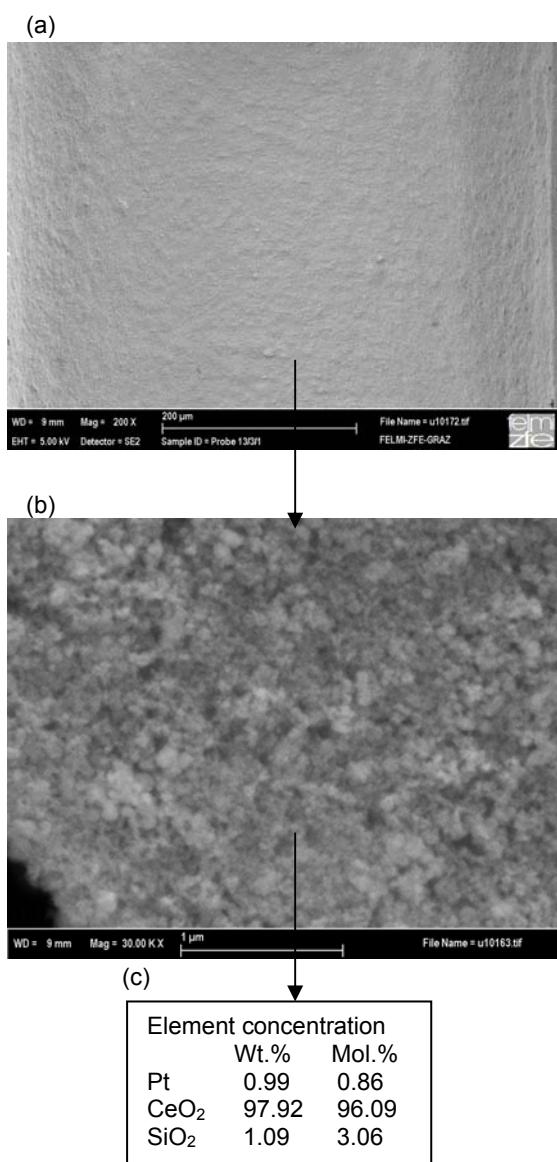


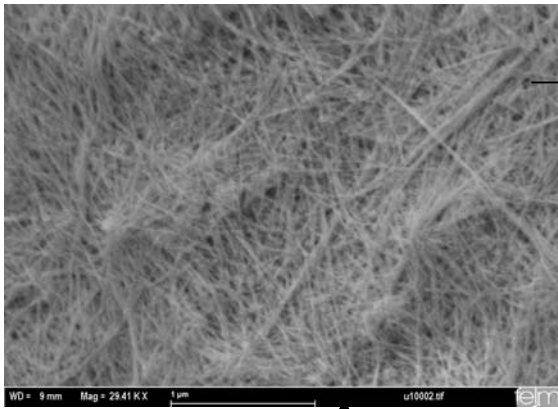
Figure 60 The SEM photographs and elemental profiles by EDX for the Pt/CeO₂-catalyst coated on the microchannel platelets.

Poor distribution of the Pt/CeO₂ catalyst on Al1(I-coat) was due to the low weight of the coated catalyst; the CeO₂ phase diameters were below 40 nm. The thicker Al1/II-layer had wider catalyst distribution. The white Pt/CeO₂ spots were heterogeneously distributed on the Al1/III and showed small distances between each other; the CeO₂ phase was above 12-67 nm in diameter.

Rarely catalyst distribution with 56 nm diameters of the CeO₂ phase on Al2/I-layer in the channels was caused by the 0.4 mg Pt and 9.6 mg CeO₂ catalyst coating. The next two Al2/II and Al2/III-layers showed CeO₂ sizes below 64 nm. The smallest CeO₂ phase diameter was founded to be lower than 17 nm on the Al3/I coating.

The photographs with higher magnification show directly the coated channel (Fig. 60 a and 61-1) and the inner surfaces of the layers (Fig. 60b, 61-2a and 61-2b) with the results of elemental analysis by EDX of some magnified surface fields (Fig. 60c and Fig. 61-3a, 61-3b). Fig 60a shows that even the edges of the micro-channels were coated with ideal uniformity. The layer was also highly adherent and even throughout the channel. The Al₂O₃ layer exhibits higher total porosity and the total specific surface area than the CeO₂ coat, which was confirmed by the results from mercury porosimeter [116].

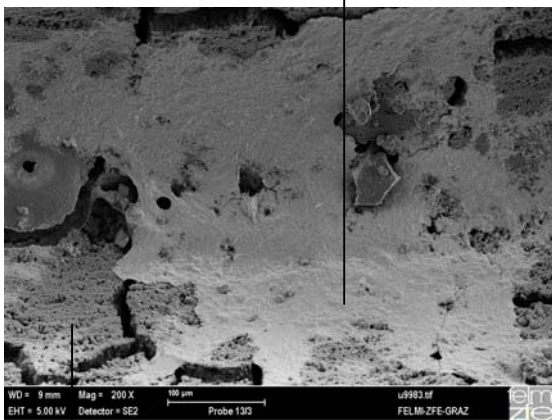
(2a)



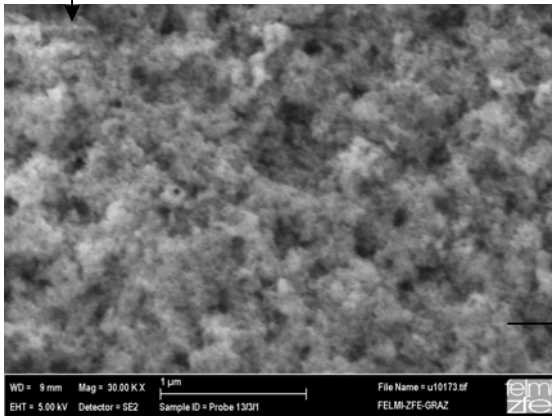
(3a)

Element concentration		
	Wt.%	Mol.%
Pt	0.99	0.59
CeO ₂	64.50	43.39
Al ₂ O ₃	34.51	56.02

(1)



(2b)



(3b)

Element concentration		
	Wt.%	Mol.%
Pt	1.26	0.7
CeO ₂	15.95	10.07
Al ₂ O ₃	82.05	88.31
Cl ₂ O	0.74	0.92

Figure 61 The SEM photographs and elemental profiles by EDX for the Pt/CeO₂/Al₂O₃-catalyst coated on the microchannel.

The inner structure of the CeO₂ coating was porous with homogeneously-packed round particles (Fig. 60b). The elemental EDX analysis results showed that Pt/CeO₂ catalyst sample contained a small, unexpected amount of 1.09 wt.% SiO₂, which was in the as-received CeO₂-powder (Fig 60c).

Fig. 61-1 shows non-homogeneously distributed CeO₂ particles on porous Al₂O₃ support. The larger magnifications (Fig.61-2a) reveal the CeO₂ regions, which are based on the phase of dense white nm-fibres crossing with each other in different directions. It was reported from the elemental EDX analysis that in this part of the coated channel, the catalyst concentration was 0.99 wt.% Pt/64.5 wt.% CeO₂/Al₂O₃ (fig.61-3a). Based on the EDX elemental analysis, the catalyst concentration in other layer area reached a higher Pt concentration of 1.26 wt.% and a low CeO₂ content of only 15.95 wt.%. Some additional 0.74 wt.% of Cl₂O was found from the impregnation with the H₂PtCl₆ aqueous solution (fig. 61-3b).

Fig. 62 represents the elemental profile of 1 wt.% Pt supported on one and three CeO₂ layers made of the suspension based on PVA₁ (Mw of 13000 g/mol), resulting in two different catalyst weights on each foil. For the catalyst with only one support layer, there was not enough Pt at 0.1 mg to detect it through the EDX analysis. Other elements such as Cr and Fe were found, whose peaks belonged to fragments of stainless-steel material of the micro-channel plate (Fig. 62a). The thin catalyst coating meant that the basis metallic support material was transparent for the X-rays during elemental analysis.

Figure 62b shows that the thicker catalyst layer exhibited higher Ce loading (20 mg) and for the first time clear Pt peaks appeared. No visible Cl elements were found for this catalyst weight on either elemental profiles.

The next two figures, 63a and 63b, present the EDX profiles for the Pt/CeO₂ catalyst, where the CeO₂ support was made from suspension containing PVA with a higher molecular weight of 31000 g/mol. Both plots show the same elements, but all the peaks were higher (Fig. 63b) with the thicker catalyst layer (three CeO₂ layers) than with the thinner one (Fig. 63a). The additional Cl peaks were also spotted on the elemental profiles for two catalysts loaded with 0.25 mg and 0.4 mg Pt due to impregnation with H₂PtCl₆ solution. In the case of Pt/CeO₂ supported on Al₂O₃, other elemental differences were found for the same catalyst in two separate channels (Figs. 64a and 64b). This was further proof of the non-homogenous dispersion of catalyst particles. Some regions of the first channel exhibited higher Pt and CeO₂ concentrations than the second channel. The higher peaks of the O, Pt and Ce elements confirmed the higher Pt/CeO₂ content on the Al₂O₃ support.

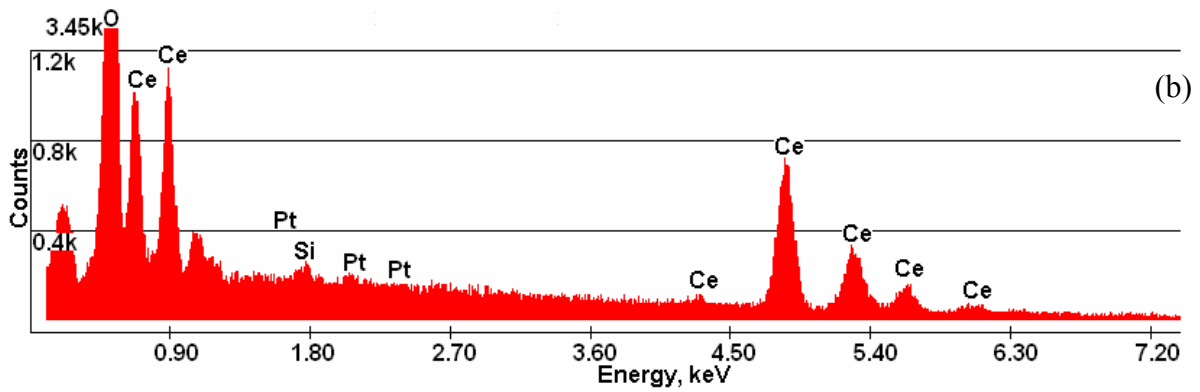
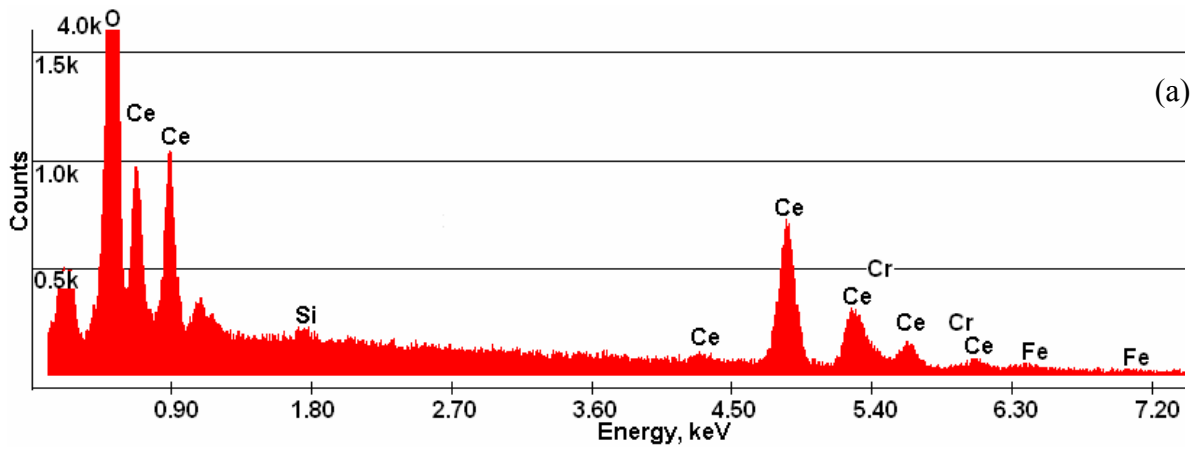


Figure 62 EDX spectrums of samples Pt supported on CeO_2 : a. Ce-1(I-layer), b. Ce-1(III-layers).

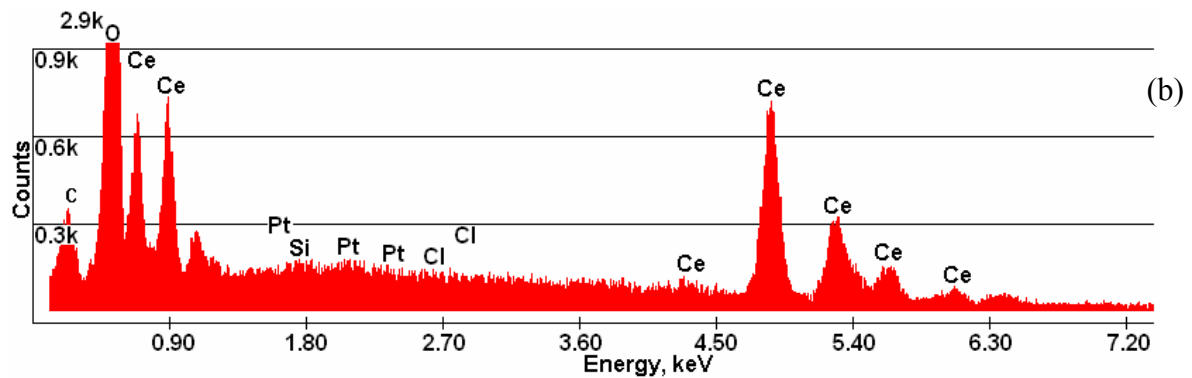
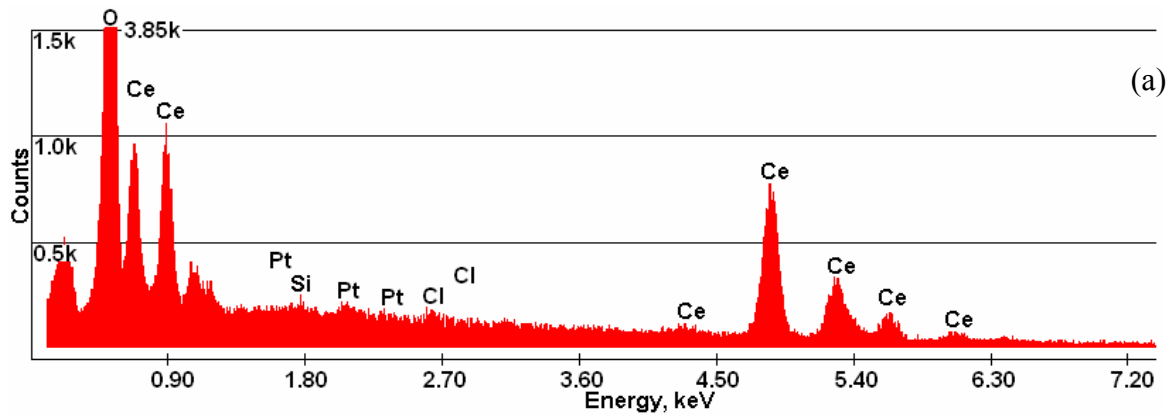


Figure 63 EDX spectrums of samples Pt supported on CeO_2 : a. Ce-2(I-layer), b. Ce-2(III-layers).

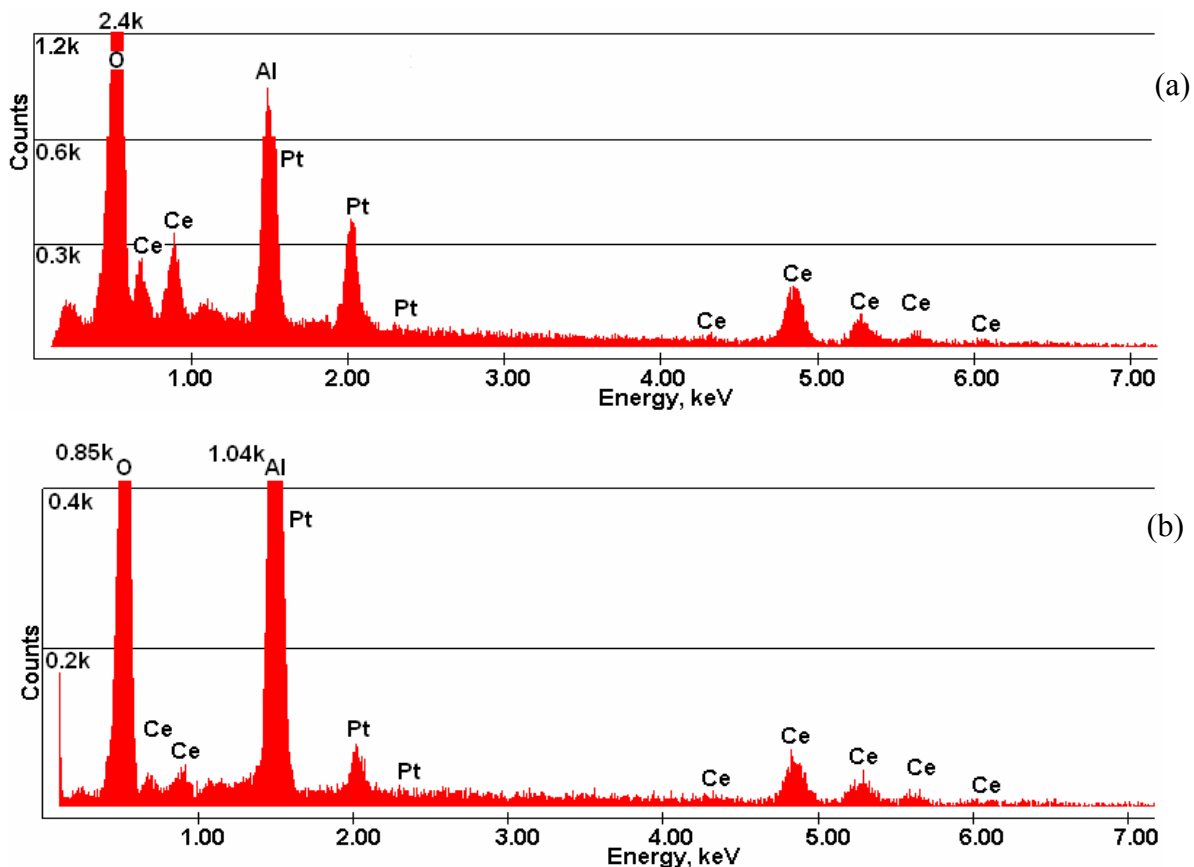


Figure 64 EDX spectrums of the coated catalyst sample Pt/CeO₂ supported on Al₂O₃: Al-1(III-layers) in two different channels.

6.2.3 EFFECT OF H₂O

The WGS reaction is reversible and exothermic and, due to its moderate exothermicity, is thermodynamically unfavourable at elevated temperatures. This is illustrated by the continuous decline and eventual change in the Gibbs free energy as a function of temperature, and the corresponding decreasing equilibrium constant as temperature increases (Figures 65, 67, 68). Of course, the kinetics of the catalytic reaction were more favourable at higher temperatures. However, the higher operating temperature is favourable for smaller reactor sizes due to fast kinetics. The water content has a strong influence on the CO conversion. The steam entering into the WGS reactor can be varied by controlling the water

amount added in the reformer and by injecting water. In addition, CO, CO₂ and H₂ concentrations are mainly dependent on the reformer operating temperature, which in turn determines the thermodynamic limitations.

Figures 65, 67, 68 show that the molar-steam to dry-gas (S/G) ratio rising from 0.24 to 0.72 significantly increased the CO conversion for all catalysts. The highest conversion level of 70 % and 63.5 % was found for sample 9 (168 mg) and sample 6 (82 mg) at 300 °C and 350 °C under 70 ml n/min of total gas flow and 0.24 steam to gas (S/G) ratio (Fig. 62). It is also important to note that sample 7 (95.6 mg) showed lower activity compared to sample 6 (82 mg). Moreover, sample 6 achieved the higher activity due to the best uniformity of the support layer after suspension deposition with PVA₁ (124000 g/mol) then sample 7 received from

suspension containing PVA₂ (31000 g/mol). Both catalysts had the same Pt weight of 1 mg but sample 6 had a lower CeO₂ content. For this reason, the CeO₂ had no influence on the increase in catalyst activity in this case. The next catalyst samples such as samples 8 (101 mg) and 5 (58.2 mg) showed almost the same highest CO conversions of 60.6 % and 60.1 % at 350 °C. The cohesion ability was the main impact factor maintaining the higher catalytic activity of the catalyst layer number 5 (PVA of 13000 g/mol). As was already proved in our recent paper [21], when the layer adhesion decreased with the coating thickness (loading), the catalyst activity decreases. Therefore, in this work the catalyst sample 5 (58 mg) was more active than sample 8 (101 mg) for Pt/CeO₂/Al₂O₃. On the other hand, samples 1-4 were most active at 400 °C operation temperature. Only 55 % CO conversion was noted for sample 4

(41 mg). The activity decreased when catalyst loading dropped, and the lowest conversion value of 40 % was found for sample 1 (16 mg).

The catalyst activity losses were analysed for each catalyst at reaction temperatures from 250 °C to 400 °C. Only catalyst sample 9 (168 mg) showed the CO conversion falling, from 0.5 % to 0.3 % between 250 °C and 400 °C reaction temperatures after 40 min of reaction running (Fig. 66).

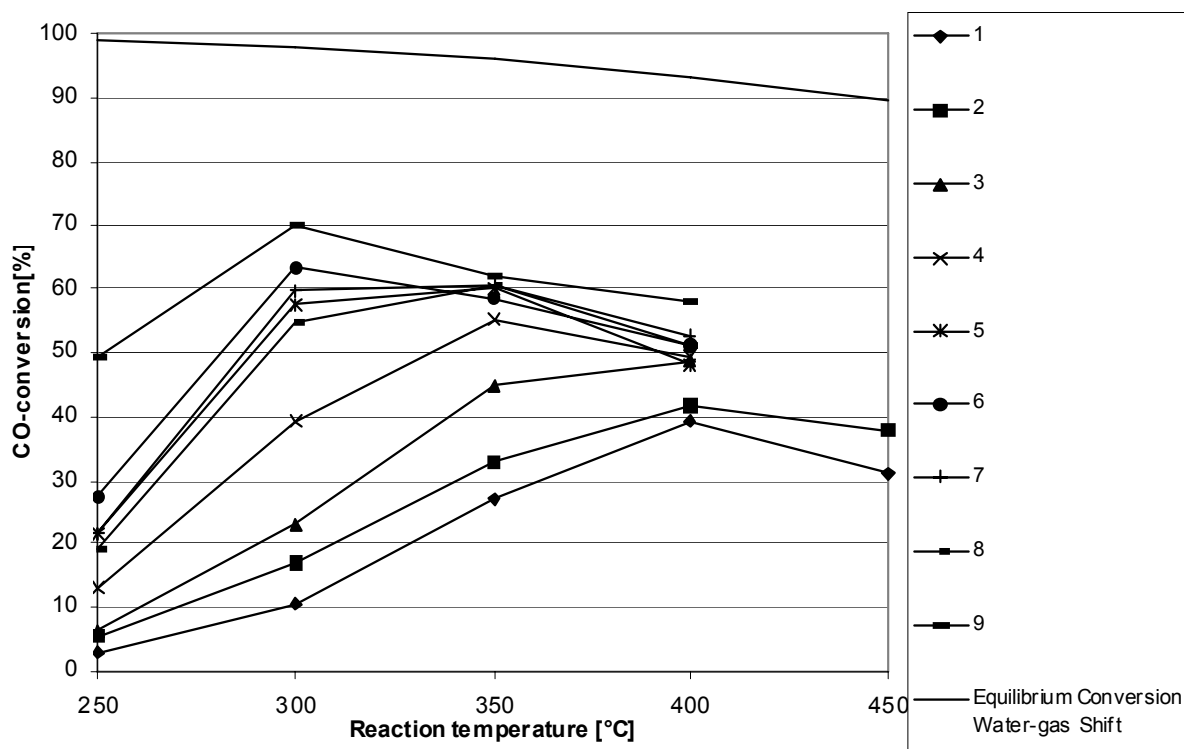


Figure 65 CO-conversion over Pt/CeO₂/Al₂O₃-catalyst samples; S/G=0.24; total feed flow rate: 70 ml/min.

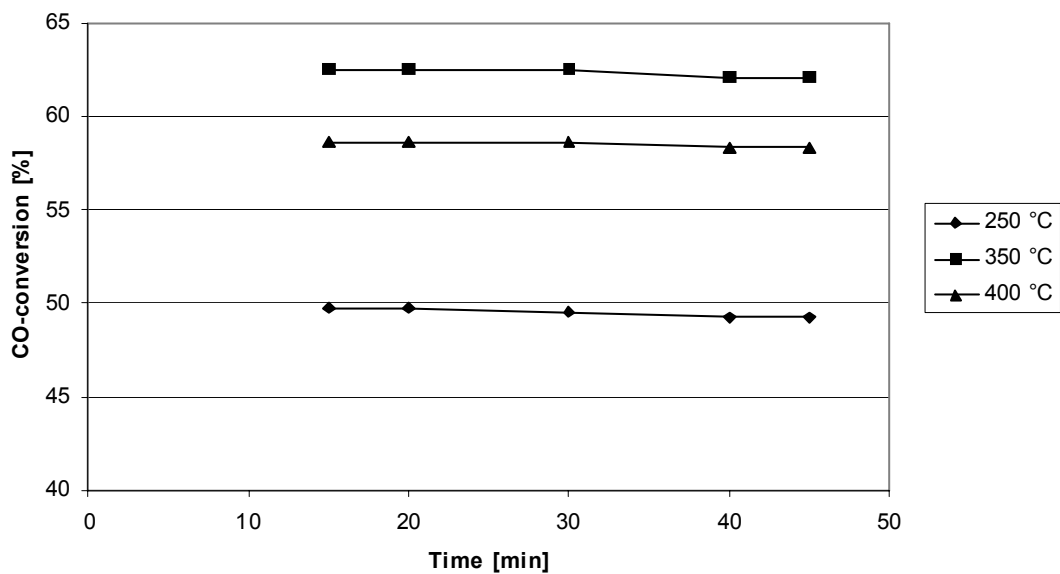


Figure 66 CO-conversion over Pt/CeO₂/Al₂O₃-catalyst (samples nr. 9) as a function of reaction time; S/G=0.24; total feed flow rate: 70 ml/min.

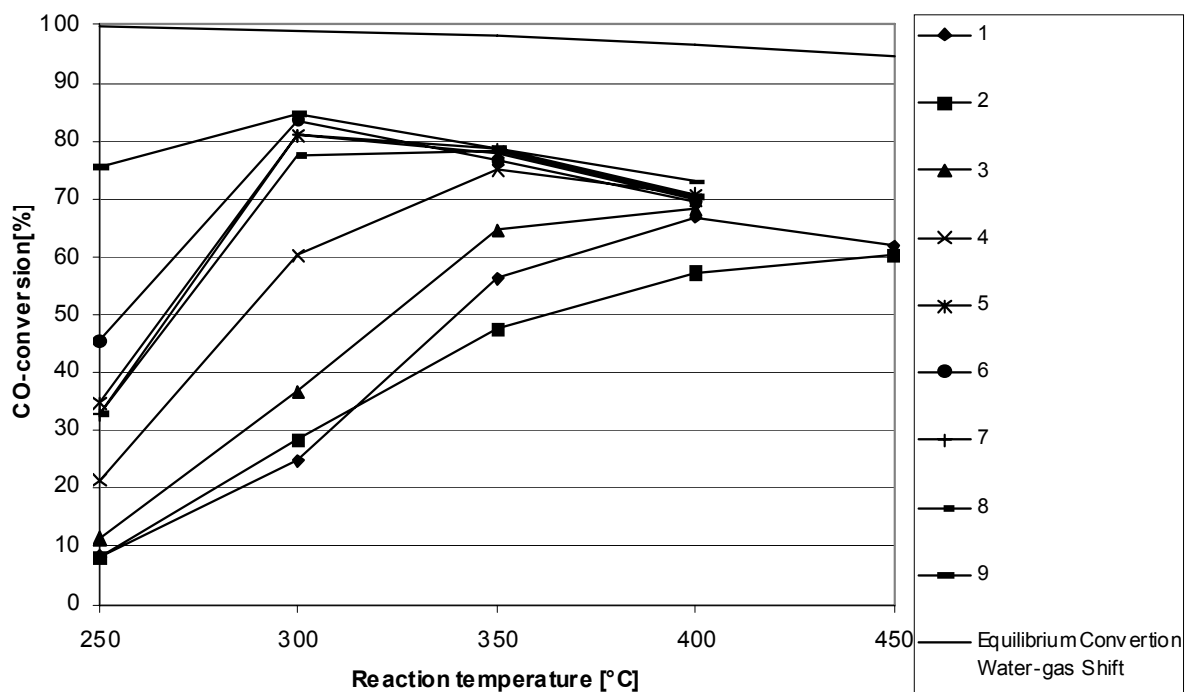


Figure 67 CO-conversion over Pt/CeO₂/Al₂O₃-catalyst samples; S/G=0.48; total feed flow rate: 70 ml/min.

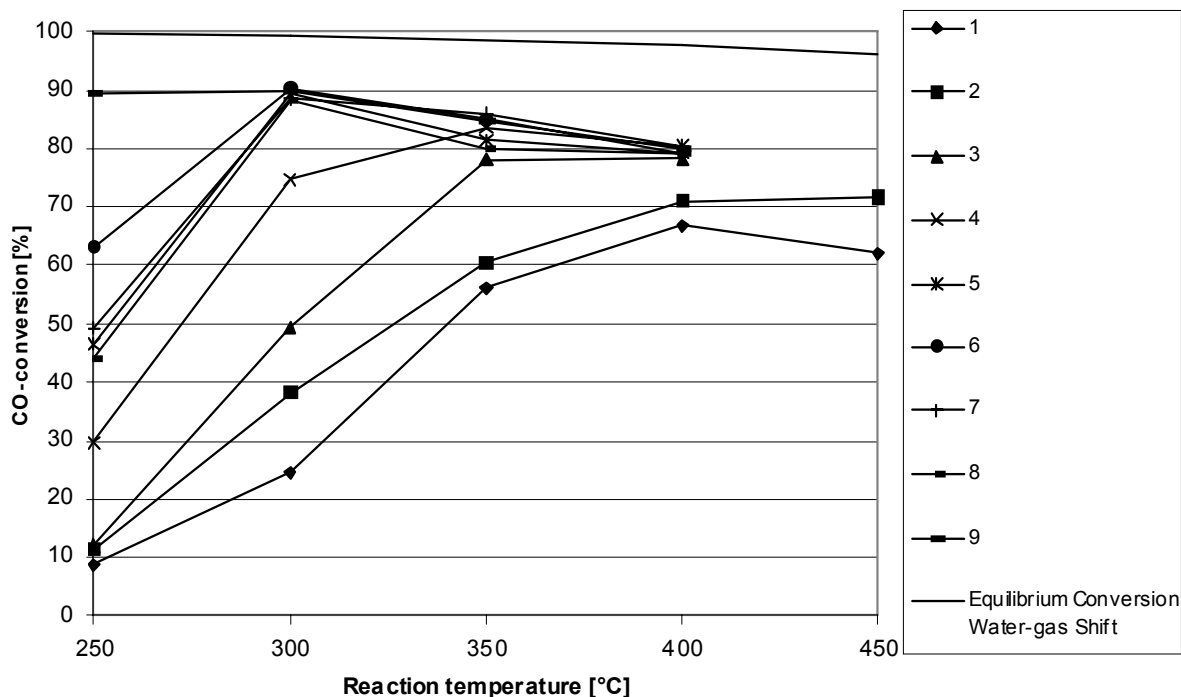


Figure 68 CO-conversion over Pt/CeO₂/Al₂O₃-catalyst samples; S/G=0.72; total feed flow rate: 70 mln/min.

After a steam to gas ratio increase from 0.24 to 0.48, the maximum CO conversion was increased and forwarded in to lower temperature regions. Samples 5 and 7 showed the activity increasing from 350 °C to 300 °C and a CO conversion of 81 % and 78 %, respectively, was reached. In addition, the samples 4 and 1 resulted in the highest CO conversion profiles at lower operation temperatures of 350 °C and 400 °C. In the case of catalyst sample 9, still at 300 °C, 85 % of carbon monoxide in the feed was converted, leaving some 2 % CO left in the dry gas product, which was the highest conversion rate under 0.48 S/G ratio (Fig. 67).

Fig. 68 presents results of the CO conversion over the 0.72 S/G ratio and 70 mln/min total flow. Catalyst sample 9 achieved a constant 1.5% CO in dry gas mixture at the outlet at 250 °C and 300°C operating temperature and represented the highest CO conversion. After the maximum water content was reached with the inlet reacting gas, only catalyst sample 8 showed a better CO conversion performance at lower reaction temperatures of 300 °C.

6.2.4 EFFECT OF CATALYST WEIGHT (WHSV)

It is important for fuel cell systems to determine the effect of WHSV (weight hourly space velocity) to prove its performance as it shows operating conditions after the application of the present water-gas shift catalysts. As shown in Figs. 69 and 70, with lower WHSV the reactant gases had more time over the catalyst to achieve adsorption, thus leading to a higher CO conversion at a specific temperature.

To achieve 94.4 % CO conversion, a temperature of 250 °C and under the WHSV of 1.3 N l/(h g_{cat}) was needed to be reached by catalyst sample number 9. At 300 °C, this conversion value was 4.4 % lower under WHSV of 25 N l/(h g_{cat}). The CO conversion value of 93 % was the second best result and was achieved at 300 °C with a WHSV of 29.3 and 25.1 N l/(h g_{cat}) at 300 °C for both catalyst samples 6 and 7; however, they had different surface areas and weight used in the

WGS reaction. This surprisingly equal result of higher CO conversion was caused by the higher catalyst surface area of sample 6 under the higher WHSV value at the same reaction temperature even at 14 mg lower weight compared to sample number 7. In addition, the

three equal CO conversions for different catalysts were also found at 300 °C. The following conversion order, such as 92%, 90% and 89%, resulted with WHSVs of 41.2 (23.8) N I / (h g_{cat}), 14.3 (51) N I / (h g_{cat}) and 43.9 (72) N I / (h g_{cat}), respectively (Fig. 69).

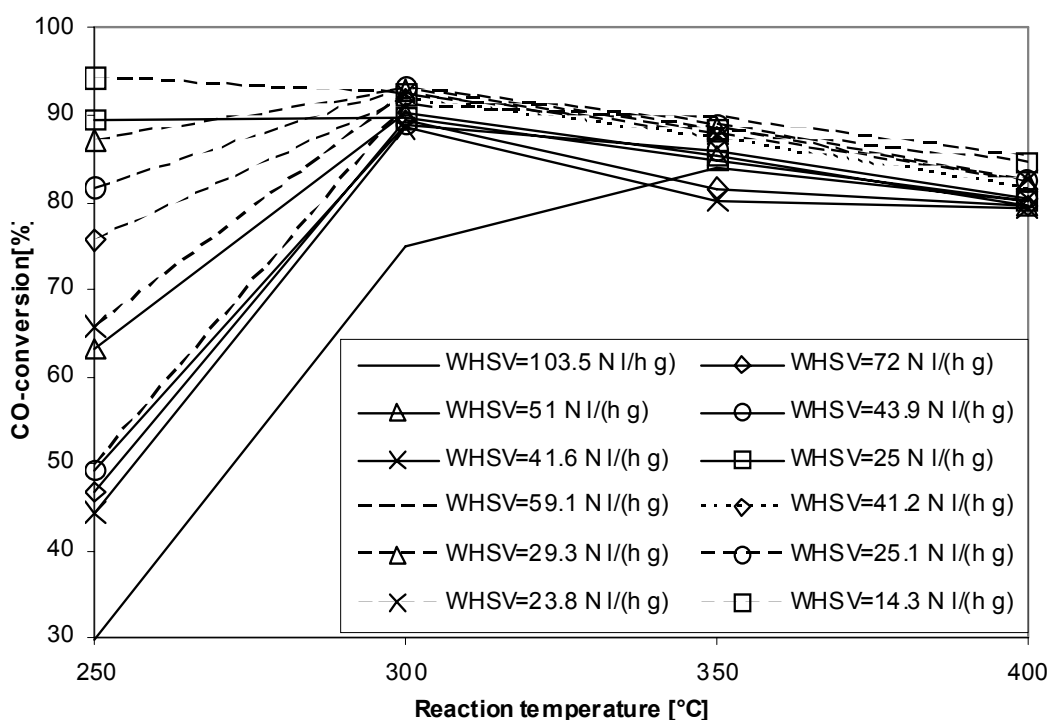


Figure 69 CO-conversion over Pt/CeO₂/Al₂O₃-catalyst samples; S/G=0.72; total feed flow rate: 40 mln/min (dashed line), 70 mln/min (continuous line).

A second group of three Pt/CeO₂/Al₂O₃ catalyst samples was more active in an operating temperature range of between 350°C and 450 °C under 40 mln/min and 70 ml n/min of total gas (Fig. 70). The conversion levels were generally lower compared to the results presented in Fig. 69. To achieve the 87 % of highest CO conversion at 350 °C, a WHSV of 62.3 N I / (h g_{cat}) was required. At 400 °C, the CO conversion of about 79 % was reached under both 40 and 70 mln/min and WHSVs of 151.9, 80.5 and 109.1 N I / (h g_{cat}). Only one catalyst sample with WHSV 140.9 N I / (h g_{cat}) and 70 mln/min still showed rising conversions at temperatures higher than 400 °C, reaching its maximum of 72 % at

450 °C (Fig. 69).

Fig. 71 shows that with increasing reaction temperature from 250 °C to 450 °C and a S/G ratio of 0.72, the CO conversion increased for all Pt/CeO₂ catalyst samples. Thus, the highest CO purification was noted at the highest temperature region of 400-450 °C, in contrast to the Pt/CeO₂/Al₂O₃ catalyst, which showed the conversion only 4 % lower than the WGS reaction equilibrium and the same highest value for CO conversion in this study. Based on Fig. 71, two sets of catalysts can be identified such as the most active catalysts with WHSV from 56.6-93.8 N I / (h g_{cat}) and with

average activity at 195.1-159.5 N l/(h g_{cat}) WHSV range. At operation temperatures of 250 °C and 450 °C and with 63.3 N l/(h g_{cat}), the CO conversion was 5 and 76 %, respectively. Catalyst sample 3 (WHSV of 93.8 N l/(h g_{cat})) exhibited the next highest CO conversion. It achieved 11 % CO conversion at 250 °C while at 450 °C it again showed a much higher CO conversion of 75 %. It was also evident that sample 6 with the WHSV of 56.6 N l/(h g_{cat}), which had a significant influence on the CO-conversion, succeeded in reaching 8 % CO conversion at 250 °C and 72 % CO conversion at a reaction temperature of 400 °C. Thus all catalysts

showed stable activity under the reaction running for several hours. Even at the highest reaction temperature of 450 °C, the CO level was reduced down to 3.5 vol.% (in dry gas). Sample 1 showed the highest activity comparing the average active catalysts. It achieved a CO conversion of 5 % under a WHSV of 195.1 N l/(h g_{cat}) at 250 °C and 68 % CO conversion at 450 °C. The next most active catalyst (sample 2) exhibited the lowest CO conversion of 62.4 % at 450 °C. Additionally, no traces of methane were found for either Pt/CeO₂/Al₂O₃ or Pt/CeO₂ catalysts in the out-gas feed.

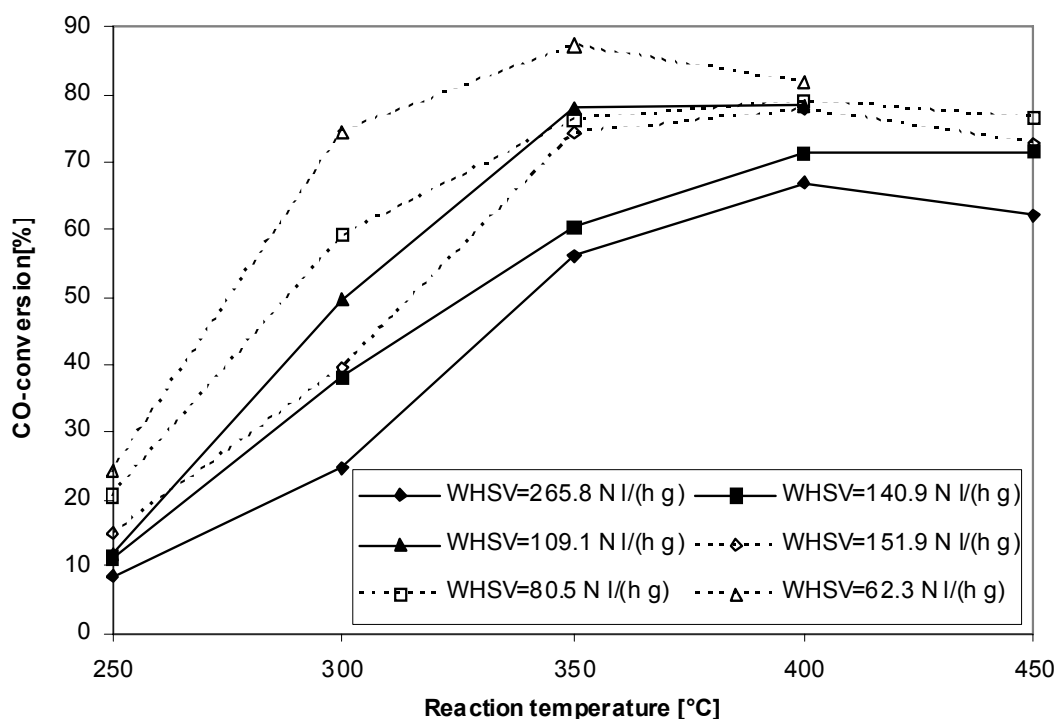


Figure 70 CO-conversion over Pt/CeO₂/ Al₂O₃ -catalyst samples; S/G=0.72; total feed flow rate: 40 mln/min (dashed line), 70 mln/min (continuous line).

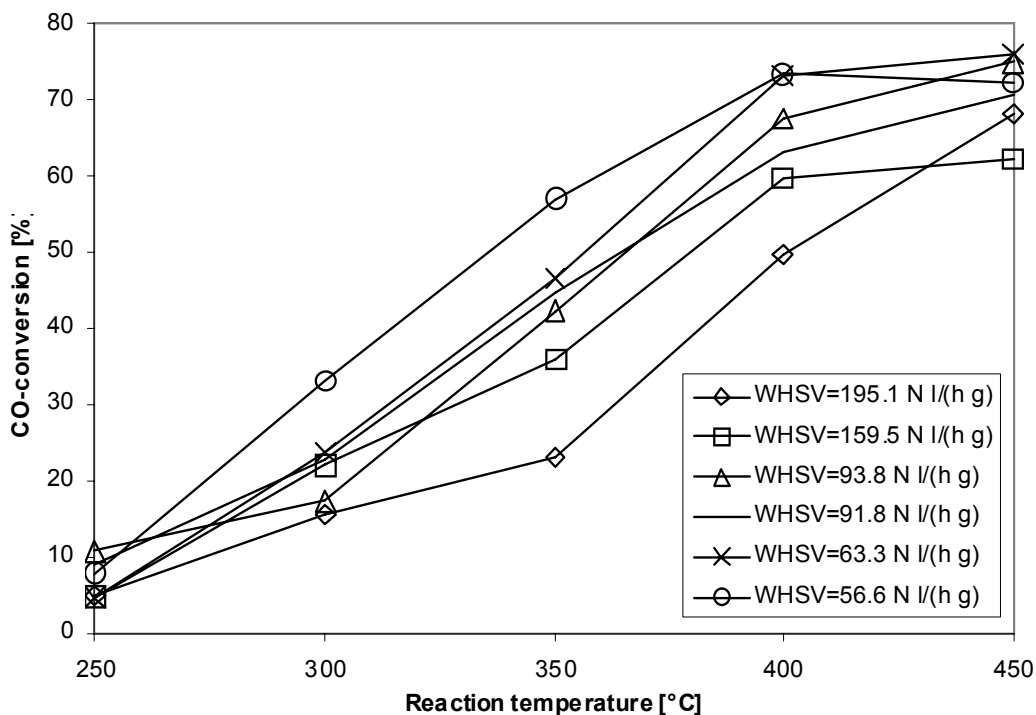


Figure 71 CO-conversion over Pt/CeO₂-catalyst samples; S/G=0.72; total feed flow rate: 40 ml/min.

6.2.5 COMPARISONS BETWEEN Pt/CeO₂/Al₂O₃ AND Pt/CeO₂ CATALYST

Table 16 clarified the limitations of the catalyst activity increases by the variations of the ceria content for the catalyst samples containing 1 wt.% Pt. The CO conversion increased with decreasing WHSV values or with rising catalyst weight. The catalyst samples with 0.98 wt.% and 21.4 wt.% ceria and 1wt.% Pt (0.4 mg) content showed the highest CO conversion of 91 % at 300 °C compared to other catalyst samples. Under the same reaction conditions, the sample with 3.5 wt.% higher ceria content exhibited a much lower CO conversion rate of 74.4 %. However, its second highest CO conversion of 87.2 % was found at a reaction

temperature of 350 °C. In the case of 1 wt.% Pt/CeO₂ catalyst samples, the maximum catalyst activities were detected between 400 and 450 °C, but they still had lower CO conversion levels compared to the Pt/CeO₂/Al₂O₃ catalyst samples. Under the WHSV of 63.3 N l/(h g_{cat}), the 1 wt.% Pt/CeO₂ catalyst showed a lower CO conversion of 46.5 % at 350 °C than the mentioned 1 wt.% Pt/CeO₂/Al₂O₃ catalyst (38.5 mg). The highest activity was noted at 450 °C and the maximum of 76 % CO conversion was reached. An increase of CeO₂ weight up to 42 mg (WHSV of 56.6 N l/(h g_{cat})) contributed to reaching the maximum CO conversion level of 73.5 % at the reaction temperature of 400 °C. This catalyst showed almost 10 % higher CO conversion at 350 °C than the 1 wt.% Pt/CeO₂ sample (37.9 mg). The temperature treatments such as calcination temperature and reaction temperature were limited up to 450 °C to avoid a deterioration of the Pt dispersion.

Table 16 CO-conversion for WGS over Pt/CeO₂/Al₂O₃ and Pt/CeO₂ catalyst samples; S/G=0.72; total feed flow rate: 40 mln/min

Catalyst	Pt [mg]	CeO ₂ [mg]	Total weight [mg]	WHSV [N l/(h g _{cat})]	CO conversion [%]
4- Pt/Ce/Al	0.4 (1.0 wt.%)	8.7 (21.4 wt.%)	40.6	59.1	91.1 (250 °C) 87.9 (300 °C)
3- Pt/Ce/Al	0.4 (1.1 wt.%)	9.6 (24.9 wt.%)	38.5	62.3	74.4 (300 °C) 87.2 (350 °C)
5- Pt/Ce	0.4 (1.0 wt.%)	37.5	37.9	63.3	46.5 (350 °C) 76 (450 °C)
6- Pt/Ce	0.4 (0.9 wt.%)	42	42.4	56.6	57.1 (350 °C) 73.5 (400 °C)

6.2.6 COMMERCIAL CATALYST

In order to investigate the effect of H₂O on the activity of the commercial Pt/CeO₂ catalyst, a wet feed was passed through the reactor while the minimum catalyst temperature was kept above 250 °C, because the entire set-up would not have any colder spots, which could lead to water condensation and thus flood the reactor.

As shown in Fig. 72, H₂O had a dramatic effect on CO conversion between the temperatures of 250 and 350 °C. At a temperature of 250 °C, CO conversion was around 76 %, when only 0.24 S/G has been present in the feed. On the other hand, it reached a higher CO conversion of 94.3 % when 0.72 S/G was added. The influence of the H₂O addition dominated up to the temperature of 250 °C, where with the ratios of S/G=0.48 and S/G of 0.72 in the feed obtained 91.4 % and 94.3 % CO conversion. The slight CO conversion decrease of 17 % was found between the temperatures of 300 °C and 450 °C with the wet feed when the S/G-ratio of 0.72 was attributed to the fact that the CO conversion dropped due to changes in the Gibbs free energy, which was a function of temperature, and due to the corresponding decreasing of the equilibrium constant with the temperature increase. For this reason,

the exothermic WGS reaction was thermodynamically unfavourable at elevated temperatures.

It needs to be mentioned that the methanation reaction started at a temperature of 350 °C for the commercial Pt/CeO₂ catalyst and reached 2 %. At 400 °C and 450 °C, more methane – 7 % and 20 %, respectively – was detected.

This catalyst achieved the same high CO conversion of 94 % only at 250 °C and an S/G ratio of 0.72 under 40 mln/min total gas flow as the self-coated Pt/CeO₂/Al₂O₃ catalyst. It was explained that the industrial catalyst consisted of 1.25 times higher platinum weight to be highly active in the WGS reaction tests under the same reaction conditions. At higher operation temperatures such as 300 and 350 °C, the industrial catalyst showed a lower CO purification level. The larger decreases of the CO conversion values were more significant between the commercial and self-coated catalysts with the diminishing water content. For the steam to gas ratio of 0.24 and with a reaction temperature range of between 250 and 350 °C, the commercial catalyst clearly exhibited 7 % lower CO conversion.

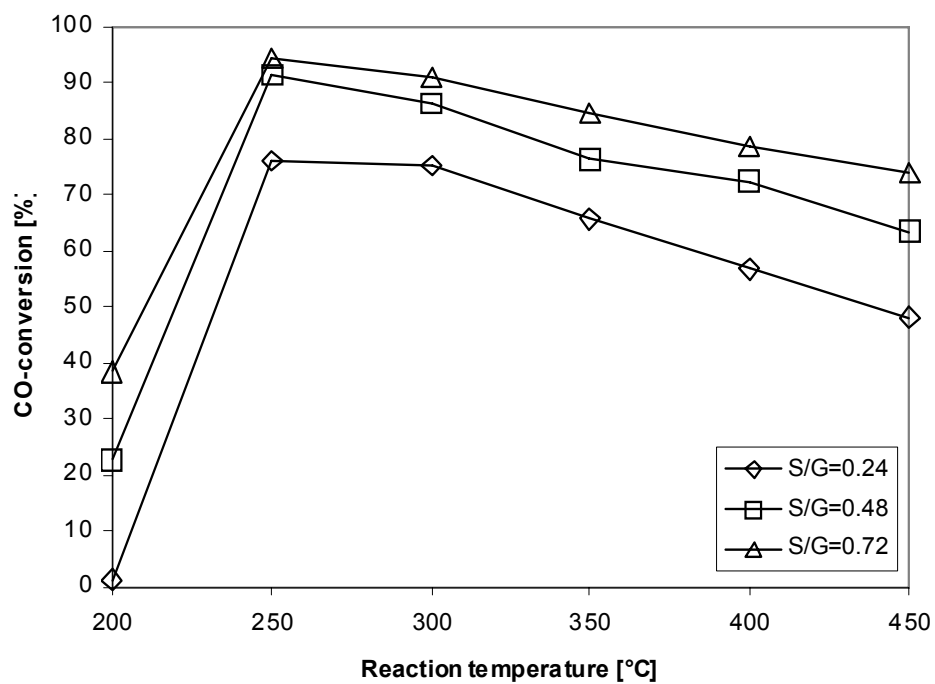


Figure 72 CO-conversion over commercial 2% Pt/CeO₂-catalyst; S/G=0.24-0.72; total feed flow rate: 40 mln/min.

7 SUMMARY

The object of this thesis was the preparation and optimization of catalysts for the water-gas shift reaction in a micro-channel reactor with the aim of generating hydrogen for mobile fuel cell systems. The catalysts had to exhibit high catalytic activity and strong adhesion to support foils and prove long-term stability, especially during start-up/shut-down procedures. Especially it was difficult to achieve strong adhesion of the catalyst coating on the micro-structured material, which was made of metal. The catalysts have to prove high catalytic activity, strong adhesion to support foils and long-term stability to be approved for common usage.

The results of this thesis can be divided into three sections (chapter 4, 5 and 6). In Chapter 4, the wash coatings were prepared from commercially available dry-milled powder catalysts. The commercial catalysts such as PtX, PtY, RuZ, and CuXY were prepared using a milling process. Adhesion characteristics were investigated as a function of the particle sizes of the powder catalysts. Influences of preparation methods, reduction treatments, and concentrations of the gases for HTS and LTS reaction conditions were studied. In chapter 5, the alumina and cerium dioxide wash coats were obtained by spin coating. The coating parameters such as suspension-pH, binder (PVA) molecular weight and solid loading were varied to optimize the homogeneous, well-adhered layer with good thermal stability and high surface area for water-gas shift reaction on microstructures. Chapter 6 focuses on the possibilities using micro-structured reactors after the adapting of Pt catalysts such as Pt/CeO₂/Al₂O₃ and Pt/CeO₂ on micro-channel foils for the one-step water-gas shift reaction at low reaction temperatures. Micro-structured reactors allowed the creation of more compact and efficient systems thanks to new micro-channel devices with the promising possibility of deposition of high surface-area catalysts. This remained a main impact factor which influenced the better catalyst dispersion and better usage, especially for small amounts of expensive precious metals.

The main results of these three chapters are summarized in the following:

In Chapter 4 the literature survey was prepared for the novel WGS-catalysts, advantages of microreactors and commercial catalyst coating on the micro structured devices. The WGS-reaction complexity was studied to present the challenges of the WGS-catalysts for fuel processing applications.

The catalyst samples presented in this work were successfully applied onto microstructured foils made from stainless steel as a catalyst substrate by using a wash coat method. The uniform layer confirmed only aqueous catalyst coats such as PtX, PtY and RuZ thanks to great suspension concentration, viscosity and calcinations parameters. The PtX-2 catalyst was the most suitable for HTS. It achieved a 90 % CO-conversion at 250 °C. Positive effects of the milling process were also spotted for the II-PtY-2 catalyst, which showed the highest CO-conversion of 83 % at 300 °C. However, the milled RuZ-2 catalyst achieved the equilibrium of CO-conversion at higher HTS reaction temperatures between 350-400 °C, which was also a consequence of the highly active methanation process. For this reasons foregoing catalyst was not applicable for the hydrogen system production. The applied Pt/CeO₂ catalysts reached a maximum CO-conversion at the highest investigated temperature (400 °C).

The PtY-2 catalyst exhibited the highest CO-conversion of all catalysts investigated with a maximum of 76 % at 200 °C for LTS. The outlet gas contained 0.5 % of carbon monoxide.

In Chapter 6 the well-adhered coats of CeO₂ and Al₂O₃ were prepared by stabilizing nm powders and support materials such as Al₂O₃ and CeO₂ in suspensions and depositing them on the metallic micro-channel plates by the spin-coating method. The dispersion stability and the detailed interaction between alumina and cerium dioxide particles were established by zeta-potential

measurements, which allowed the flocculation and dispersion stages for solid medium in the suspension to be controlled. The zeta-potential values enabled the maximum stability at pH levels of 4 and 8 for the CeO_2 and Al_2O_3 suspensions, respectively, to be found. The addition of PVA binders with different molecular weights and concentrations into the suspension influenced the particle diameter changes of the solid materials. A small amount of surfactant with a 1/10 ratio was added into the slurry and significantly increased particle dispersion. The highest-resulting Al_2O_3 surface reached $216.4 \text{ m}^2/\text{g}$. The catalysts exhibited strong adhesion to support foils and proved long-term stability, especially during several start-up/shut-down procedures.

In Chapter 7 the $\text{Pt}/\text{CeO}_2/\text{Al}_2\text{O}_3$ catalyst was coated by the spin-coating method in micro-channels of stainless-steel platelets. An optimum of platinum and ceria

resulted from their solution's impregnation on alumina and ceria carriers. The high thermal catalyst stability with high activity was proved under the condition of water-gas shift reaction. The 1 wt.% Pt/24 wt.% $\text{CeO}_2/\text{Al}_2\text{O}_3$ catalyst was the best catalyst for the WGS reaction compared to the 1 wt.% Pt/ CeO_2 catalyst and the industrial 2 wt.% Pt/ CeO_2 catalyst, especially in the case of a low reaction temperature ($250 \text{ }^\circ\text{C}$). The 94.4 % of CO conversion was closed to the thermodynamic equilibrium of the water-gas shift reaction at a WHSV of $14.3 \text{ N l}/(\text{h g}_{\text{cat}})$. The 12 vol.% carbon monoxide content in the outlet reformat gas was decreased to 0.6 % at $250 \text{ }^\circ\text{C}$ in a one-stage WGS reactor.

CHAPTER C

APPENDIX

LIST OF SYMBOLS

ATR – auto thermal reforming
BET surface area – Brauner, Emmett, and Teller surface area
CETAB – cetrimonium bromide
CRT – cathode ray tube
CVD – chemical vapour deposition
DTA – differential thermal analysis
DSC – differential scanning calorimetry
EDX – X-rays elemental dispersion analysis
FET – field effect transistor
GHSV – gas hourly space velocity
HTS – high temperature shift
HT-WGS – high temperature water gas shift
HCR – sandwich – type reactor
HTPEM – high temperature solid polymer fuel cell
HEC – hydroxyl ethyl cellulose
HPC – hydroxyl propyl cellulose
LTS – low temperature shift
LDV – Laser Doppler Velocimetry
LDE – Laser Doppler Electrophoresis
MTS – medium temperature shift
Mw – molecular weight
MEC – methylhydroxyethyl cellulose
Mol.% - mol percent
NDIR – non-dispersive infra-red photometer
PEFC – proton-exchange fuel cell
PEM – solid polymer fuel cell
PVA – polyvinyl alcohol
PEG – poly (ethylene glycol)
RWGS – reverse water gas shift
SOFC – solid oxide fuel cell
STA – simultaneously thermal analysis
SEM – scanning electron microscope
SDS – sodium dodecyl sulphate
TGA – thermal gravimetric analysis
WGSR – water gas shift reaction
WHSV – weight hourly space velocity
WGS – water gas shift
Wt.% - mass-weight percentage
Vol.% - mass-volume percentage
XRD – X-ray diffraction

LIST OF FIGURES

Figure 1 Process Chart for the coupled SOFC-PEFC system.	12
Figure 2 Thermodynamic equilibrium of the WGS reaction as described by the Gibbs free energy change and the equilibrium constant of the reaction as function of temperature	13
Figure 3 Selectivity of WGS catalysts. (▲, Δ) Commercial Fe/Cr/Cu, (●, ○) 2% Pt/CeO ₂ . HTS syngas, total gas SV=45000h ⁻¹ , S/G=0.5 [93].	16
Figure 4 Typical BET plot.	34
Figure 5 The covering of the adsorbent solid surface with gas molecules in form of thin layer [83].	35
Figure 6 Mercury porosimeter: applied pressure as a function of penetrated mercury volume.	37
Figure 7 Mercury porosimeter: pore size distribution.	37
Figure 8 Reflection of X-rays from two planes of atoms in a solid.	40
Figure 9 Schematic of an X-ray powder diffractometer.	40
Figure 10 Furnace system for measurements under water vapour atmosphere.	42
Figure 11 TG-curve (1) with one-level mass reduction according to DIN EN ISO 11358.	42
Figure 12 TG-curve (2) with two-levels mass reduction according to DIN EN ISO 11358.	43
Figure 13 CILAS 1180 system for particle size measurements.	43
Figure 14 System for a large particle (Fraunhofer theory).	44
Figure 15 System for a small particle (Mie Theory).	44
Figure 16 Schematic representation of the structure of the double layer according to Stern's theory	45
Figure 17 Derivation of Smoluchowski's equation	46
Figure 18 Plot of f (κa) against κa.	46
Figure 19 Test stand equipment	48
Figure 20 Microreactor (a); microstructured devices (b). Reactor housing with microstructured platelets (c).	49
Figure 21 Measuring principle (1 – radiator, 2 – aperture, 3 - modulation device, 4 - measuring cuvette, 5 - adjustment unit / calibration unit, 6 – receiver)	50
Figure 22 Measuring principle.	50
Figure 23 Particle size of catalyst powder before milling	54
Figure 24 Particle size of catalyst powder after milling.	55
Figure 25 SEM of the PtX-1 catalyst on a microstructured stainless steel foil.	55
Figure 26 SEM of the PtX-2 catalyst on a microstructured stainless steel foil.	55
Figure 27 SEM of the PtY-1 catalyst on a microstructured stainless steel foil.	55
Figure 28 SEM of the PtY-2 catalyst on a microstructured stainless steel foil.	56
Figure 29 SEM of the RuZ-1 catalyst on a microstructured stainless steel foil.	56
Figure 30 SEM of the RuZ-1 catalyst on a microstructured stainless steel foil.	56
Figure 31 SEM of the Cu-XY-1 catalyst on a microstructured stainless steel foil.	57
Figure 32 SEM of the Pt/CeO ₂ catalyst on a microstructured stainless steel foil.	57
Figure 33 XRD pattern obtained for the 1 wt.% Pt/CeO ₂ catalyst.	58
Figure 34 CO-conversion at 558 ms residence time and 2.1 H ₂ O/CO-ratio over the industrial catalysts as a function of reaction temperature [°C]; HTS-inputgas: CO=8 vol.%, CO ₂ =12 vol.%, H ₂ =23 vol.%, N ₂ =30.6 vol.%, H ₂ O=17 vol.%.	59
Figure 35 CO-conversion at different residence time as a function of reaction temperature [°C] over PtX-1-2; HTS-input gas: CO=8 vol.%, CO ₂ =12 vol.%, H ₂ =23 vol.%, N ₂ =30.6 vol.%, H ₂ O=17 vol.%.	60
Figure 36 CO-conversion at 353 ms, different temperature and H ₂ O/CO-ratio over the PtY-1-2 catalysts (300 °C); HTS-input gas: CO =8 vol.%, CO ₂ =12 vol.%, H ₂ =23 vol.%, H ₂ O =17-47 vol.%, N ₂ =31-10 vol.%.	61

Figure 37 CO-conversion at 353 ms, different temperature and H ₂ O/CO-ratio over the PtX-1-2 and CuXY-1-2 catalysts (300 °C); HTS-input gas: CO =8 vol.%, CO ₂ =12 vol.%, H ₂ =23 vol.%, H ₂ O =17-47 vol.%, N ₂ =31-10 vol.%	61
Figure 38 CO-conversion at 353 ms, different temperature and H ₂ O/CO-ratio over the RuZ-1-2 and Pt/CeO ₂ catalysts (400°C); HTS-inputgas: CO=8 vol.%, CO ₂ =12 vol.%, H ₂ =23 vol.%, H ₂ O=17-47 vol.%, N ₂ =31-10 vol.%	61
Figure 39 CO-conversion at different temperature and 353 ms residence time as a function of the H ₂ O/CO-ratio for the PtX-1-2-catalysts; LTS inputgas: CO=2 vol.%, CO ₂ =18 vol.%, H ₂ =31 vol.%; H ₂ O=27-42 vol.%, N ₂ =21-0.4 vol.% ..	62
Figure 40 CO-conversion at 353 ms residence time and 250°C as a function of H ₂ O/CO-ratio for the PtY-CuXY-1-2-catalysts; LTS-inputgas: CO=2 vol.%, CO ₂ =18 vol.%, H ₂ =31 vol.%; H ₂ O=27-42 vol.%, N ₂ =21-0.4 vol.%	62
Figure 41 SEM picture of microchannel stainless plate after calcination at 900 °C for 3 h	64
Figure 42 Particle size distribution of the Al ₂ O ₃ -and CeO ₂ powders	65
Figure 43 SEM pictures of Al ₂ O ₃ - powder. (a) Low magnification. (b) High magnification	66
Figure 44 SEM pictures of CeO ₂ - powder. (a) Low magnification. (b) High magnification	66
Figure 45 Zeta potential as a function of pH for CeO ₂ - and Al ₂ O ₃ -powders	67
Figure 46 SEM micrographs of Al ₂ O ₃ -layers dried in air (a) and on hot plate (b)	69
Figure 47 SEM micrographs of layers for different solid content: Al ₂ O ₃ – 16/32 (a), 18/36 (b), CeO ₂ - 30/30 (c), 20/20 (d) containing PVA (Mw of 31000 g/mol)	70
Figure 48 SEM micrographs of calcined alumina (Al-2) coating at 700 °C (a) and 500 °C (b) for 2h	71
Figure 49 Mercury porosimetry. Cumulative volume plot for different samples	72
Figure 50 The Al ₂ O ₃ -and CeO ₂ -catalyst coating into microchannels as a function of coating cycles	73
Figure 51 Mass loss of Al ₂ O ₃ and-CeO ₂ -washcoats for three different layer thicknesses and PVA addition (Mw=13000) vs. frequencies in the thermal shock test	75
Figure 52 Mass loss of Al ₂ O ₃ and-CeO ₂ -washcoats for three different layer thicknesses and PVA addition (Mw=31000) vs. frequencies in the thermal shock test	76
Figure 53 Mass loss of Al ₂ O ₃ and-CeO ₂ -washcoats for three different layer thicknesses and PVA addition (Mw=124000) vs. frequencies in the thermal shock test:	76
Figure 54 Mass loss of Al ₂ O ₃ and-CeO ₂ washcoats for three different layer thicknesses and PVA addition (Mw=13000) vs. time in the ultrasonic vibration test	76
Figure 55 Mass loss of Al ₂ O ₃ and-CeO ₂ washcoats for three different layer thicknesses and PVA addition (Mw=31000) vs. time in the ultrasonic vibration test	77
Figure 56 Mass loss of Al ₂ O ₃ and-CeO ₂ washcoats for three different layer thicknesses and PVA addition (Mw=124000) vs. time in the ultrasonic vibration test	77
Figure 57 The loading of CeO ₂ -coating by impregnation on the Al ₂ O ₃ -support, which contained different PVAs (13000, 31000 and 124000 g/mol)	81
Figure 58 The surface morphology of Pt/CeO ₂ /Al ₂ O ₃ catalyst in microchannels	82
Figure 59 The surface morphology of Pt/CeO ₂ catalyst in microchannels	82
Figure 60 The SEM photographs and elemental profiles by EDX for the Pt/CeO ₂ -catalyst coated on the microchannel platelets	82
Figure 61 The SEM photographs and elemental profiles by EDX for the Pt/CeO ₂ /Al ₂ O ₃ -catalyst coated on the microchannel	83
Figure 62 EDX spectrums of samples Pt supported on CeO ₂ : a. Ce-1(I-layer), b. Ce-1(III-layers)	85
Figure 63 EDX spectrums of samples Pt supported on CeO ₂ : a. Ce-2(I-layer), b. Ce-2(III-layers)	85
Figure 64 EDX spectrums of the coated catalyst sample Pt/CeO ₂ supported on Al ₂ O ₃ : Al-1(III-layers) in two different channels	86
Figure 65 CO-conversion over Pt/CeO ₂ /Al ₂ O ₃ -catalyst samples; S/G=0.24; total feed flow rate: 70 mln/min	87
Figure 66 CO-conversion over Pt/CeO ₂ /Al ₂ O ₃ -catalyst (samples nr. 9) as a function of reaction time; S/G=0.24; total feed flow rate: 70 mln/min	88

Figure 67 CO-conversion over Pt/CeO ₂ /Al ₂ O ₃ -catalyst samples; S/G=0.48; total feed flow rate: 70 mln/min.....	88
Figure 68 CO-conversion over Pt/CeO ₂ /Al ₂ O ₃ -catalyst samples; S/G=0.72; total feed flow rate: 70 mln/min.....	89
Figure 69 CO-conversion over Pt/CeO ₂ /Al ₂ O ₃ -catalyst samples; S/G=0.72; total feed flow rate: 40 mln/min (dashed line), 70 mln/min (continuous line).	90
Figure 70 CO-conversion over Pt/CeO ₂ / Al ₂ O ₃ -catalyst samples; S/G=0.72; total feed flow rate: 40 mln/min (dashed line), 70 mln/min (continuous line).	91
Figure 71 CO-conversion over Pt/CeO ₂ -catalyst samples; S/G=0.72; total feed flow rate: 40 mln/min.	92
Figure 72 CO-conversion over commercial 2% Pt/CeO ₂ -catalyst; S/G=0.24-0.72; total feed flow rate: 40 mln/min.	94

LIST OF TABLES

Table 1 Physical and chemical properties of the platinum catalyst based on the literature	18
Table 2 WGS catalyst requirements for mobile applications [27].....	19
Table 3 Suspension method used for catalyst coating onto microchannel foils.....	23
Table 4 Sol-gel method used for catalyst coating onto microchannel foils	26
Table 5 Other methods used for catalyst coating onto microchannel foils.....	29
Table 6 Classification of porosimeter according to pore sizes.....	37
Table 7 Experimental Conditions for HTS and LTS.....	53
Table 8 Specific mass, BET surface area, and calcination parameters for the catalyst samples applied onto the microstructured foil.....	54
Table 9 Influence of surfactant addition in to the suspension containing 8 wt.% of PVA (Mw=18000g/mol) on effective particle diameter of the Al ₂ O ₃ and CeO ₂	68
Table 10 Influence of polymers on the effective particle diameter	68
Table 11 Calcination parameters for Al ₂ O ₃ and CeO ₂ ; T _{calc} =500°C	68
Table 12 Mercury porosimeter analysis of the different suspensions	73
Table 13 Effect of binder and number of layers on the catalyst deposition.....	74
Table 14 Feed gas composition – WGS reaction	79
Table 15 Pt/CeO ₂ /Al ₂ O ₃ -and Pt/CeO ₂ -catalyst compositions.....	79
Table 16 CO-conversion for WGS over Pt/CeO ₂ /Al ₂ O ₃ and Pt/CeO ₂ catalyst samples; S/G=0.72; total feed flow rate: 40 mln/min	93

REFERENCES

- [1] Dokupil, M., Spitta, C., Mathiak, J., Beckhaus, P., Heinzl, A., *Compact propane fuel processor for auxiliary power unit application*, Journal of Power Sources, 2006, 157, 906-913.
- [2] Roychoudhury, S., Lyubovski, M., Shabbir, A., *Microlith catalytic reactors for reforming iso-octane-based fuels into hydrogen*, Journal of Power Sources, 2005, 152, 75-86.
- [3] Kolb, G., Baier, T., Schürer, J., Tiemann, D., Ziogas, A., Specchia, S., Galetti, E., Germani, G., Schuurmann, Y., *A micro-structured 5 kW complete fuel processor for iso-octane as hydrogen supply system for mobile auxiliary power units. Part II – Development of water-gas shift and preferential oxidation reactors and assembly of the fuel processor*, Chemical Engineering Journal (2007), in press.
- [4] Kolb, G., Schürer, J., Tiemann, D., Wiechert, M., Zapf, R., Hessel, V., Löwe, H., *Fuel processing in integrated micro-structured heat-exchanger reactors*, Journal of Power Sources 2007, 171, 198-204.
- [5] Tonkovich, A. Y., Zilka, J. L., LaMont, M. J., Wang, Y., Wegeng, R.S., *Microchannel reactors for fuel processing applications. I. Water gas shift reactor*, Chemical Engineering Science 1999, 54, 2947-2951.
- [6] Goerke, O., Pfeifer, P., Schubert, K., *Water gas shift and selective oxidation of CO in microreactors*, Applied Catalysis A: General 2004, 263, 11–18.
- [7] Basińska, A., Kępiński, L., Domka, F., *The effect of support on WGS activity of ruthenium catalysts*, Applied Catalysis A: General 1999, 183, 143.
- [8] Erdőhelyi, A., Fodor, K., Suru, G. *Reaction of carbon monoxide with water on supported iridium catalysts*, Appl. Catal. A 1996, 139, 131.
- [9] Campbell, C. T., Daube, K. A., *A surface science investigation of the water-gas shift reaction on copper(111)*, J. Catal. 1987, 104, 109.
- [10] Hougen, O. A., Watson, K. M., *Chemical Process Principles*; Wiley: New York, 1947; Vol. III.
- [11] Stoltze, P. *Microkinetic simulation of catalytic reactions*, Progress in Surface Science 2000, 65, 65.
- [12] Milner, P. C., *The possible mechanisms of complex reactions involving consecutive steps*, J. Electrochemical Society 1964, 111, 228.
- [13] Schumacher, N., Boisen, A., Dahl, S., Gokhale, A. A., Kandoi, S., Grabow, L. C., Dumesic, J. A., Mavrikakis, M., Chorkendorff, I., *Trends in low-temperature water-gas shift reactivity on transition metals*, J. Catal. 2005, 229, 265.
- [14] Askgaard, T. S., Nørskov, J. K., Ovesen, C. V., Stoltze, P., *A kinetic model of methanol synthesis*, J. Catal. 1995, 156, 229.
- [15] Grenoble, D. C., Estadt, M. M., Ollis, D. F., *The chemistry and catalysis of the water gas shift reaction. 1. The kinetics over supported metal catalysts*, J. Catal. 1981, 67, 90.
- [16] Shido, T., Iwasawa, Y., *The effect of coadsorbates in reverse water-gas shift reaction on ZnO, in relation to reactant-promoted reaction mechanism*, J. Catal. 1993, 140, 575.
- [17] Van Herwijnen, T., De Jong, W. A., *Kinetics and mechanism of the CO shift on Cu/ZnO. I. Kinetics of the forward and reverse CO shift reactions*, J. Catal. 1980, 63, 83.
- [18] Tanaka, Y., Utaka, T., Kikuchi, R., Sasaki, K., Eguchi, K., *CO removal from reformed fuel over*

- Cu/ZnO/Al₂O₃ catalysts prepared by impregnation and coprecipitation methods*, Applied Catal. A: General 2002, 6032, 1.
- [19] Li, Y., Fu, Q., Flytzani-Stephanopoulos, M., *Low-Temperature water-gas-shift reaction over Cu- and Ni-loaded cerium oxide catalysts*, Appl. Catal. B 2000, 27, 179.
- [20] Jacobs, G., Ricote, S., Graham, U. M., Petterson, P. M., Davis, B. H., *Low temperature water gas shift: Type and loading of metal impacts forward decomposition of pseudo-stabilized formate over metal/ceria catalysts*, Catalysis Today 2005, 106, 259-264.
- [21] Boccuzzi, F., Chiorino, A., Manzoli, M., Andreeva, D., Tabakova, T., FTIR Study of the Low-Temperature Water-Gas Shift Reaction on Au/Fe₂O₃ and Au/TiO₂, *CatalystsJ. Catal.* 1999, 188, 176.
- [22] Germani, G., Alphonse, P., County, M., Schuurman, Y., Miradatos, C., *Platinum/ceria/alumina catalysts on microstructures for carbon monoxide conversion*, Cat. Today 110 (2005) 114-120.
- [23] Kolb, G., Baier, T., Schürer, J., Tiemann, D., Ziogas, A., Specchia, S., Galetti, E., Germani, G., Schuurmann, Y., *A micro-structured 5 kW complete fuel processor for iso-octane as hydrogen supply system for mobile auxiliary power units. Part II – Development of water-gas shift and preferential oxidation reactors and assembly of the fuel processor*, Chemical Engineering Journal (2007), in press.
- [24] Kolb, G., Pennemann, H., Zapf, R., *Water-gas shift reaction in micro-channels—Results from catalyst screening and optimisation*, Cat. Today 110 (2005) 121-131.
- [25] Germani, G., Schuurman, Y., *AIChE Journal, Water-Gas Shift Reaction Kinetics over μ -Structured Pt/CeO₂/Al₂O₃ Catalysts*, May 2006, Vol. 52, No. 5., 1807-1813.
- [26] Valentini, M., Groppi, G., Cristiani, C., Levi, M., Tronconi, E., Forzatti, P., *The deposition of γ -Al₂O₃ layers on ceramic and metallic supports for the preparation of structured catalysts*, Catal. Today 2001, 69, 307–314.
- [27] Serre, C., Garin, F., Belot, G., Maire, G., *Reactivity of Pt/Al₂O₃ and Pt-CeO₂/Al₂O₃ Catalysts for the Oxidation of Carbon Monoxide by Oxygen*, J. Catal. 1993, 141, 1.
- [28] Amadeo, N. E., Laborde, M. A., *Hydrogen Production from the Low Temperature Water-Gas Shift Reaction: Kinetics and Simulation of the Industrial Reactor*, Int. J. Hydrogen Energy 1995, 20, 949.
- [29] Germani, G., Stefanescu, A., Schuurman, Y., van Veen, A.C., *Preparation and characterization of porous alumina-based catalyst coatings in microchannels*, Chemical Engineering Science 2007, 62, 5084 – 5091.
- [30] Chen, G., Li, S., Yuan, Q., *Pd-Zn/Cu-Zn-Al catalysts prepared for methanol oxidation reforming in microchannel reactors*, Catalysis Today 2007, 120, 63-70.
- [31] Kundu, A., Park, J.M., Ahn, J.E., Park, S.S., Shul, Y.G., Han, H.S., *Micro-channel reactor for steam reforming of methanol*, Fuel 2007, 1331-1336.
- [32] Hu, J., Brooks, K.P., Holladay, J.D., Howe, D.T., Simon, T.M., *Catalyst development for microchannel reactors for martian in situ propellant production*, Catalyst Today (2007), doi: 10.1016/j.cattod.2007.01.067.
- [33] Wu, X., Weng, D., Zhao, S., Chen, W., *Influence of an aluminized intermediate layer on the adhesion of a γ -Al₂O₃ washcoat on FeCrAl*, Surface and Coatings Technology 2005, 190, 434-439.

- [34] Yu, X., Tu, S.-T., Wang, Z., Qi, Y., *On-board production of hydrogen for fuel cells over Cu/ZnO/Al₂O₃ catalyst coating in a micro-channel reactor*, Journal of Power Source (2005), doi:10.1016/j.jpowsour.2005.02.027.
- [35] Men, Y., Gnaser, H., Zapf, R., Hessel, V., Ziegler, C., Kolb, G., *Steam reforming of methanol over Cu/CeO₂/γ-Al₂O₃ catalysts in a microchannel reactor*, Applied Catalysis A: General 2004, 277, 83-90.
- [36] Wang, Y., Chin, Y.H., Rozmiarek, R.T., Johnson, B.R., Geo, Y., Watson, J., Tonkovich, A. Y.L., Vander Wiel, D.P., *Highly active and stable Rh/MgO-Al₂O₃ catalysts for methane steam reforming*, Catalyst Today 2004, 98, 575-581.
- [37] Wang, Y., Chin, Y.H., Geo, Y., U.S. Patent 6,713,519.
- [38] Badini, C., Laurella, F., *Oxidation of FeCrAl alloy: influence of temperature and atmosphere on scale growth rate and mechanism*, Surface and Coatings Technology 2001, 135, 291-298.
- [39] Seo, Y.-S., Yu, S.-P., Cho, S.-J., Song, K.-S., *The catalytic heat exchanger using catalytic fin tubes*, Chemical Engineering Science 2003, 58, 43-53.
- [40] Zhao, S., Zhang, J., Weng, D., Wu, X., *A method to form well-adhered γ-Al₂O₃ layers on FeCrAl metallic supports*, Surface and Coatings Technology 2003, 167, 97-105.
- [41] Yasaki, S., Yoshino, Y., Ihara, K., Ohkubo, K., US Patent No. 5,208,206 (May 4, 1993).
- [42] Zwinkels, M.F.M., Jaras, S.G., Govind Menon, P., in: G. Poncelet, et al. (Eds.), *Proceedings of the Sixth International Symposium on Scientific Bases for the Preparation of Heterogenous Catalysts*, Elsevier, Amsterdam, 1995.
- [43] K. Haas-Santo, M. Fichtner, K. Schubert, *Preparation of microstructure compatible porous supports by sol-gel synthesis for catalyst coatings*, Applied Catalysis A: General A 2001, 220, 79-92.
- [44] Zapf, R., Becker-Willinger, C., Berresheim, K., Bolz, H., Gnaser, H., Hessel, V., Kolb, G., Löb, P., Pannwitt, A.-K., Ziogas, A., *Detailed characterization of various porous alumina-based catalyst coatings within Microchannels and their testing for methanol steam reforming*, Trans IChemE, Vol 81, Part A, August 2003.
- [45] Müller, A., Drese, K., Gnaser, H., Hampe, M., Hessel, V., Löwe, H., Schmitt, S., Zapf, R., *Fast preparation and testing methods using a microstructured modular reactor for parallel gas phase catalyst screening*, Catalyst Today 2003, 81, 377-391.
- [46] Cominos, V., Hessel, V., Hofman, C., Kolb, G., Zapf, R., Ziogas, A., Delsman, E. R., Schouten, J. C., *Selective oxidation of carbon monoxide in a hydrogen-rich fuel cell feed using a catalyst coated microstructured reactor*, Catalyst Today 2005, 110, 140-153.
- [47] Pfeifer, P., Schubert, K.; Liauw, M.A.; Emig, G., *PdZn catalysts prepared by washcoating microstructured reactors*, Applied Catalysis A: General 2004, 270, 165-175.
- [48] Pfeifer, P., Schubert, K., Emig, G., *Preparation of copper catalyst washcoats for methanol steam reforming in microchannels based on nanoparticles*, Applied Catalysis A: General 2005, 286, 175-185.
- [49] Agrafiotis, C., Tsetsekou, A., Ekonomakou, A., *The effect of particle size on the adhesion properties of oxide washcoats on cordierite honeycombs*, Journal of Materials Science Letters 1999, 18, 1421-1424.
- [50] Villegas, L., Masset, F., Guilhaume, N., *Wet impregnation of alumina-washcoated monoliths: Effect of the drying procedure on Ni distribution and*

- on autothermal reforming activity*, Applied Catalysis A: General 2007, 320, 43-55.
- [51] Pérez-Cadenas, A. F., Kapteijn, F., Moulijn, J. A., *Tuning the morphology of monolith coatings*, Applied Catalysis A: General 2007, 319, 267-271.
- [52] Hwang, S.-M., Kwon, O. J., Kim, J. J., *Method of catalyst coating in micro-reactors for methanol steam reforming*, Applied Catalysis A: General 2007, 316, 83-89.
- [53] Chen, H., Bednarova, L., Besser, R. S., Lee, W. Y., *Surface-selective infiltration of thin-film catalyst into microchannel reactors*, Applied Catalysis A: General A 2005, 286, 186-195.
- [54] Wunsch, R., Fichtner, M., Goerke, O., Haas-Santo, K., Schubert, K., *Process of Applying Al₂O₃ Coatings in Microchannels of Completely Manufactured Microstructured Reactors*, Chemical Engineering & Technology 2002, 25, 7.
- [55] Goerke, O., Pfeifer, P., Schubert, K., *Highly selective methanation by the use of a microchannel reactor*, Catalyst Today 2005, 110, 132-139.
- [56] Shetty, K., Zhao, S., Cao, W., Siriwardane, U., Seetala, N. V., Kuila, D., J. Pow. Sour. 2007, 163, 630-636.
- [57] Giornelli, T., Löfberg, A., Bordes-Richard, E., *Grafting of VO_x/TiO₂ catalyst on anodized aluminum plates for structured catalytic reactors*, Thin Solid Films 2005, 479, 64-72.
- [58] Lim, M. S., Kim, M. R., Noh, Woo, S. I., *A plate-type reactor coated with zirconia-sol and catalyst mixture for methanol steam-reforming*, Journal of Power Sources 2005, 140, 66-71.
- [59] Won, J. Y., Jun, H. K., Jeon, M. K., Woo, S. I., *Performance of microchannel reactor combined with combustor for methanol steam reforming*, Catalyst Today 2006, 111, 158-163.
- [60] Conant, T., Karim, A., Datye, A., Cat. Tod. (2007), doi:10.1016/j.cattod..207.01.061, 1-5.
- [61] Yoldas, B. E., *Alumina Sol Preparation from Alkoxides*, American Ceramic Society Bulletin 1975, 22, 289-290.
- [62] Meille, V., Pallier, S., Santa Cruz Bustamante, G. V., Roumanie, M., Reymond, J.-P., *Deposition of γ -Al₂O₃ layers on structured supports for the design of new catalytic reactors*, Applied Catalysis A: General 2005, 286, 232-238.
- [63] Hwang, S. – M., Kwon, O.J., Kim, J. J., *Method of catalyst coating in micro-reactors for methanol steam reforming*, Applied Catalysis A: General 2007, 316, 83-89.
- [64] Conant, T., Karim, A., Datye, A., *Coating of Steam Reforming Catalysts in Non-Porous Multi-Channeled Microreactors*, Catalyst Today 2007, 125, 11-15.
- [65] Janicke, M. T., Kestenbaum, H., Hagendorf, U., Schüth, F., Fichtner, M., Schubert, K., *The Controlled Oxidation of Hydrogen from an Explosive Mixture of Gases Using a Microstructured Reactor/Heat Exchanger and Pt/Al₂O₃*, Journal of Catalysis Catalyst 2000, 191, 282-293.
- [66] Fukuhara, C. , Kamata, Y., Igarashi, A., *Catalytic performance of microtube-type copper-based catalyst for methanol steam reforming, prepared on the inner wall of an aluminum tube by electroless plating*, Applied Catalysis A: General 2005, 296, 100-107.
- [67] Thybo, S., Jensen, S., J. Johansen, J., Johannessen, T., Hansen, O., Quaade, U. J., *Flame spray deposition of porous catalysts on surfaces and in microsystems*, Journal of Catalysis 2004, 223, 271-277.
- [68] Yeong, K. K., Gavriilidis, A., Zapf, R., Hessel, V., *Catalyst preparation and deactivation issues for*

- nitrobenzene hydrogenation in a microstructured falling film reactor*, *Catalyst Today* 2003, 81, 641-651.
- [69] Rebov, E. V., Kuznetsov, S. A., De croon, M. H. J. M., Schouten, J. C., *Study of the water-gas shift reaction on Mo₂C/Mo catalyst coatings for application in microstructured fuel processors*, *Catalyst Today* (2007), doi:10.1016/j.cattod.2007.01.075.
- [70] Rebov, E. V., Seijger, G. B. F., Calis, H. P. A., de Coon, M. H. J. M., van den Bleek, C. M., Schouten, J. C., *The preparation of highly ordered single layer ZSM-5 coating on prefabricated stainless steel microchannels*, *Applied Catalysis A: General* 2001, 206, 125-143.
- [71] Cominos, V., Hessel, V., Hofmann, C., Kolb, G., Zapf, R., Ziogas, A., Delsman, E.R., Schouten, J.C., *Platinum/ceria/alumina catalysts on microstructures for carbon monoxide conversion*, *Catalyst Today* 2005, 110, 140-153.
- [72] Schimpf, S., Lucas, M., Mohr, C., Rodemerck, U., Bruckner, A., Radnik, J., Hofmeister H., Claus, P., *Supported gold nanoparticles: in-depth catalyst characterization and application in hydrogenation and oxidation reactions*, *Catalyst Today* 2002, 72, 63–78.
- [73] Schuessler, M., Portscher, M., Limbeck, U., *Monolithic integrated fuel processor for the conversion of liquid methanol*, *Catalyst Today* 2003, 79, 511–520.
- [74] Sidwell, R.W., Zhu, H., Kibler, B.A., Kee, R.J., Wickham, D.T., *Experimental investigation of the activity and thermal stability of hexaaluminate catalysts for lean methane–air combustion*, *Applied Catalysis A: General* 2003, 255, 279–288.
- [75] Younes-Metzler, O., Svagin, J., Jensen, S., Christensen, C.H., Hansen, O., Quaade, U., *Microfabricated high-temperature reactor for catalytic partial oxidation of methane*, *Applied Catalysis A, General* 2005, 284, 5–10.
- [76] Huang, Y.-Y., Chou, K.-S., *Studies on the spin coating process of silica films*, *Ceramics International* 2003, 29, 485–493.
- [77] Bravo, J., Karim, A., Conant, T., Lopez, G.P., Datye, A., *Wall coating of a CuO/ZnO/Al₂O₃ methanol steam reforming catalyst for micro-channel reformers*, *Chemical Engineering Journal* 2004, 101, 113–121.
- [78] Chen, C.H., Emond, M.H.J., Kelder, E.M., Meester, B., Schoonman, J., *Electrostatic sol spray deposition of nanostructured ceramic thin films*, *Journal of Aerosol Science* 1999, 30, 959–967.
- [79] Nomura, M., Meester, B., Schoonman, J., Kapteijn, F., Moulijn, J.A., *Preparation of thin porous titania films on stainless steel substrates for heat exchange (HEX) reactors*, *Separation and Purification Technology* 2003, 32, 387-395.
- [80] Stefanescu, A., van Veen, A. C., Duval – Brunel, E., Mirodatos, C., *Investigation of a Ni-based steam reforming catalyst developed for the coating of microstructures*, *Chemical Engineering Science* 2007, 62, 5092 – 5096.
- [81] Walter, S.; Malmberg, S., Schmidt, B., Liauw, M., *Microstructured reactors for catalytic reactions*, *Catalyst Today* 2005, 110, 15–25.
- [82] Lowell, S., Shields, J. E., *Powder Surface Area and Porosity*, Springer Netherland, 1991; 3. rd ed.
- [83] <http://www.oleinotec.fi/pdf/QC/Autosorb1Bro.pdf>
- [84] Washburn, E.. W., *The observed flow behavior disagrees with models based on the classical Washburn flow*, *Phys. Rev.* 1921, 17, 273.
- [85] Ritter, H. L., Drake, L. C., *IEC Anal. Ed.* 1945, 17, 782-787.

- [86] Mayer, R. P., Stowe, R. A., J. Colloid Interface Science 1965, 20, 893.
- [87] <http://materials.binghamton.edu/labs/xray/xray.html>
- [88] <http://www.cilas.com/theory/ffrau.html>
- [89] Shaw, D.J., *Introduction to Colloid and Surface Chemistry*, London, Butterworths 1966.
- [90] Operator's Manual, *Advance Optima*, Modular Process Analyser System.
- [91] Bae, J.-M., Ahmed, S., Kumar, R., Doss, E., *Microchannel development for autothermal reforming of hydrocarbon fuels*, Journal of Power Sources 2005, 139, 91-95.
- [92] Kiwi-Minsker, L., Renken, A., *Microstructured reactors for catalytic reactions*, Catalysis Today 2005, 110, 2-14.
- [93] Luengnaruemitchai, A., Osuwan, S., Gulari, E., *Comparative studies of low-temperature water-gas shift reaction over Pt/CeO₂, Au/CeO₂, and Au/Fe₂O₃ catalysts*, Catalysis Communications 2003, 4, 215-221.
- [94] Wheeler, C., Jhalani, A., Klein, E. J., Tummala, S., Schmidt, L. D., *The water-gas-shift reaction at short contact times*, Journal of Catalysis 2004, 223, 191-199.
- [95] Hilaire, S., Wang, X., Luo, T., Gorte, R. J., Wagner, *A comparative study of water-gas-shift reaction over ceria supported metallic catalysts*, J. Appl. Catal. 2001, 215, 271.
- [96] Zhao, I. et al., *The influence of milling parameters on the properties of the milled powders and the resultant coatings*, Surface of Coatings Technology 2003, 168, 179-185.
- [97] Hessel, V., Loewe, H., Mueller, A., Kolb, G. *Chemical Micro Process Engineering- Processing and Plants*; Wiley-VCH: Weinheim, 2005, 290-393.
- [98] Wang, X., Gorte, R. J., Wagner, J. P., Effect of pre-treatment conditions on the performance of sulfided Ni-Mo/ γ -Al₂O₃ catalysts for hydrogenation of linear aldehydes, J. Catal. 2002, 212-225.
- [99] Kušar, H., Hočevár, S., Levec, *Kinetics of the water-gas shift reaction over nanostructured copper-ceria catalysts*, J. Appl. Catal. B 2006, 63, 194-200.
- [100] Jacobs, G., Ricote, S., Patterson, P. M., Graham, U. M.; Dozier, A., Khalid, S., Rhodus, E., Davis B. H., Low temperature water-gas shift: Examining the efficiency of Au as a promoter for ceria-based catalysts prepared by CVD of a Au precursor, Appl. Catal. 2005, 292, 229-243.
- [101] Jacobs, G.; Williams, L., Graham, U. M.; Sparks, D. E., Davis, B. H., *Low-Temperature Water-Gas Shift: In-Situ DRIFTS-Reaction Study of a Pt/CeO₂ Catalyst for Fuel Cell Reformer Applications*, J. Phys. Chem. 2003, 107, 10398.
- [102] Ricote, S., Jacobs, G., Milling, M., Ji, Y., Petterson, P. M., Davis, B. H., *Low temperature water-gas shift: Characterization and testing of binary mixed oxides of ceria and zirconia promoted with Pt*, Appl. Catal. A 2006, 303, 35-47.
- [103] Panagiotopoulou, P., Kondarides D. I., *Effect of the nature of the support on the catalytic performance of noble metal catalysts for the water-gas shift reaction*, Catal. Today 2006, 112, 49-52.
- [104] Xue, E., O'Keefe, M. O., Ross, J. R. H., *Water-gas shift conversion using a feed with a low steam to carbon monoxide ratio and containing sulfur*, Catal. Today 1996, 30, 107.
- [105] Choi, Y., Tajima, K., Shin, W., Izu, N., Matsubara, I., Murayama, N., *Combustor of ceramic Pt/alumina catalyst and its application for micro-thermoelectric hydrogen sensor*, Appl. Catal. A. 2005, 287, 19-24.

- [106] Milner, P.C., *The possible mechanisms of complex reactions involving consecutive steps*, J. Electrochemical Society 1964, 111, 228.
- [107] Liguras, D.K., Goundani, K., Verykios, X.E., *Production of hydrogen for fuel cells by catalytic partial oxidation of ethanol over structured Ni catalysts*, J. Power Sources 2004, 130, 30–37.
- [108] Kikuchi, R., Maeda, S., Sasaki, K., Wennerström, S., Ozawa, Y., Eguchi, K., *Catalytic activity of oxide-supported Pd catalysts on a honeycomb for low-temperature methane oxidation*, Appl. Catal. A 2003, 239, 169–179.
- [109] Zhao, H., Hu, Y., Li, J., *Reduced rate method for discrimination of the kinetic models for the water-gas shift reaction*, Journal of Molecular Catalysis A: Chemical 1999, 149, 141.
- [110] Yasaki, S., Toshino, Y., Ihara, K., Ohkubo, K.; US Patent No. 5, 208, 206 (May 4, 1993).
- [111] Pugh, R. J., Bergström, L., *Surface and colloid chemistry in advanced ceramics processing*, Volume 51, Marcel Dekker, Inc. 1994, New York.
- [112] Cristiani, C., Valentini, M., Merazzi, M., Neglia, S., Forzatti, P., *Effect of ageing time on chemical and rheological evolution in γ -Al₂O₃ slurries for dip-coating*, Catalysis Today 2005, 105, 493-495.
- [113] Lefèvre, G., Duc, M., Fédoroff, M., *Effect of solubility on the determination of the protonable surface site density of oxyhydroxides*, J. Colloids Interf. Sci. 2004, 269, 274.
- [114] Laiti, E., Öhman, L.O., Nordin, J., Sjöberg, S., *Acid/Base Properties and Phenylphosphonic Acid Complexation at the Aged γ -Al₂O₃/Water Interface*, J. Colloid Interf. Sci. 1995, 175, 230.
- [115] Krusty, M. R., (Ed.) *Colloid Science*, vol. I, Elsevier, Amsterdam, 1965.
- [116] Pawlak, M., Hacker, V., Siebenhofer, M., *Hydrogen purification using microstructures; Part I: Preparation of Al₂O₃-and CeO₂ washcoats in Microchannels*, submitted in Chemical Engineering Communications for publication.
- [117] Jiang, P., Lu, G., Guo, Y., Guo, Y., Zhang, S., Wang, X., *Preparation and properties of a γ -Al₂O₃ washcoat deposited on a ceramic honeycomb*, Surface & Coating Technology 2005, 190, 314-320.
- [118] Giani, L.; Cristiani, C.; Groppi, G.; Tronconi, E., *Washcoating method for Pd/ γ -Al₂O₃ deposition on metallic foams*, Appl. Catal. B, 2006, 62, 121–131.
- [119] Pfeifer, P., Schubert, K., Emig, G., *Preparation of copper catalyst washcoats for methanol steam reforming in microchannels based on nanoparticles*, Appl. Catal. A: General, 2005, 286, 175-185.
- [120] Ladebeck, J. R.; Wagner, J. P., *Handbook of Fuel Cells – Fundamentals, Technology and Applications* 2003, 3, 198.
- [121] Pawlak, M., Thaler, M., Hacker, V., *Characterisation of HTS and LTS reactions in micro-structured reactors*, Energy & fuels 21 (2007) 4, 2299 – 2305.
- [122] Pawlak, M., Hacker, V., Siebenhofer, M., *Hydrogen purification using microstructures; Part II: Catalytic performance of nm-Pt-catalyst for water gas shift on microstructured plates*, submitted in Chemical Engineering Communications for publication.